Isochronous Mass Measurements of Short-Lived Neutron Rich Nuclides at the FRS-ESR Facilities

Inaugural-Dissertation
zur Erlangung des
Doktorgrades der Naturwissenschaften
der Justus-Liebig-Universität Giessen
(Fachbereich 07 / Mathematik, Physik, Geographie)

vorgelegt von
Milan Matoš
geboren in Poprad

Giessen, im Mai 2004

Dekan: Prof. Dr. V. Metag
I. Berichterstatter: Prof. Dr. H. Geissel
II. Berichterstatter: Prof. Dr. V. Metag
Tag der mündlichen Prüfung: 28.5.2004

Always aim at complete
harmony of thought and word and deed.
Always aim at purifying
your thoughts and
everything will be well.

Mohandas Karamachand Gandhi

Preface

This work has been carried out at the FRS group of the KPII department at GSI in Darmstadt, Germany, during the years 2001–2004.

I would like to thank all the people for their help during my years at GSI, but also at JINR in Dubna, Russia, and Comenius University in Bratislava, Slovakia.

In particular I am grateful to Prof. Dr. Gottfried Münzenberg for affiliation in KPII and giving me the chance to work at GSI.

I would like to express my sincere gratitude to Prof. Dr. Hans Geissel for his guidance and support. His assignment for fulfilling the tasks in physics is encouraging and gives a lot of motivation.

I would like to thank Prof. RNDr. Štefan Šáro, DrSc. who introduced me into the field of experimental nuclear physics. A lot of his advises helped me in my work.

My warmest thanks go also to Prof. Dr. Yuri N. Novikov for his encouragement, support and help.

Discussions and advises from Dr. Marc Hausmann meant a relevant help for writing this thesis.

My stay in Dubna increased my knowledge in nuclear physics too. For this I thank Prof. Dr. Gurgen M. Ter-Akopian and Dr. Roman Wolski.

My closest fellows in my work were Dr. Yuri A. Litvinov, Dr. Christoph Scheidenberger, Dr. Jens Stadlmann, Dr. Helmut Weick and Dr. Martin Winkler. Especially I would like to thank to Martin who was always ready to help me in the foreign country.

It was a pleasure for me to learn about physics from Prof. Dr. Fritz Bosch, Dr. Zygmunt Patyk, Dr. Bernd Pfeiffer, Prof. Dr. Hendrik Schatz, Dr. Dave Vieira and Prof. Dr. Hermann Wollnik.

The friendly atmosphere was created also thanks to colleagues and guests Dr. Faouzi Attallah, David Boutin, Dr. Vladimir Chichkine, Dr. Thomas Faestermann, Dr. Margareta Hellström, Evangelia Kaza, Dr. Otto Klepper, Dr. Christopher Kozhuharov, Ludwig Maier, Michael Maier, Dr. Takahisa Ohtsubo, Dr. Wolfgang Plaß (also thanks for corrections), Dr. Mauricio Portillo, Dr. Peter Torsten Radon, Dr. Klaus Sümmerer and Dr. Takayuki Yamaguchi.

Also the support from the technician Karl-Heinz Behr, Adolf Brünle, Karlheinz Burkard, Hans-Joachim Schött and the secretaries Siggi, Tanya and Inna is greatly acknowledged.

The experts of the ESR — Dr. Peter Beller, Bernhard Franczak, Dr. Bernhard Franzke, Dr. Fritz Nolden, Dr. Markus Steck have contributed a lot during the experiments.

V neposlednom rade by som sa chcel poďakovať svoje rodine, za lásku a za podporu. Ďakujem za pomoc mojim rodičom, Martinke za trpezlivosť a za všetko.

Milan Matoš Darmstadt
May 2004

Abstract

Precise mass values of nuclides are of great importance for the basic understanding of nuclear structure and decay. The neutron-rich area of nuclides up to the neutron dripline has the largest discovery potential for new nuclear properties. The neutron dripline is reached only for light elements up to oxygen.

The combination of the fragment separator FRS with the storage ring ESR at GSI is a unique facility in the world for research with exotic nuclei. The software package TOFSIM was developed to simulate the crucial parameter settings for the performance of these complex facilities in the present experiments.

In this study we used neutron-rich nuclides produced via fragmentation of 456 A·MeV ^{70}Zn projectiles and via fission of ^{238}U projectiles at different energies (380–415 A·MeV). The FRS separated in-flight the selected exotic nuclei and injected them into the ESR. Bare or H-like ions were investigated in the ESR operated in the isochronous mode as a high-resolution time-of-flight mass spectrometer.

The present experimental studies are the first isochronous mass measurements that covered a larger area of n-rich short-lived nuclides. More than 500 peaks corresponding to 280 neutron-rich isotopes from oxygen to promethium were carefully analyzed. For 41 nuclides experimental mass values were obtained for the first time and for 20 isotopes the current values in the literature were improved. A mass resolving power of 2×10^5 was achieved for ions with the best isochronicity and the accuracy ranged from 140–400 keV. The nuclide with the shortest known half-life (17 ms) was ^{13}B, however, we can investigate nuclides with much lower half-lives, since the method allows to go down to a few hundreds of μs.

Comparisons of our experimental results with different mass predictions reveal large deviations particularly for the most neutron-rich nuclides. A remarkable result is that the pure microscopic theoretical model [SGP03] is better (σ_{rms} =575 keV) in this new territory than the microscopic-macroscopic FRDM description [MNMS95] (σ_{rms} =667 keV). In the recently measured neutron-deficient new mass surface the FRDM prediction was still a factor of two superior due to the method of parameter adjustment to experimental data. This reflects the advantage of microscopic theories for unknown mass areas far from the valley of beta stability. Much room for improvements is also observed from the comparison with the Atomic Mass Evaluation (AME) [ABW03]. The AME has for our

previously measured new neutron-deficient mass surface [Lit03] a σ_{rms} deviation of 148 keV and has now for the 41 new masses in this work 651 keV. For individual nuclides the deviation is even larger, e.g. for ^{109}Nb and ^{114}Tc isotopes the differences from AME reach 1.5 MeV.

The region of the new masses from this experiment can also contribute to the knowledge of nucleosynthesis for r-process nuclei and help to determine the corresponding path.

In summary this pioneering experiment performed at the FRS-ESR facility at GSI contributes a lot to improve the knowledge on neutron-rich nuclides. In future experiments our goals are to increase the resolution and accuracy of the method and to reach more exotic nuclei, particularly along the predicted r-process path for Z>30.

Zusammenfassung

Experimente zur genauen Massenmessungen von kurzlebigen exotischen Kernen sind von großer Bedeutung, um die Kernmodelle überprüfen und verbessern zu können. Besonders sind diese Beiträge bei den neutronenreichen Kernen wertvoll, da dort die Dripline nur bis zum Sauerstoff erreicht wurde und somit diese Kerne das größte Entdeckungspotential für neue Eigenschaften darstellen.

Die Kombination des Fragmentseparators FRS mit dem Speicherring ESR ist eine einmalige und sogleich universelle Anlage zur Untersuchung von exotischen Kernen. Im Rahmen dieser Arbeit wurde zunächst das Computerprogramm TOFSIM entwickelt, um die Experimentplanung, Durchführung und Datenanalyse effektiv zu unterstützen. Solche Simulationsprogramme sind unentbehrlich für die Forschungsarbeiten mit den komplexen Anlagen, wie FRS und ESR bei GSI.

Im Rahmen dieser Arbeit wurden zwei Experimente zur direkten Massenmessung mit gespeicherten kurzlebigen Kernen durchgeführt. Neutronenreiche, mittelschwere Nuklide wurden zum einen durch Fragmentation von 456 A MeV ^{70}Zn Projektilen und durch Spaltung von ^{238}U Strahlen im Energiebereich von 380–415 A MeV produziert. Die Reaktionsprodukte wurden mit dem FRS im Fluge separiert und in den Speicherring injiziert. Der ESR wurde für diese Messungen in der isochronen ionenoptischen Einstellung betrieben. Diese Betriebsart ermöglicht, dass die Umlauffrequenz für ein bestimmtes Massen-zu-Ladungsverhältnis unabhängig von der Geschwindigkeitsbreite der gespeicherten Ionen ist. Die Fragmentstrahlen haben von ihrer Entstehungsreaktion her eine unvermeidliche Geschwindigkeitsbreite, die eine Präzisionsmassenmessung mit Hilfe der Umlauffrequenz im Speicherring vereiteln würde. Der Vorteil der isochronen Massenmessung ist, dass keine Kühlung im ESR notwendig ist und somit auch die interessanten kurzlebigen Kerne im Experiment erfasst werden können.

In den isochronen Massenmessungen dieser Arbeit wurden für 41 neutronenreiche Kerne im Elementbereich von Sauerstoff bis Promethium die Massen erstmals gemessen und für 20 Kerne die Literaturwerte verbessert. Dabei wurden die Zeitverteilungen von 280 Isotopen gemessen und analysiert. Im Bereich der untersuchten Kerne hatte das kurzlebigste Isotop eine Halbwertszeit von 17 ms (^{13}B), jedoch ist die isochrone Massenmessung prinzipiell bis hinunter in den Zeitbereich von einigen hundert Mikrosekunden voll einsetzbar.

In den Massenmessungen konnte eine Auflösung von 200000 für die isochron umlaufenden Teilchen erreicht werden. Die Genauigkeit betrug 140–400 keV und war hauptsächlich durch die erreichte Statistik und die Eigenschaften der Referenzmassen bestimmt.

Vergleiche mit theoretischen Vorhersagen zeigen, dass im untersuchten Massenbereich die mikroskopischen Hatree-Fock Theorien den makro-mikroskopischen Vorhersagen überlegen sind. Dieser Trend wurde nicht bei unseren früheren Messungen in der Bleigegend im Bereich der neutronenarmen Kerne beobachtet. Der Vergleich mit semiempirischen Tabellen zeigt ebenfalls für die neutronenreiche Gegend größere Abweichungen. Beispielsweise wurden Abweichungen für einige neue Massen bis 1500 keV gemessen.

Die erzielten neuen und verbesserten Massenwerte können nicht nur zur Verbesserung der Kernmodelle einen Beitrag leisten, sondern sind auch wichtig zum Verständnis des r-Prozesses und vor allem auch zum Festlegen des entsprechenden Pfades auf der Nuklidkarte.

Die Experimente dieser Arbeit liefern die ersten umfassenden Messungen von neutronenreichen Kernmassen mit der isochronen Technik im ESR. Die nächsten Ziele in diesen Experimenten sind, die Auflösung und Genauigkeit der Methode zu erhöhen. Dies soll durch Modifikationen des Flugzeitdetektors und durch ionenoptische Verbesserungen bei der Einstellung und Diagnose erfolgen. In der ferneren Zukunft eröffnet die NUSTAR Anlage mit dem Super-FRS und dem Ringkoplex CR-RESR-NESR ganz neue Möglichkeiten, da die Intensität der neutronenreichsten Kerne um mehr als einen Faktor 1000 gesteigert werden kann und die Auslegung des Kollektorrings für isochrone Messungen besser geeignet ist als der ESR. Damit wird die NUSTAR Anlage ein wichtiges Gerät zur Erforschung der r-Prozess Kerne im Labor.

Contents

Chapter 1

Introduction

The mass of a nucleus, and thus its binding energy, is one of the most basic nuclear property. All strong and Coulomb interactions contribute to the total nuclear binding energy, which determines their masses. Mass measurements far from the valley of stability are of primary interests for nuclear structure research. The chart of nuclides with the presently known masses is shown in Fig. 1.1.

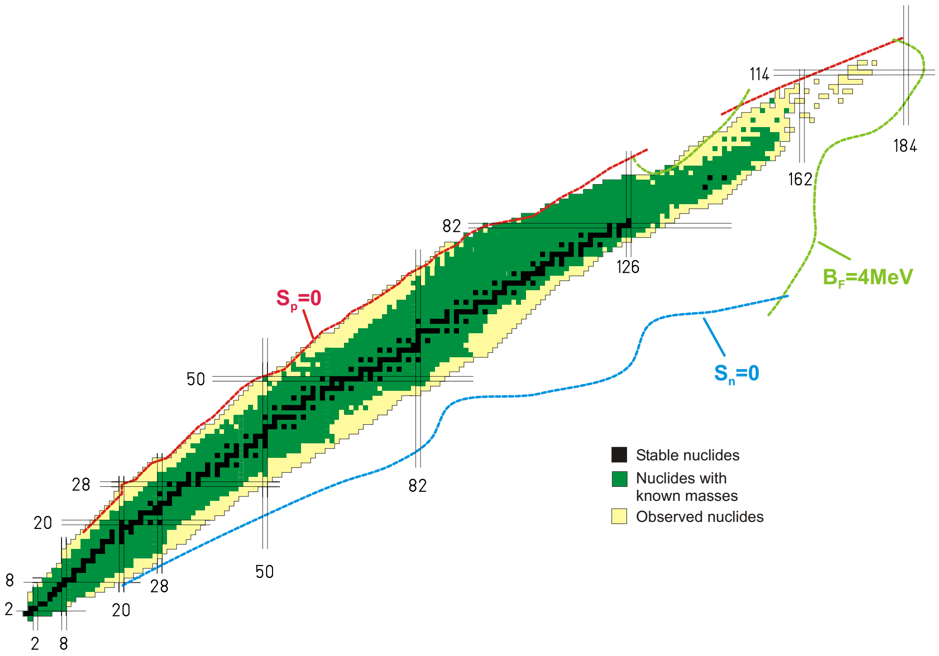

Figure 1.1: Chart of nuclides with presently known masses (green area) [ABW03]. The proton and neutron driplines and the fission barrier are the borders for the existence of nuclei. The area of neutron-deficient nuclides is almost fully covered with measured masses, whereas the neutron-rich region is still a *Terra Incognita*, where the neutron dripline is not observed for Z>8.

1.1 Motivation

Masses of nuclides intrinsically provide essential information about nuclear structure. For example, the study of binding energy differences, i.e. separation energies of nucleons can reveal new regions of deformation or the evolution of shell-closures.

Various models have been developed to reproduce measured masses and to predict unknown masses: collective semi-empirical microscopic-macroscopic models [MNMS95], phenomenological microscopic models such as shell-model calculations [LZ76], Hartree-Fock mean-field calculations [SGP03], relativistic mean-field calculations [LRR99], etc. Basic theories predict binding energies, but with a same model also other properties. Various force functions applied in self-consistent mean-field models lead to different predictions and large discrepancies from experimental values, as is illustrated in Fig. 1.2.

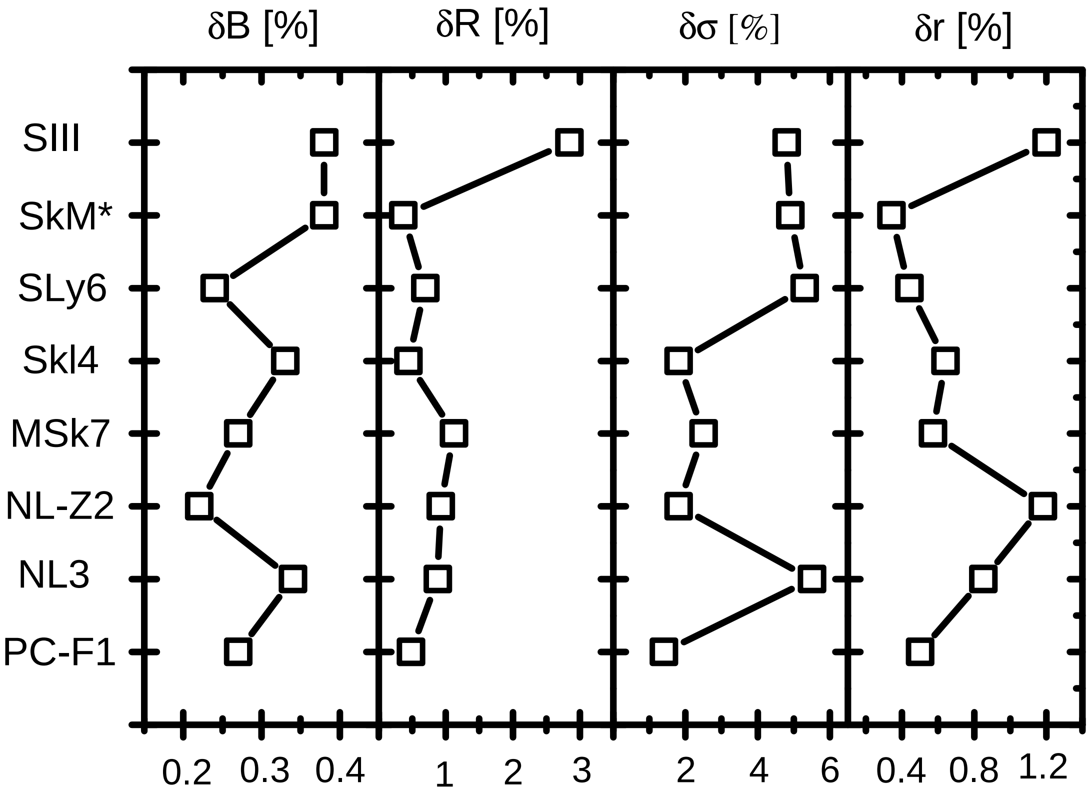

Figure 1.2: Relative error $\delta O = (O_{calc} - O_{exp})/O_{exp}$ calculated for the experimental binding energy δB, charge diffraction radius δR, charge surface thickness $\delta\sigma$, and charge rms radius δr for various nuclear forces functions in self-consistent mean-field model [BHR03]. The predictive power of the different forces is illustrated.

The predictive power of these models developed from existing data on stable nuclei can be greatly improved by extending mass measurements to the most exotic nuclei as well as by improving the precision of known masses. Predictions of mass models for exotic nuclei located at the drip-lines, i.e. the limits of stability against the emission of a proton or neutron, diverge from each other by several MeV or even tens of MeV. Much more reliable mass predictions and, consequently, more experimental data are crucial if we are to deeper understand the structure of nuclei.

Determination of masses also play an important role in other fields of physics, such as atomic physics or nuclear astrophysics. In the latter, masses allow to account for the abundances of nuclides or to determine the path of nucleosynthesis processes, such as the rapid neutron-capture (r-) process on the neutron-rich side of the nuclear chart, or the rapid proton-capture (rp-) process on the neutron-deficient side, which proceeds along the N = Z line, therefore close to stability for light nuclei but close to the proton drip-line for heavier nuclei, see Fig. 1.3.

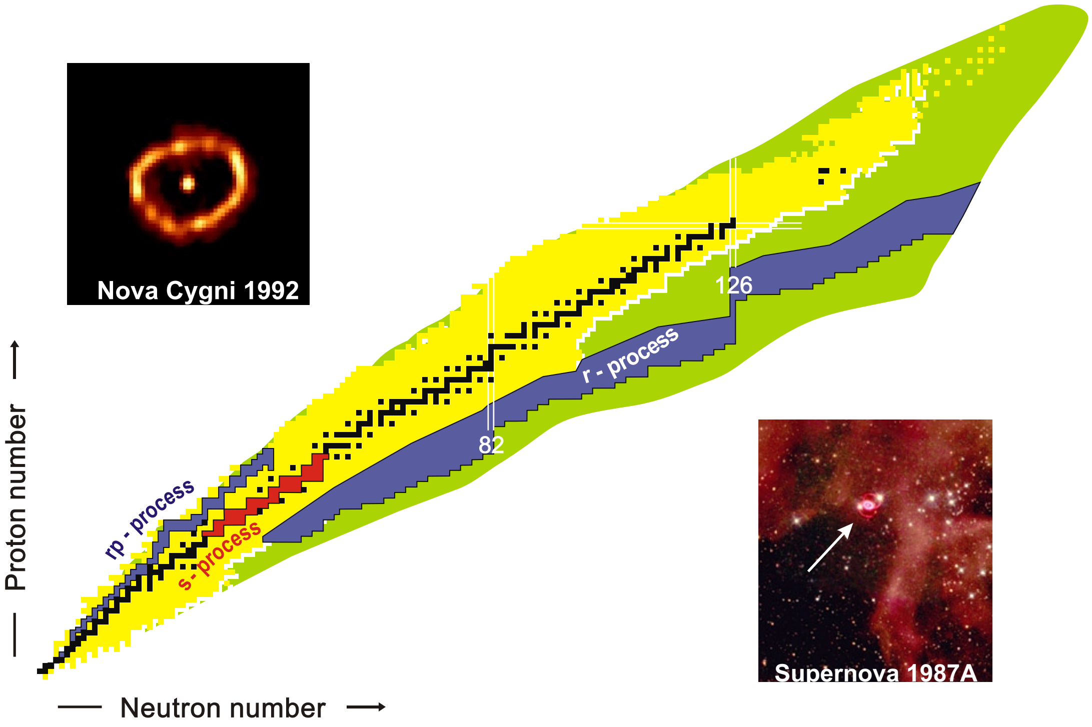

Figure 1.3: Relevance of exotic nuclei for nuclear astrophysics. The chart of the nuclides showing the stable nuclei (black squares) and the observed unstable nuclei (yellow area). The rp-, s- and r- process paths of the nucleosynthesis are also indicated. The insets represent Hubble Space Telescope images of the nova Cygni 1992, a possible site for the rp-process, and afterglow from SN1987A, a r-process site.

1.2 Production and Separation of Exotic Nuclei

An experiment with exotic nuclides requires first their efficient production. As these nuclides are produced in different nuclear reactions together with a huge amount of other less interesting nuclides, the main task is to separate them in a short time.

1.2.1 Production of Exotic Nuclides

There are several reactions used to produce secondary exotic beams. Projectile fragmentation and fission are effective reactions at high energies, which are used in the present study. At low energies the fusion process is also used. The range of isotopes provided by all three processes are shown in Fig. 1.4.

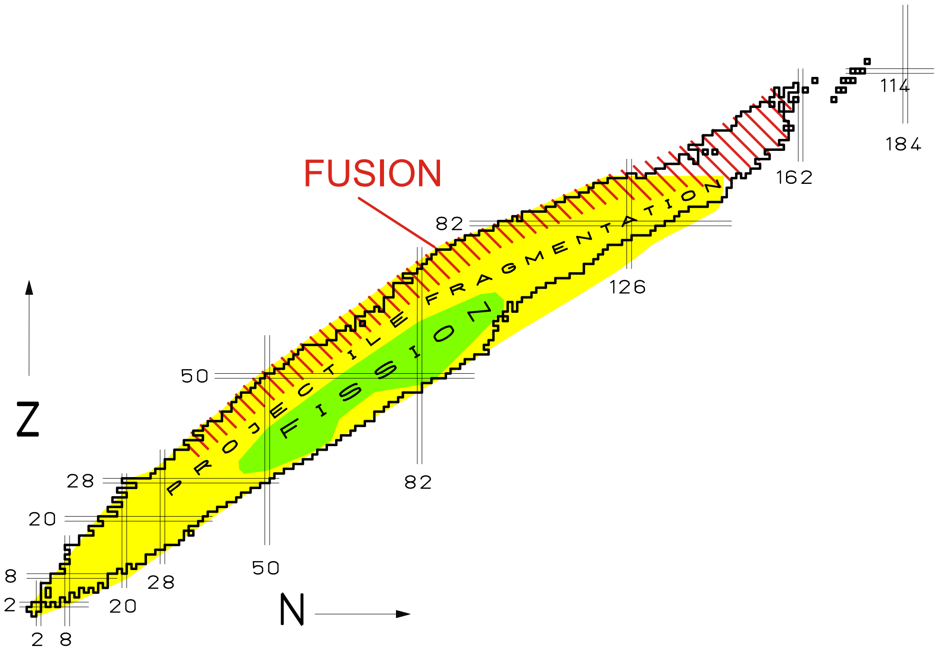

Figure 1.4: Chart of nuclides with areas produced by various reactions, fission (green), fragmentation (yellow) and fusion (red).

Fragmentation provides most of the species and its reaction is ideally suited for high transmission through forward spectrometers like the FRS. Fragmentation products are transmitted by about 50% and more with the FRS. The energy distribution resulting from fragmentation is a few percent and is determined by number of nucleons removed from the projectile.

The energy distribution after the fission process is much wider, which decreases the transmission. On the other hand a high cross-section for the neutron-rich nuclides allows to reach more exotic areas, see Fig. 1.5. The wide energy

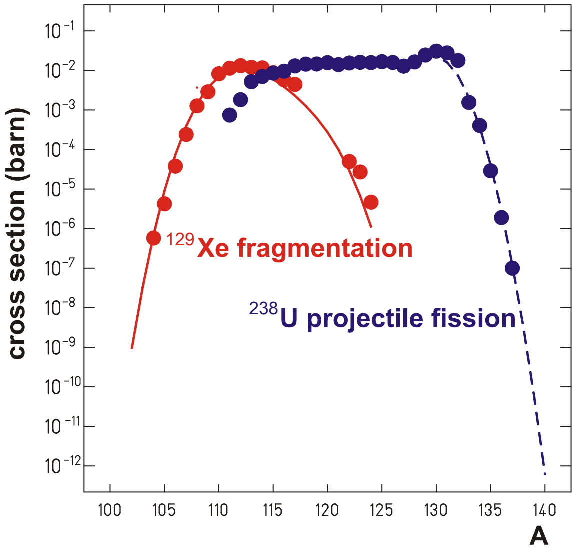

Figure 1.5: Comparison of the cross-section for tin isotopes from fragmentation of ^{129}Xe in a ^{27}Al target [RFK+98] and fission of ^{238}U in a ^{208}Pb target [EBF+99].

distribution makes the separation very difficult, but in our experiment it is an advantage, as more species are required in our experiment. Together with high cross-section in the areas of neutron-rich Sn and Br it makes the fission to be a promising tool for mass measurement in the storage ring ESR. Such measurements are the goal of the experiment described in this work.

Fission of uranium projectile on a beryllium target is described in more detail in following. Depending on the impact parameter b, two different fission mechanisms can occur [Kel03].

For large impact parameters, $b > R + r$ the contribution from electromagnetic interactions is expected, see Fig. 1.6. Electromagnetic interactions ex-

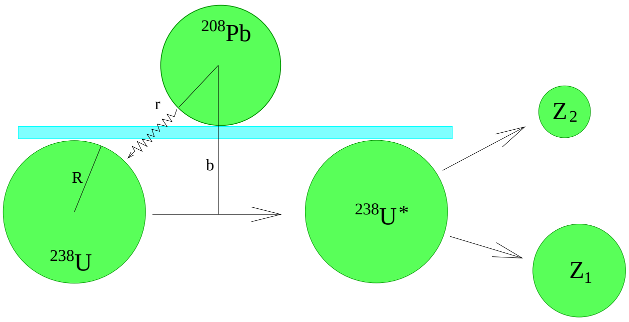

Figure 1.6: Scheme of low energy fission process at relativistic projectile energies. The projectile does not hit the target nucleus but excites via the Coulomb interaction. The projectile fissions into asymmetric fragments due to shell effects.

cite predominantly the low-energy part of the giant dipole resonance at around 12 MeV [SSB+00]. At this low excitation energy, a uranium projectile splits predominantly into a heavier and a lighter fragment, as symmetric splits are strongly suppressed due to shell effects. A schematic example of the mass distribution of fragments produced by electromagnetic induced fission is shown in Fig. 1.7 b). The observed structures are described as a superposition of three different *fission modes* or *fission channels*: two mass-asymmetric channels (*Standard I* and *Standard II*) and a *Superlong* channel at a mass symmetry [BGM90]. According to [BGM90], the fission channels are identified with valleys in the potential-energy surface of the highly deformed system due to shell effects. The Standard I channel is characterized by a spherical heavy fragment around mass number 134 and a deformed light fragment. The Standard II channel is characterized by a deformed heavy fragment near mass 145 and slightly deformed or spherical light fragment. Finally, in the Superlong channel both fragments are strongly deformed.

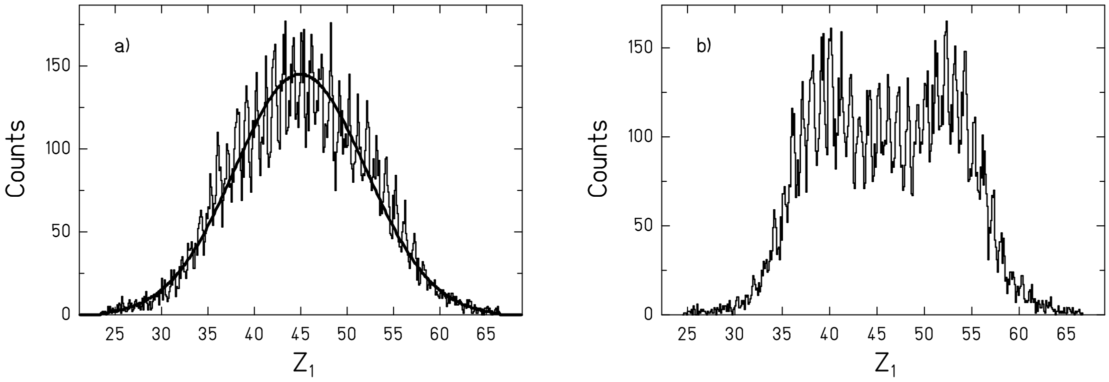

Figure 1.7: Element distribution of the fission fragments produced in the reaction of ^{238}U projectile at 1 A GeV on $(CH_2)_n$ target. **a)** For the fissioning nucleus $Z_1+Z_2=90$ excited with a high energy after a nuclear collision. The full line is the result of a Gaussian fit. **b)** For the fissioning nucleus $Z_1+Z_2=92$ excited with low energy after an electromagnetic interaction. The asymmetric charge distribution of the fissioning nucleus with charge 92 is characteristic of the contribution of low-energy fission. Here, the excitation energy is induced by electromagnetic interaction or very peripheral nuclear collisions where only few neutrons are abraded. [JA02]

For a smaller impact parameter, $b < R + r$, see Fig. 1.8, nuclear collisions between the projectile and the target nucleus occur. A number of nucleons are removed from the projectile, and a so called prefragment is formed. Due to the excitation energy induced of about 27 MeV per abraded nucleon [GS91] the shell effects are washed out, and the prefragment fissions into two fragments of similar masses, see Fig. 1.7 a). This is the case of high-energy or symmetric fission. Because of the excitation energy induced, several particles, mostly neutrons, are evaporated prior to the fission as well as from the fission fragments. Consequently, fission fragments formed in the high-energy fission are less neutron rich compared to fragments formed in the low-energy fission.

The contributions from both these mechanisms to the total uranium fission cross-sections depend on the target size. With increasing the target size, the electromagnetic induced fission becomes more important.

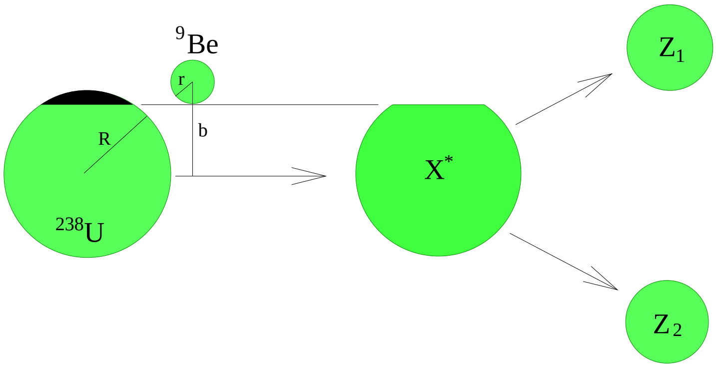

Figure 1.8: Scheme of high energy fission process. The projectile hits the target nucleus and removes several nucleons. The highly excited prefragment fissions into a symmetric Z-distribution.

1.2.2 In-Flight and ISOL Techniques

Various ion species are produced in the nuclear reactions and therefore separation techniques have to be applied to get rid of contaminants. Two main complementary separation principles are applied in exotic beam facilities, the Isotope Separation On-Line (ISOL) and the In-Flight Separation [GMR95].

In the ISOL device the reaction products are stopped in a thick target, thermalized and transported to an ion source by diffusion. The ions are ionized there to be accelerated to kinetic energies in the range of 10–100 keV. Electromagnetic fields separate the nuclei according to their mass-to-charge ratio. The scheme of the ISOL technique is shown in Fig. 1.9.

A complementary separation method is in-flight separation. It allows a wide energy range of projectiles, from the Coulomb barrier up to several GeV/u. The principle of the method is compared with the ISOL technique in Fig. 1.9. The target used is thinner than in an ISOL facility and reaction products have therefore high energies. The separation is performed by ion-optical systems, that comprises electric (only up to medium energies) and magnetic fields.

An in-flight separator is not limited by the diffusion processes like the ISOL technique and can produce a separated secondary beam of exotic ions with half-lives shorter than microseconds. The ISOL system is limited to lifetimes longer

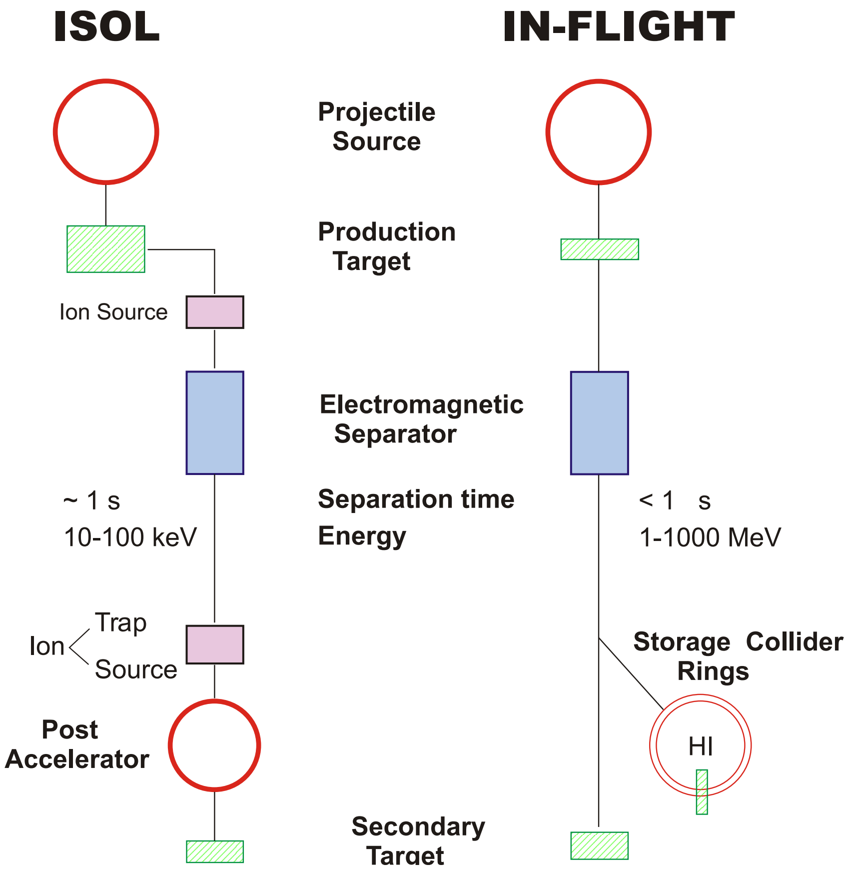

Figure 1.9: Comparison of the two main methods for production and separation of secondary nuclear beams, the ISOL and In-Flight techniques. In the ISOL device the reaction products are stopped in the thick target, thermalized and transported by diffusion to an ion source. In the In-Flight method a thinner target is used and reaction products enter the electromagnetic separator with high kinetic energies. [GMR95]

than 10 ms and is depending on the chemical characteristics of the target. The ISOL technique is superior in beam intensities for most of the elements and provides beams of smaller emittance. Presently, techniques combining both features are developed. For example, the ISOL devices are coupled to post-accelerators to produce high quality beams of high energy exotic ions.

1.2.3 Exotic Nuclear Beam Facility at GSI - the Fragment Separator FRS

The research center GSI (Gesellschaft für Schwerionenforschung) in Darmstadt consists of several facilities. The linear accelerator (UNILAC) accelerates most of the chemical elements up to uranium to a kinetic energy of about 10 MeV/u, see Fig. 1.10.

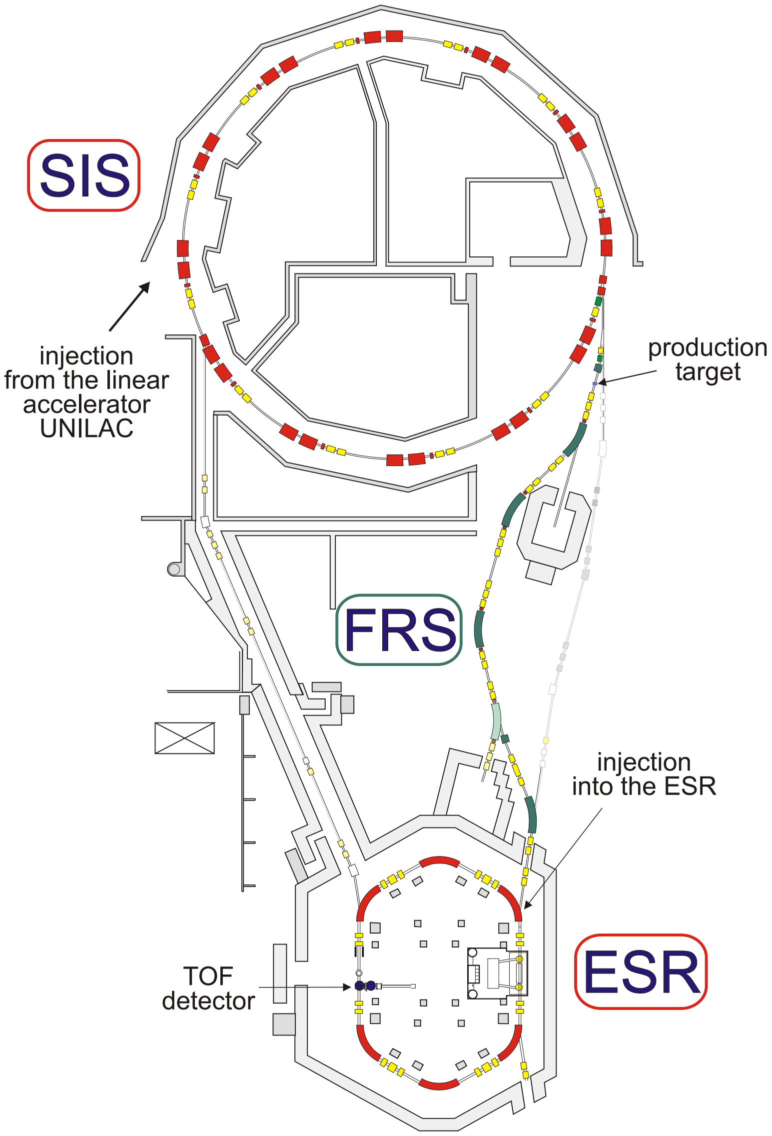

Figure 1.10: A scheme of the high energy part of the GSI research facility. The ions are injected from the linear accelerator UNILAC into the heavy ion synchrotron (SIS), where they are accelerated to relativistic energies. An extracted primary beam produces a secondary beam of exotic nuclides in the fragment separator (FRS). The ions are separated in-flight and injected into the storage ring (ESR).

The beam can be transfered into the heavy ion synchrotron (SIS) [BBFP85]. The ions are accelerated to relativistic energies up to 2 GeV/u for the lighter and 1 GeV/u for the heavier ions. The maximum magnetic rigidity is about 18 Tm.

Subsequently the ions are extracted and delivered into experimental areas, a storage ring (ESR), but also an irradiation area for the tumor therapy project at GSI [KBB+91, KW03].

A secondary nuclear beam can be produced in the target at the entrance to the fragment separator (FRS) [GAB+92]. The secondary beam can be delivered to the experimental areas or injected into the storage ring ESR [GBB+92], see Sec. 1.4.

The FRS is an in-flight separator for relativistic heavy ions, that consists of two stages. Each stage consists of two dipole magnets and a set of quadrupole lenses and sextupole correction magnets.

In the target the primary beam produces a secondary nuclear beam of exotic ions [GMR95]. These are separated in-flight according to their magnetic rigidity (Bρ) by the FRS and delivered to experimental areas.

The separation of ions with similar mass-to-charge ratios but different proton numbers Z can be performed by an energy absorber — degrader placed in the focal plane (Bρ-ΔE-Bρ method) [GAB+92, SG98]. The energy losses in the matter for various elements depend on Z^2 [Bet30]. Consequently the ions with a same magnetic rigidity before the degrader but different proton number Z will have a different magnetic rigidity after the degrader and can be easily separated. The achievable separation is improved by a wedge-shaped form of the degrader.

The nuclides produced at the FRS target can be separated by the Bρ-ΔE-Bρ method into an isotope-pure beam. A complete separation of nuclides of higher atomic numbers (which is a case for uranium fission) is more difficult due to the larger number of possible charge states [MGV+95].

1.3 Methods of Mass Measurement

Masses of nuclides are one of the nuclide characteristics, which has been of great interest from the beginning of the nuclear physics history. A pioneer in mass measurements was F. W. Aston [Ast33], who made systematic measurements of some 200 nuclides. Nowadays mass measurements are pursued worldwide. The present mass values of more than 1900 nuclei are the results of more than 500 experiments [Bol97].

The methods of mass measurements are usually divided into two groups: direct and indirect methods. If a mass measurement yields from a mass difference of a few masses in a nuclear reaction (Q-value) it is called a indirect mass measurement. If a measured mass is compared to a known masses it is called a direct mass measurement.

1.3.1 Indirect Methods

Indirect mass measurement methods are based on energy conservation,

$$\sum M_{initial}c^2 = \sum M_{final}c^2 + Q \tag{1.1}$$

where $\sum M_{initial}$ is the sum of initial masses, $\sum M_{final}$ is the sum of final masses, c is the speed of light and Q the reaction energy. If all masses except one are known and the Q-value is measured, the unknown mass can be determined.

1.3.1.1 Nuclear Reactions

Nuclear reactions are traditionally one of the most accurate mass measurement techniques. Especially neutrons offer the possibility of high accuracy via (n,p) or (n,α) reactions [WWG01] and (n,γ) decays. For example, the energy of the ^{1}H(n,γ)^{2}H reaction was determined with precision of only 0.4 keV [KDD$^+$99]. Due to the fundamentals of the methods, also the mass of an unbound nuclide can be measured if it is a product of the reaction. No direct technique is applicable in this case, since the measurement time would be too long. In this way the mass of unbound $^{13-16}$B [KBvO$^+$00], ^{13}Be [BKP$^+$98, LGZ$^+$98] and ^{18}Na [Zer01] were recently measured. The latter one was obtained using the invariant mass spectroscopy, where also the momentum conservation law is used and momenta and angles of particles are measured to reconstruct the reaction process [Pen01].

1.3.1.2 Decays

Radioactive decay can provide relatively accurate mass measurement. The measured kinetic energy of an α-particle, a β-particle or an emitted nucleon can be used to derive the mass of the daughter or mother nucleus. However the measurement can use a known mass value which can be incorrect and induce a cumulative error. In addition, it is often difficult to get complete spectroscopic information. A good knowledge of decay branches is required especially for β-decays, where an additional determination of the detector response function is crucial to correctly determine the endpoint energy. For example, masses around ^{132}Sn were measured from β-decay [FMM$^+$98], mass of ^{60}Ga was determined at GSI [MJD$^+$01]. Measurements of Q_α and Q_p are very powerful for heavy nuclides at the drip line, especially in superheavy-element areas [HHA$^+$00, HHA$^+$01].

1.3.2 Direct Methods

Most precise methods of mass determination rely on the measurement of frequencies. The mass is determined using an equation for the cyclotron frequency f_c in a magnetic field B

$$f_c = \frac{1}{2\pi}\frac{Bq}{m\gamma} \tag{1.2}$$

Such measurements can be performed in Penning traps. Penning traps consist of a static quadrupole electric field formed by a set of electrodes providing axial confinement and a static magnetic field providing radial confinement of an ion. This offers the possibility of storing ions for long periods of time. The cyclotron frequency is determined using a resonant RF-excitation of the ion motion, followed by a time-of-flight (TOF) measurement. If the excitation frequency is in resonance, the TOF shortens. More than 200 masses with a typical accuracy of about 10^{-7} were measured by ISOLTRAP [HAA⁺03]. Recently, this technique has been improved by using clusters of ^{12}C, which defines the atomic mass unit, for calibration and by other technical developments. A mass accuracy of about 10^{-8} has been achieved [BAB⁺03, BBH⁺03].

More Penning trap facilities are built worldwide. JYFLTRAP in Jyväskylä presented first results recently [KEH⁺03, Kol03]. Masses of ^{4}He and ^{3}He with uncertainties of 3×10^{-10} and 9×10^{-10} respectively were measured at the SMILETRAP in Stockholm [FCD⁺01]. New Penning trap facility SHIPTRAP at GSI [SAA⁺03] aims for mass measurements of superheavy elements.

The MISTRAL experiment based on a radiofrequency transmission spectrometer allows precision mass measurements of nuclides with particularly short half-lives. It measures frequency ratios for two different masses in the same homogeneous static field. Recently a high accuracy mass determination of the halo nuclide ^{11}Li was performed [LAB⁺03].

The SPEG spectrometer at GANIL combines time-of-flight measurements with rigidity analyses. The projectile-like fragments are selected using the beam analysis spectrometer and transported along a beam line to the focal plane of SPEG, where the magnetic rigidity $B\rho$ of each ion is derived from a position measurement. The time-of-flight is measured using micro-channel plate detectors located near the production target (start signal) and at the final focal plane (stop signal). The mass m of the particle with charge q and velocity v is deduced from the relation

$$B\rho = \frac{\gamma m v}{q}, \tag{1.3}$$

where γ is the Lorentz factor. The measurement of the masses of proton-rich nuclei with $32 \leq Z \leq 35$ has been made recently [LLSA⁺02].

At Los Alamos neutron-rich nuclei are produced via spallation and fission of the proton beam on a thin Th target. Products are separated by a mass-to-charge filter and transmitted to TOFI. The isochronous recoil spectrometer TOFI is a highly symmetrical system, which has been arranged such that the flight time of an ion with a particular mass-to-charge ratio is independent of the ion's velocity. A flight-time of an ion with an unknown mass is compared with the flight-time of a reference ion. Masses of 48 neutron-rich nuclei extending from ^{55}Sc to ^{75}Cu have been determined in 1998 [BVSW98].

Both SPEG and TOFI perform measurements with lower uncertainty of about 0.5 MeV.

The resolution in time-of-flight measurements is limited by the total flight time. If this can be increased, then a corresponding gain in resolution is possible. This can be achieved in multi-turn devices. At GANIL a coupled-cyclotron complex CSS1-CSS2 is used for mass measurements. The primary beam is accelerated in the CSS1 and bombards a production target, creating proton-rich nuclides via fusion-evaporation, which are injected and accelerated in the CSS2. To be accelerated by a cyclotron with the radio-frequencies applied to cavities f_c ($\omega_c = 2\pi f_c$) a particle with mass m_c and charge q_c has to fulfill the cyclotron equation

$$\frac{B}{\omega_c h} = \gamma \frac{m_c}{q_c}, \tag{1.4}$$

where h is a harmonic and γ a Lorentz factor. The disadvantage of the method is that only ion species within a short band of mass-to-charge ratios can be accelerated simultaneously. For two nuclei with mass-to-charge ratios m/q and $m/q + \delta(m/q)$ the accumulated difference in the time-of-flight δt determines $\delta(m/q)$ by

$$\frac{\delta t}{t} = \frac{\delta(m/q}{m/q}. \tag{1.5}$$

A new mass is determined using a known reference mass and measuring the flight time by a high-resolution spectrometer system. A micro-channel plates detector provides a start signal before the injection into CSS2 and and a plastic scintillator provides a stop signal after acceleration. Recently mass measurements of the N=Z nuclei ^{80}Zr, ^{76}Sr, and ^{68}Se were performed [LAM+01].

A storage ring is used as a multi-turn device at GSI for mass measurements. It is described in more detail in Sec. 1.4.

1.4 Mass Spectrometry at the Storage Ring ESR

At GSI the storage ring ESR coupled to the in-flight fragment separator FRS is used for mass measurements [GAB+01].

The ESR was constructed in order to store relativistic heavy ions [Fra87]. The ESR consists of 6 dipoles, that bring the beam on a closed orbit, as well as 20 quadrupoles and 8 hexapoles, see Fig. 1.11. The path length at the central orbit amounts to 108.36 m. The storage ring can store fragments separated by the FRS or a primary beam with a magnetic rigidity of 0.5–10 Tm. The ring is operated under ultra high vacuum (UHV) conditions . The pressure amounts to about 5×10^{-11} mbar, which enables ion storage times of several hours. The apertures of the dipole magnets are 220 mm in the horizontal and 70 mm in the vertical directions. The corresponding values for the quadrupoles are 300 mm in the horizontal and 120 mm in the vertical direction. These relatively large horizontal apertures enable the simultaneous storage of ions with a momentum acceptance of about 2.5% (in the non-isochronous ion optical mode). For storing the beam, the septum magnet bends the ions onto the injection line from where they are injected by the kicker magnet on a closed orbit.

The ESR is equipped with an electron cooler [ABE+90, SBB+00] (up to 240 keV electron energy; 1A electron current) and a stochastic cooler [BCF+00].

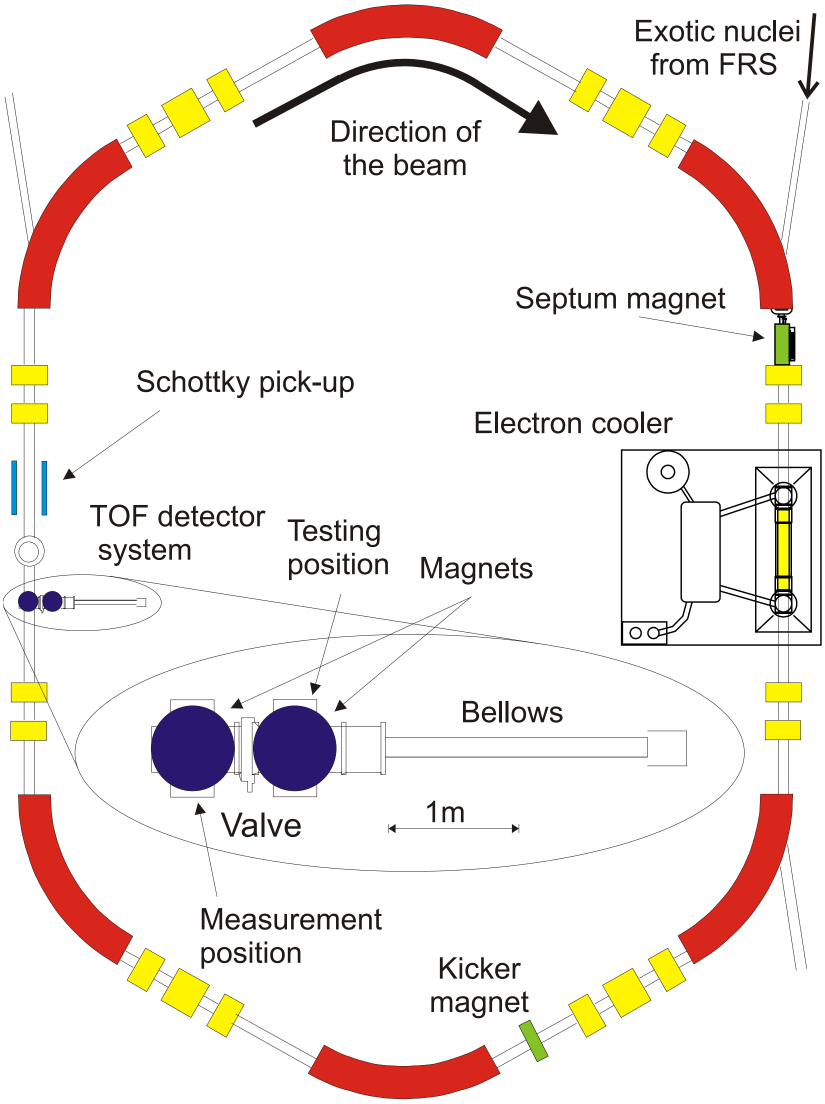

Figure 1.11: Lattice of the storage ring ESR. A beam of exotic nuclei produced at the FRS is injected by the septum magnet into the ESR. The kicker magnet corrects the beam to revolve on a closed orbit. The beam can be cooled by the electron cooler. A detection of the beam is provided by Schottky pick-ups or the TOF detector, which can be placed inside the ring for the measurement or outside when is not needed.

The internal gas target can be used for scattering, charge exchange experiments etc [RBF+97]. The beam can be decelerated by radio frequency cavity. The stability of the magnet fields is about 10^{-6}. This excellent stability is in particular required for precision experiments such as mass measurement.

The detection of the beam is provided by Schottky pick-ups or the TOF detector, which can be placed inside the ring for the measurement or outside when is not needed, see Fig. 1.11.

1.4.1 Mass Measurements

Two complementary techniques have been developed at the ESR and have been used in several experiments for mass measurements, Schottky-Mass-Spectrometry (SMS) for cooled beams of longer-lived isotopes [RKS+97, RGM+00] and Isochronous-Mass-Spectrometry (IMS) for uncooled beams of short-lived fragments [HSA+01]. Both methods are based on precise measurements of the revolution frequency which unambiguously characterizes the mass-to-charge ratio of the circulating ions. The relative difference in the revolution frequencies $\Delta f/f$ depends on two components: the difference in mass-to-charge ratios $\Delta(m/q)/(m/q)$ and the difference in velocities $\Delta v/v$ according to

$$\frac{df}{f} = -\alpha_p \frac{d\left(\frac{m}{q}\right)}{\frac{m}{q}} + \left(1 - \frac{\gamma^2}{\gamma_t^2}\right)\frac{dv}{v}, \tag{1.6}$$

where γ is the Lorentz factor and γ_t is a transition point. For more details on the equation see Sec. 3.1.1. The equation can be used for mass determination, if the second part goes to zero

$$\left(1 - \frac{\gamma^2}{\gamma_t^2}\right)\frac{dv}{v} \rightarrow 0. \tag{1.7}$$

This can be achieved for SMS and IMS using different approaches, see Fig. 1.12.

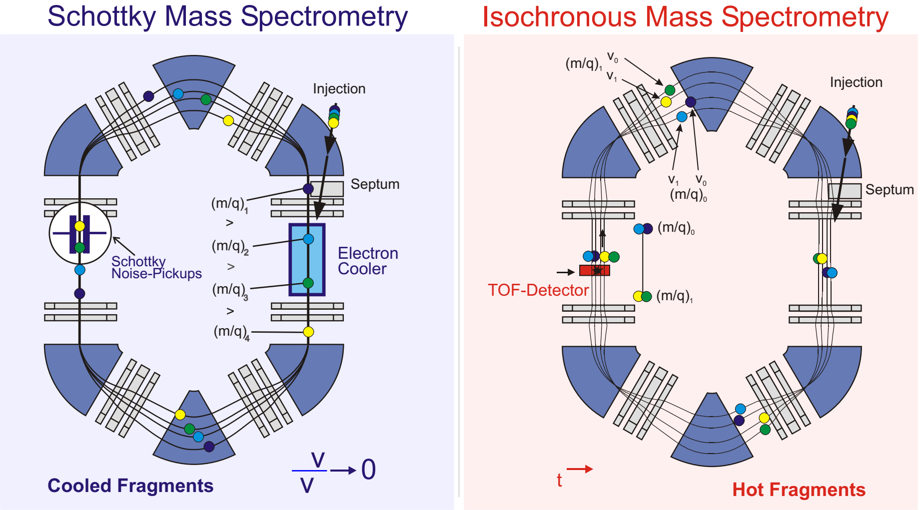

Figure 1.12: Comparison of the two methods for mass measurements at the storage ring at GSI. In SMS the velocity spread of the heavy-ion beam is reduced by electron cooling. In IMS the storage ring is in the isochronous ion-optical mode, so that all ions of one species should revolve with the same revolution time independent of its velocity.

In SMS the velocity spread of the heavy-ion beam is reduced by electron cooling. This is achieved by merging the relativistic hot fragments with a cold electron beam, see Fig. 1.12, so that $dv \to 0$ and (1.7) is fulfilled. Masses are determined from revolution frequencies which are obtained by a Fourier transformation of their signals induced in Schottky pick-up probes at each turn in the ring. New masses were determined for the first time in two experiments where neutron-deficient nuclei were produced by fragmentation of bismuth [RGM+00, Lit03]. Due to the slow electron cooling the measurements are limited to nuclides with half-lives longer than 1s.

In IMS the storage ring is in the isochronous ion-optical mode, so that all ions of one species should revolve with the same revolution time independent of its velocity [WSB86, WBB+97, HBD+98]. This can be described mathematically as $\gamma \to \gamma_t$ and (1.7) is fulfilled. The revolution frequency is measured by a fast time-pickup detector mounted in the storage ring aperture, see Fig. 1.12. Typically the ions make several hundred turns in the ESR and at each revolution they pass through a very thin carbon foil, where secondary electrons are released. These produce a signal in micro-channel plates. The TOF detector is described in more detail in Sec. 1.4.2. New masses are determined from comparison of the time-of-flight of the unknown masses with those the known reference masses [HAB+00]. The method is suited for the mass measurement of extremely short-lived nuclides of the order of several tens of μs.

The IMS technique was used in the experiment described in this thesis.

1.4.2 The Time-of-Flight Detector

The revolution time of the ion in the experiment described in this work was measured by the Time-of-Flight detector, see Fig. 1.11–1.14. This detector has to fulfill the requirement of high efficiency, low energy losses and low charge exchange [TBE+92, Trö93, Rad94].

The detector is based upon a principle that is described in [BH78]. Ions pass through a thin carbon foil (about 20 μg/cm^2), which is covered on both sides with 10 μg/cm^2 CsI [THKL99], as shown in Fig. 1.15. Electrons, produced by the ion interacting with the foil, are guided by electric and magnetic fields to Micro-Channel-Plate (MCP) detectors in a Chevron arrangement. The arrangement of the fields forces the secondary electrons to move on cycloid trajectories. This makes the movement of the electrons isochronous and eliminates the influence of different emission angles or energies of the electrons on the time information.

The electric field is produced by an arrangement of potential plates, which are placed in the vacuum of the detector chamber. The magnetic field of about 0.5×10^{-2} – 1×10^{-2} T is produced by a couple of Helmholtz coils that are mounted above and below the detector chamber.

The electrons hit the channel plates, where secondary electrons are produced. These are accelerated by the high voltage and produce other electrons on the walls of the micro channels. This generates an avalanche effect, so the accumulated

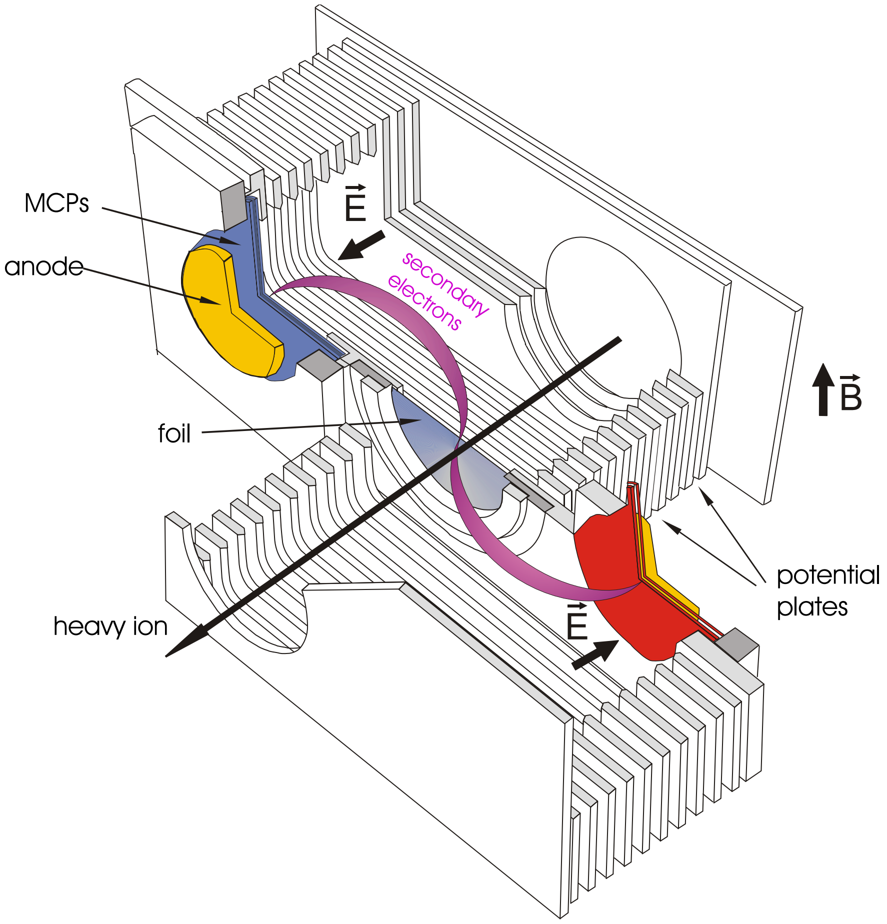

Figure 1.13: Schematic layout of the time-of-flight detector. Only one side is shown. The Helmholtz coils are located below and above the vacuum chamber. The ions penetrate the carbon foil coated with CsI and produce secondary electrons. These are transported by magnetic and electric fields on the Micro-Channel-Plate detectors (MCP) [TBE$^+$92, Trö93, Rad94].

charge on an anode behind the channel plates generates a signal with an amplitude of up to 1V and a length of several nanoseconds. The signal is transmitted by a high quality coaxial cable out of the vacuum. The obtained time precision amounts to about 40ps and the detection efficiency, depending on the ions amounts to 30–50%.

The ESR is designed to store ions also over hours and to operate under an ultra high vacuum (UHV). The pressure in the operative ESR amounts to only several 10^{-11} mbar. The detector system is constructed that it fulfills also these requests. It consists only of electropolished stainless steel, ceramics and glass in order to withstand high temperatures up to 400°C during the backing of the ESR and to guarantee optimal surface characteristics for the vacuum use.

During the standard use of the ESR the detector is placed in an outside

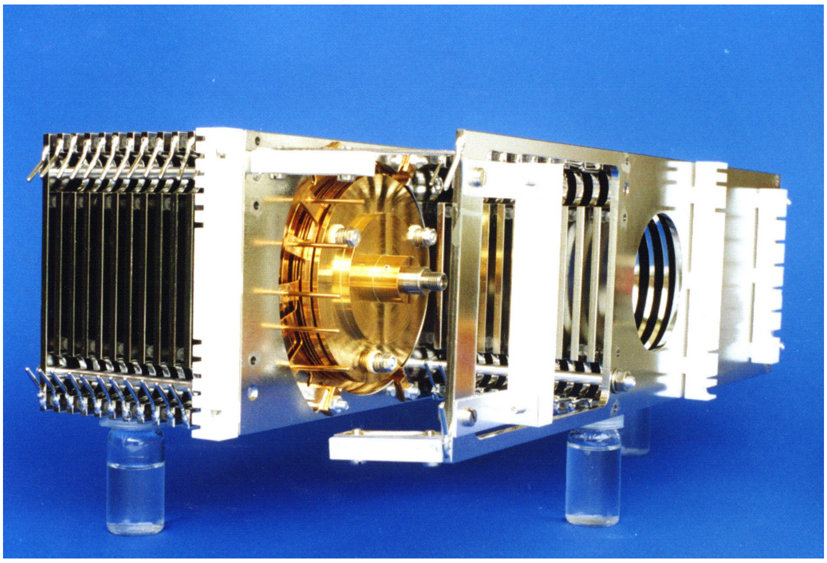

Figure 1.14: A photo of TOF detector. The detector is without cable connection and the Helmholtz coils [TBE+92, Trö93, Rad94].

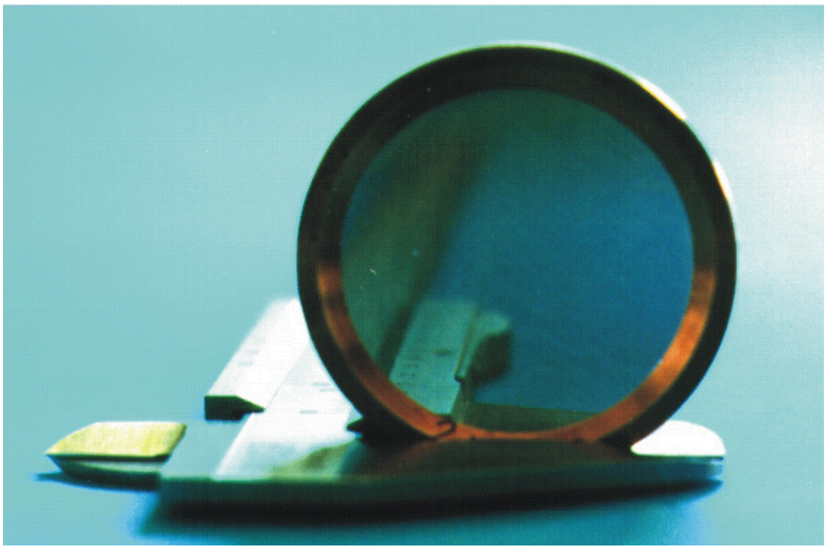

Figure 1.15: Photo of a carbon foil coated by CsI. The ions interact with the foil and produce secondary electrons.

chamber that is detached from the storage ring by a valve. There its functionality can be checked by a laser. For an experiment the detector can be positioned in the center of the ring aperture. The foil has a diameter of 40 mm, which limits the usable aperture of the beam at this place. The high voltage supply and magnet current can be operated remotely during an experiment.

Chapter 2

Preparation of the Experiment

As mentioned above, nuclidic masses are very important for various fields of physics. Especially the area of neutron-rich nuclides is not well investigated. The astrophysical r-process is not described, the neutron dripline is not reached yet and is therefore unknown. Due to the non-existence of the Coulomb interaction for the neutron, this dripline is further from the stability line than it is in the proton case. It is therefore more difficult to reach this area. A solution for a part of this region can be the production with the fission process, as was shown in Fig. 1.5.

The goal of the experiment described in this work was to measure masses of neutron-rich products of ^{238}U fission. This was challenging task, as fission fragments were injected into the ESR for the first time. On the other hand, it was possible to achieve they afford high rates in the neutron-rich areas, which is not possible by fragmentation.

2.1 Simulation of Experiment

To predict characteristics of mass measurements with the isochronous mass spectrometry, the simulation program TOFSIM was developed in the framework of this thesis.

2.1.1 The Simulation Program TOFSIM

TOFSIM is a simulation program of the time-of-flight mass measurement experiment with the ESR in the isochronous mode.

The TOFSIM requires an output from the MOCADI program [IGM$^+$97, SGM$^+$88], which simulates the production and movement of single ions through the FRS. In TOFSIM, the revolution time of particles is determined from their energy using the isochronicity curve (for more see Sec. 3.1.2). In the experiments the dependence of the revolution time on the cooling voltage was measured. These data can be converted into a magnetic rigidity or energy vs. revolution time representation.

Since isochronicity curves were measured only for some cases, to have it for a certain isotope it has to be transformed, see also Sec. 3.1.3.

The velocity of an ion v with the mass-to-charge ratio m/q can be calculated using the equation for the magnetic rigidity

$$B\rho = \frac{m}{q}\gamma v = \frac{m}{q\sqrt{\frac{1}{v^2} - \frac{1}{c^2}}}. \tag{2.1}$$

Therefore the velocity is

$$v = \frac{1}{\sqrt{\left(\frac{m/q}{B\rho}\right)^2 + \frac{1}{c^2}}}. \tag{2.2}$$

The revolution trajectory for the measured isotope with the $(m/q)_{exp}$ ratio, the magnetic rigidity $B\rho$ and the revolution time τ_{exp} is

$$C = \frac{\tau_{exp}}{\sqrt{\left[\frac{(m/q)_{exp}}{B\rho}\right]^2 + \frac{1}{c^2}}}\ . \tag{2.3}$$

It is obvious, that for one setting the revolution trajectory depends on the magnetic rigidity only. The revolution time transformed for $(m/q)_{tran}$ is then

$$\tau_{tran} = C \times \sqrt{\left[\frac{(m/q)_{tran}}{B\rho}\right]^2 + \frac{1}{c^2}}\ . \tag{2.4}$$

The transformation for a different setting is based on the approximation, that is good enough for our purposes. In the first order approximation the central orbit C_0 is same for central rigidities $B\rho_{10}$ and $B\rho_{20}$. Other orbits are the same in case the relative difference from the central $B\rho_{10}$ is the same for the measured and transformed rigidity,

$$C_1(B\rho_1) = C_2(B\rho_2) \qquad \text{if} \qquad \frac{B\rho_1}{B\rho_{10}} = \frac{B\rho_2}{B\rho_{20}}. \tag{2.5}$$

The revolution time is calculated using Eq. 2.3 and 2.4 with corresponding rigidities.

Only some particles, which have reached the ESR, will also be injected. Simulated particles are selected by the injection acceptance. It can be adjusted for the magnetic rigidity, vertical and horizontal position, and angle.

Using the procedures mentioned above, a simulated spectrum is produced. It can be drawn and compared with a real experimental spectrum, see Fig. 2.1. Simulated spectra (red) are in the lower part, experimental spectra (blue) in the upper part. The program TOFSIM is described in more detail in Appendix A.

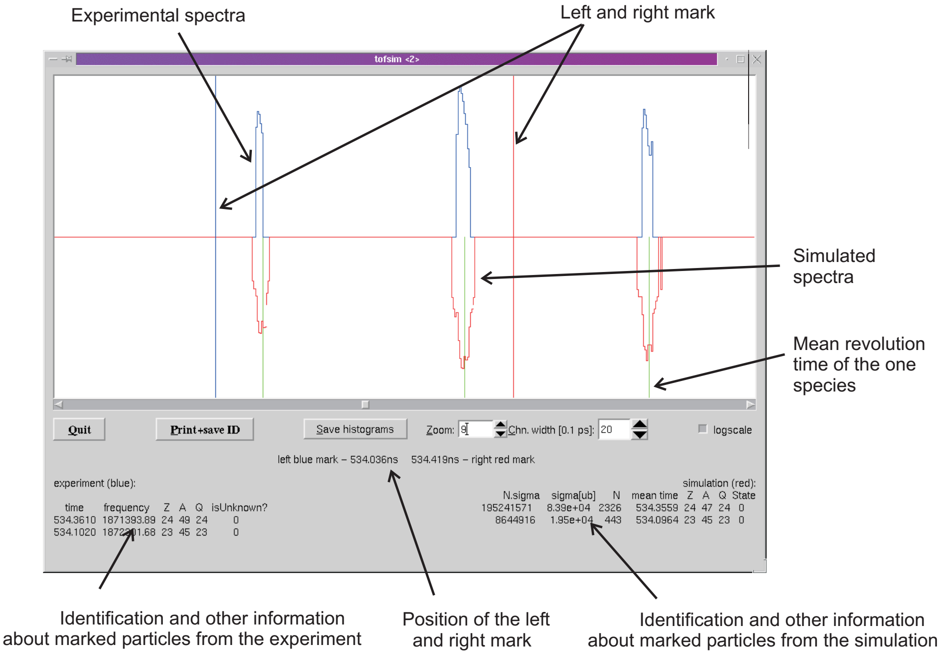

```
left blue mark – 534.036ns    534.419ns – right red mark

experiment (blue):                                                   simulation (red):
                                                  N.sigma   sigma[ub]   N   mean time  Z  A  Q  State
  time     frequency    Z  A  Q  isUnknown?     195241571   8.39e+04  2326   534.3559 24 47 24  0
534.3610 1871393.89   24 49 24     0              8644916   1.95e+04   443   534.0964 23 45 23  0
534.1020 18722[illegible]1.68   23 45 23     0
```

Figure 2.1: The window of the TOFSIM simulation with the the final graph. The graph is divided into lower (red) simulated spectra and upper (blue) experimental spectra.

2.1.2 Parameters defining the Injection Acceptance

In the TOFSIM program the acceptance of the injection into ESR can be adjusted. The correct adjustment can be crucial for a correct simulation.

First, the momentum acceptance has to be set. The experiment described in Sec. 2.2 was done for the standard ESR mode and width of the momentum acceptance was measured as $2\sigma = 0.28\ \%$.

In our case the ESR is in an isochronous mode. This should be reflected by a smaller acceptance. As we can see in Fig. 2.2, the width of the ESR momentum acceptance influences the width of the simulated peak.

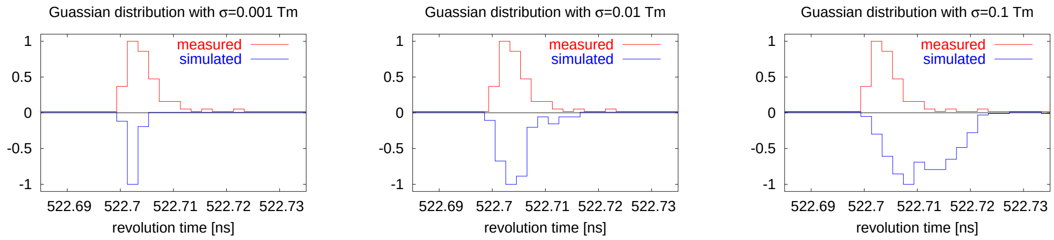

Figure 2.2: Comparison of simulated distributions for different widths assumed for the ESR momentum acceptance with a Gaussian shape (lower) with the measured distribution (upper).

The peak is generated by the TOFSIM simulation using an ESR momentum acceptance in a Gaussian shape with various widths and is compared with a real experimental result measured at $\mathrm{B}\rho = 7.2$ Tm. In the case of the wide momentum acceptance, the peak becomes wider and the mean value is shifted. This is more pronounced if the particle is in the non-isochronous area, as described later in Sec. 4.4.

It is demonstrated, that the best agreement with the experiment is observed for the standard deviation $\sigma = 0.01$ Tm. The simulation is still a little wider than the result from the experiment, so in our simulations we use the momentum acceptance with the width $\sigma \approx 0.1\%$.

2.2 Measurement of the ESR Injection Acceptance

The goal of the experiment was to measure the optical parameters of the injection into the ESR. The beam of $^{58}\mathrm{Ni}^{28+}$ was extracted from SIS and after passing the FRS injected into the ESR, see Fig. 2.3. The ESR was set to the standard mode, but one can also learn from this measurements for the isochronous mode.

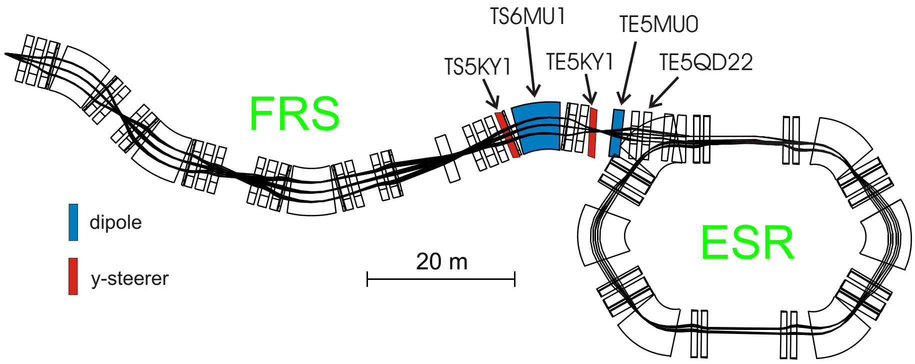

Figure 2.3: Experimental setup used for the measurement of the ESR injection acceptance. The momentum acceptance was measured by varying the energy, the horizontal and vertical acceptance with combinations of the dipoles and steerers marked in the figure. TEQD22 belongs to a group of quadrupole magnets.

The beam had to be narrow to allow a precise measurement, so the beam was cooled by the SIS electron cooler to a relative momentum spread of $\Delta p/p = 10^{-4}$ and an emittance of less than 1 mm mrad.

To measure the transmission, the current of the circulating ions in SIS and ESR was measured. The momentum acceptance was measured by varying the beam energy. The transmission was compared for various energies in the range from 387.9 MeV/u to 401.15 MeV/u.

The results from the measurements of the momentum acceptance is shown in Fig. 2.4. The standard deviation of the distribution is $\sigma = (0.14 \pm 0.01)$ %.

It can be also compared with the injection acceptance for isochronous mode $\sigma = 0.1$ %, see Sec. 2.1.2. That the acceptance should be smaller in case of the isochronous mode, as the ESR requires special settings of the optics, which restricts the injection acceptance.

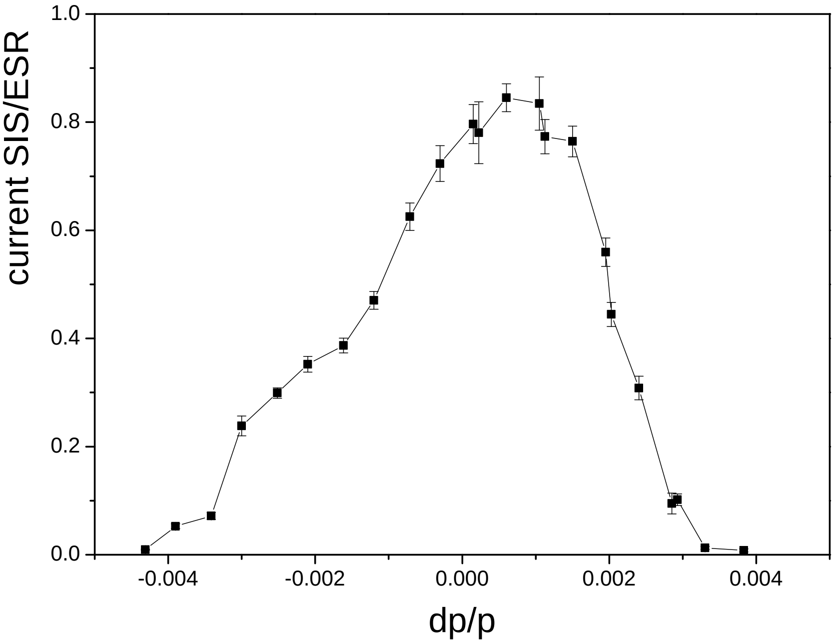

Figure 2.4: The measured momentum acceptance of the injection into the ESR. The values are obtained from the measurements of the transmission of the beam with various energies. The distribution has the width of $2\sigma = 0.28$ %.

The combination of the dipoles TS6MU1 and TE5MU0 allows to measure the X and X' acceptance, analogously the steerers TS5KY1 and TE5KY1 were used to measure the Y and Y' acceptance. The variation of the magnetic fields swept the beam over the full phase space with the $^{58}\mathrm{Ni}^{28+}$ beam with an energy of 391.55 MeV/u.

The measurement of the horizontal acceptance was based on the variation of the fields of the dipoles TS6MU1 and TE5MU0. Their combination allowed to scan the complete phase space. The angle and position of the beam was calculated from the magnet values using the program GICO [WHB88]. The horizontal acceptance was measured in the same way, using the steerers TS5KY1 and TE5KY1.

The results are presented in Fig. 2.5. It shows the horizontal and vertical acceptance 0.47m after the quadrupole TE5QD22.

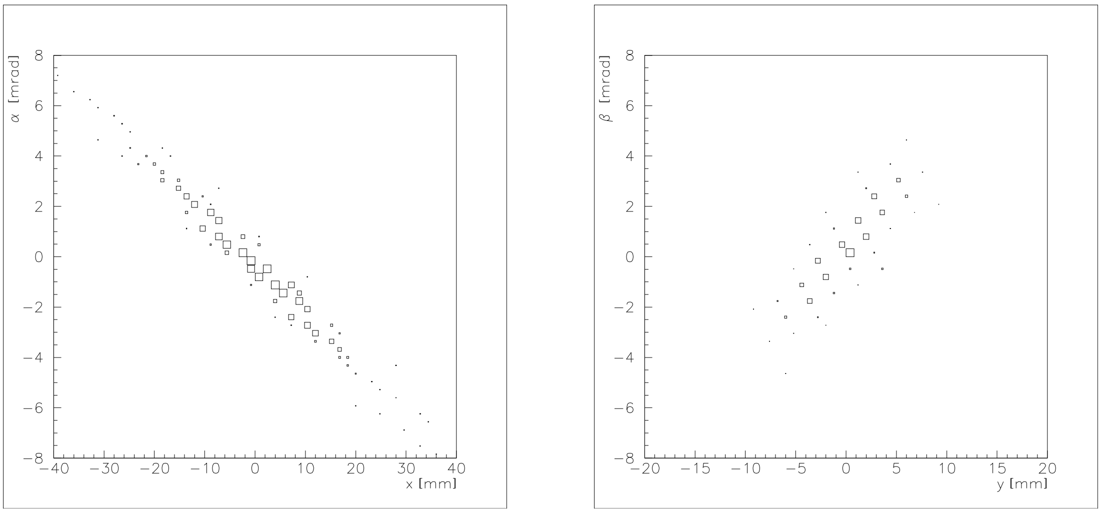

Figure 2.5: ESR horizontal and vertical acceptance of the ion-optical phase space at a position of 0.47m after the TE5QD22 magnet (see Fig. 2.3).

The results show that the momentum acceptance of the injection into the ESR is very narrow compared to the FRS acceptance with a width of FWHM = 2 % [GAB+92], so the transmission into the ESR is reduced at the injection.

2.3 Application of the TOFSIM simulation

2.3.1 Experiment with the ^{70}Zn primary beam

An experiment with a ^{70}Zn primary beam with an intensity of 1×10^{9} particles/spill was carried out. It was the first occasion, where the predictive power of the TOFSIM simulation could be verified.

The simulation of the TOF measurement in the setting with $B\rho = 7.532$ Tm (centered for ^{57}Ti) will be analyzed bellow. The primary beam of the energy 456.4 MeV/u was used to produce projectile fragments in 4g/cm^2 thick beryllium target. In the simulation the cross-section was calculated using EPAX2 formula [SB00]. The phase-space after the fragmentation processes was determined using the model of Goldhaber [Gol74]. During the experiment 6254 injections into ESR were performed in order to improve the statistics.

The simulated and measured spectra are compared in Fig. 2.6. One can see that the simulation describes the pattern in the spectrum very well. This is important for the identification of the nuclides, which was done before searching by hand in the mass-to-charge ratio tables for the same pattern as in the measured spectra. The peaks on the very left side of the experimental spectrum are missing in the simulated spectrum. The reason is, that this is the area of mass-to-charge

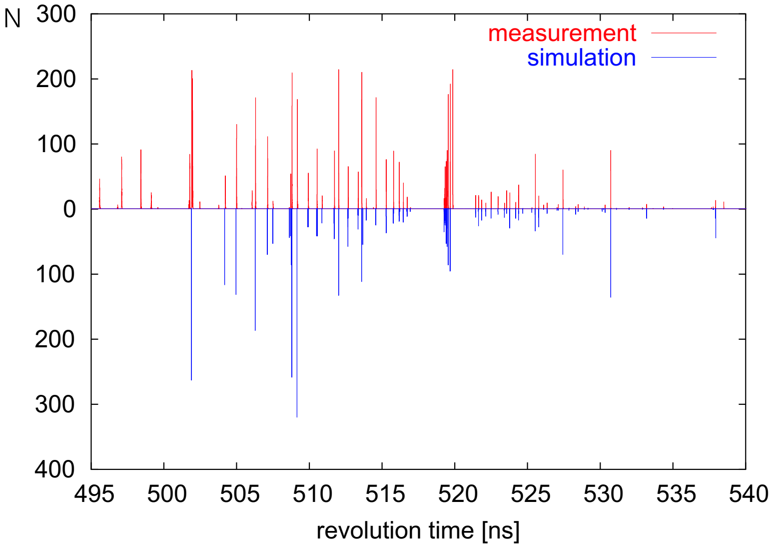

Figure 2.6: Comparison of the simulated (lower) and measured (upper) spectra of fragments produced by the ^{70}Zn primary beam.

ratio, where the transmission though FRS is low, but since the ions are produced with a high cross-section, they can nevertheless be seen in the experiment, but not in the simulation. An enormous number of particles would have to be simulated to have at least a very small number going through FRS. The number of simulated particles reaches the limit of the computer performance, but the transmission is too low and there is no particle transmitted in the simulation.

The preparation of an experiment requires the calculation of expected yields of various species. This is also the task that is fulfilled by the TOFSIM simulation. Together with MOCADI it calculates the transmission and using the cross-section we can predict the expected yield.

The chart of nuclides with yields predicted by the TOFSIM simulation is shown in the left part of the Fig. 2.7. The right part of the figure shows the measured values. The abundance of nuclides with a lower mass-to-charge ratio were discussed already in the previous figure (the left side of the spectra). The consequences are reflected in the less exotic nuclides reached in the measurement, but not in the simulation.

2.3.2 Experiment with ^{238}U primary beam

TOFSIM simulation was also used to prepare the experiment with uranium fission fragments. The fragments were produced in a 1 g.cm^{-2} thick beryllium target from an uranium primary beam with an intensity of 1.7×10^9 particles/spill on average. 11203 shots were taken in the setting with $B\rho = 8.332$ Tm and an energy of the primary beam of 410 MeV/u. The cross-section in the simulation is

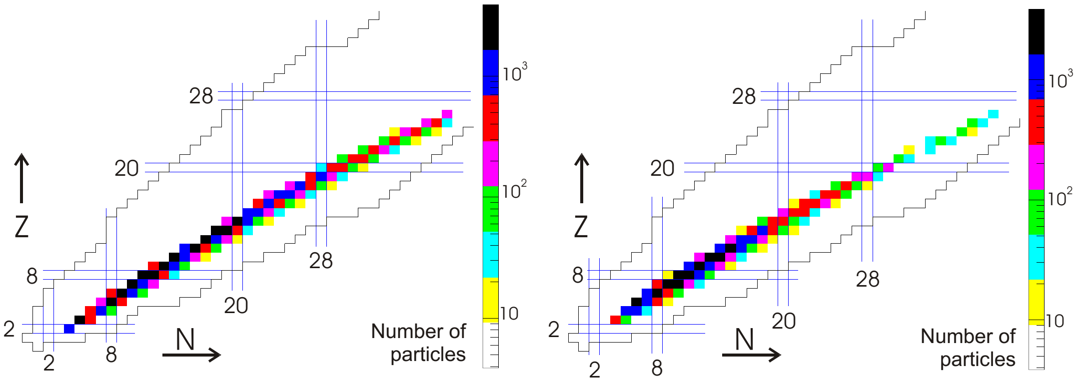

Figure 2.7: Charts with a comparison of the simulated (left) and measured (right) yields for the experiment with ^{70}Zn primary beam.

calculated using the ABRABLA code [Kel02, GS91]. The charge state of the fragment is calculated using the GLOBAL program [SSM$^+$98]. The phase-space after the fission processes was determined using the model of Wilkins et al. [WSC76]. The chart of nuclides with yields predicted by the TOFSIM is shown the Fig. 2.8.

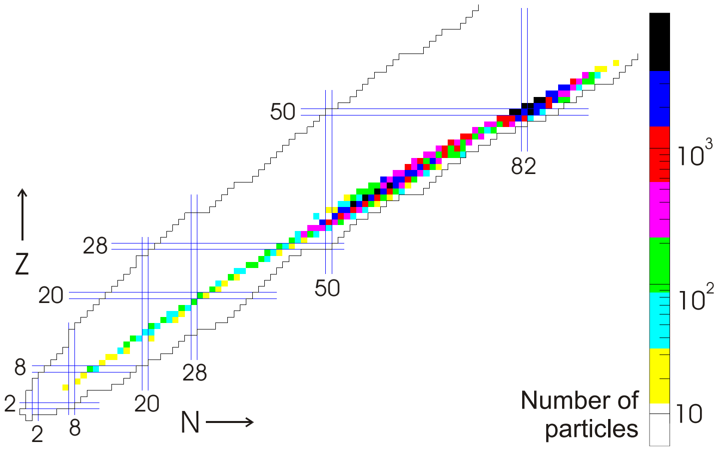

Figure 2.8: The chart with yields obtained in the experiment with ^{238}U primary beam according to the TOFSIM simulation.

In summary, as it was shown, the TOFSIM program is very useful for the preparation of complex experiments with FRS and ESR in the isochronous mode. It can very well describe positions of peaks in the TOF-spectrum and simplifies the identification during the data analysis. Also the reliable predictions of the yields can be decisive for planning of experiments.

Chapter 3

Experiments

The principle of the Isochronous Mass Spectrometry was already described in Chapter 1. To measure masses of neutron-rich nuclides, the ^{70}Zn projectile fragments and the ^{238}U fission fragments were produced and separated by the FRS and injected into ESR. The storage ring was operated in the isochronous mode.

3.1 Isochronous Mode of the ESR

Mass measurements of exotic nuclides are precision experiments. The most serious difficulties are short half-lives and low production rates.

The isochronous mass measurement in the ESR was proposed to overcome these problems [WSB86, WBB$^+$97]. For this the ESR is operated in isochronous mode [DVE$^+$96, HBD$^+$98] and the revolution time is measured by the TOF detector.

The time for a measurement time can be less than 100 μs, which would allow typically about 200 turns for the stored nuclei. The method is sensitive to a single particle in the ring.

3.1.1 Mathematical Description of the ESR Optics

The properties of the ESR can be expressed theoretically [Hau99].

A particle with a velocity v revolves in the ESR of a circumference C with a frequency f

$$f = \frac{v}{C}. \tag{3.1}$$

Differentiation yields

$$\frac{df}{f} = \frac{dv}{v} - \frac{dC}{C}. \tag{3.2}$$

In the description of synchrotrons and storage rings [BJ93] usually the momentum compaction α_p is defined as

$$\alpha_p = \frac{1}{C}\oint \frac{D(s)}{\rho} ds, \tag{3.3}$$

which describes a particle revolving not on the central orbit. The dispersion D at the position s of the ring describes a shift from a central orbit x of the particle with momentum $B\rho + dB\rho$

$$D(s) = \frac{x(s)}{d(B\rho)/(B\rho)}, \tag{3.4}$$

where $B\rho$ is a central orbit rigidity. A particle with this rigidity will move on the trajectory ds, see Fig. 3.1. It is clear from the figure, that

$$\frac{\rho}{\rho + x} = \frac{ds}{ds + dL} \qquad \text{and} \qquad \frac{\rho}{x} = \frac{ds}{dL} \tag{3.5}$$

where $ds + dL$ is a trajectory of the particle with a magnetic rigidity $B\rho + dB\rho$.

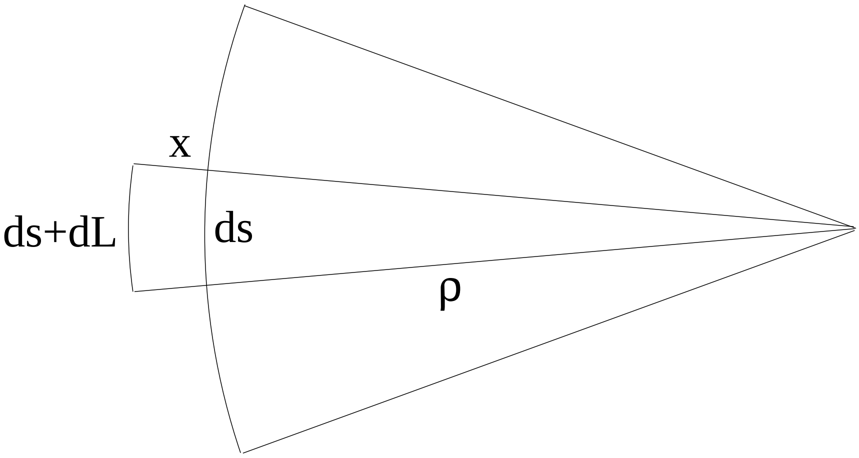

Figure 3.1: Comparison of a central orbit trajectory with a shifted trajectory. The ion with the magnetic rigidity $B\rho$ moves on the trajectory ds, while the ion with $B\rho + dB\rho$ moves on the trajectory $ds + dL$.

If we combine Eq. 3.3-3.5, we get

$$\alpha_p = \frac{1}{C}\oint \frac{x(s)}{d(B\rho)/(B\rho)}\frac{ds}{\rho} = \frac{1}{C}\oint \frac{dL}{d(B\rho)/(B\rho)} = \frac{dC}{C}\frac{B\rho}{d(B\rho)}, \tag{3.6}$$

where $dC = \oint dL$ is the difference in the full revolution trajectory. Now we can further develop Eq. 3.2,

$$\frac{df}{f} = \frac{dv}{v} - \alpha_p \frac{d(B\rho)}{(B\rho)}. \tag{3.7}$$

The magnetic rigidity for the relativistic charged particle can be expressed as

$$B\rho = \frac{p}{q} = \frac{\gamma m v}{q} = \frac{m}{q}\gamma\beta c, \tag{3.8}$$

where relativity variables are defined as

$$\beta = \frac{v}{c}, \quad \gamma = \frac{1}{\sqrt{1-\beta^2}}, \quad \beta\gamma = \frac{\beta}{\sqrt{1-\beta^2}}. \tag{3.9}$$

The differential is

$$d(B\rho) = \frac{\partial(B\rho)}{\partial\left(\frac{m}{q}\right)} d\left(\frac{m}{q}\right) + \frac{\partial(B\rho)}{\partial(\gamma\beta)} d(\gamma\beta) = \gamma\beta c \cdot d\left(\frac{m}{q}\right) + \frac{m}{q}\, c \cdot d(\gamma\beta) \tag{3.10}$$

and the relative differential

$$\frac{d(B\rho)}{B\rho} = \frac{d\left(\frac{m}{q}\right)}{\frac{m}{q}} + \frac{d(\gamma\beta)}{\gamma\beta}. \tag{3.11}$$

The differential of $\beta\gamma$ is

$$\begin{aligned} d(\beta\gamma) &= \frac{\partial\left(\frac{\beta}{\sqrt{1-\beta^2}}\right)}{\partial\beta} d\beta = \left(\frac{1}{\sqrt{1-\beta^2}} + \frac{\beta^2}{(1-\beta^2)^{3/2}}\right) d\beta \;= \\ &= d(\beta\gamma) = (\gamma + \beta^2\gamma^3) = \gamma\left(1 + (\beta\gamma)^2\right) d\beta \end{aligned} \tag{3.12}$$

and the relative expression is

$$\frac{d(\beta\gamma)}{(\beta\gamma)} = \left(1 + (\beta\gamma)^2\right)\frac{d\beta}{\beta} = \gamma^2\frac{d\beta}{\beta}, \tag{3.13}$$

where

$$1 + (\beta\gamma)^2 = 1 + \frac{\beta^2}{1-\beta^2} = \frac{1-\beta^2+\beta^2}{1-\beta^2} = \frac{1}{1-\beta^2} = \gamma^2 \tag{3.14}$$

was used. Using Eqs. 3.11 and 3.13, Eq. 3.7 can be written as

$$\frac{df}{f} = \frac{dv}{v} - \alpha_p\left(\frac{d\left(\frac{m}{q}\right)}{\frac{m}{q}} + \gamma^2\frac{dv}{v}\right) \tag{3.15}$$

or

$$\frac{df}{f} = -\alpha_p\frac{d\left(\frac{m}{q}\right)}{\frac{m}{q}} + (1-\alpha_p\gamma^2)\frac{dv}{v}. \tag{3.16}$$

It is usually written in the form

$$\frac{df}{f} = -\alpha_p \frac{d\left(\frac{m}{q}\right)}{\frac{m}{q}} + \left(1 - \frac{\gamma^2}{\gamma_t^2}\right)\frac{dv}{v} \tag{3.17}$$

where

$$\gamma_t = \frac{1}{\sqrt{\alpha_p}}. \tag{3.18}$$

is the transition point.

The goal of the isochronous mode is to make $\gamma = \gamma_t$. If this condition is fulfilled the second part of the equation goes to zero and the frequency does not depend on the velocity anymore. Then the frequency is a function of the mass-to-charge ratio only.

If $\gamma = \gamma_t$, the particles with higher velocities revolve on longer trajectories, so particles with a same mass-to-charge ratio revolve with a same frequency, independent of their velocity. The application of a storage ring in the isochronous mode for mass measurements was proposed by [Wol87].

The isochronous mode of the ESR with a γ_t in the range of 1.37–1.41 is obtained by adjusting the ion optical setting quite different from the standard storage mode [DVE+96, HBE+98, Hau99, HAB+00].

3.1.2 Measurements of the Isochronicity Curve

Before any measurement using an isochronous mode takes place in ESR, the isochronicity of the setting has to be verified. Therefore a set of measurements is done, where revolution frequencies of a cooled primary beam for various cooling energies are determined.

Frequencies are measured by Schottky noise spectroscopy [BBH+74], which is used for non-destructive beam diagnosis in circular accelerators and storage rings. Ions circulating in the ring induce at every turn a mirror charge on two electrostatic pick-up electrodes [Sch91]. Fast Fourier transformation is applied to the raw spectra which yields noise density spectra. Although a single signal is not visible in the time domain because of the signal noise, it is repeated periodically and the corresponding frequency appears in the frequency domain spectra.

The magnetic rigidity of the ions is fixed by an electron cooler [Fra87, ABE+89]. Electrons of the same velocity act on the ions and contract the phase-space volume of a stored beam. The velocity distribution can be reduced down to $\Delta v/v \approx 5 \times 10^{-7}$ by electron cooling [Ste97]. The maximum electron energy possible in the ESR is 240 keV.

The frequency dependence on the magnetic rigidity, resp. the cooler voltage is called an isochronicity curve. An example of a measured isochronicity curve obtained using a $^{238}\mathrm{U}^{90+}$ primary beam is shown in Fig. 3.2. It is obvious that

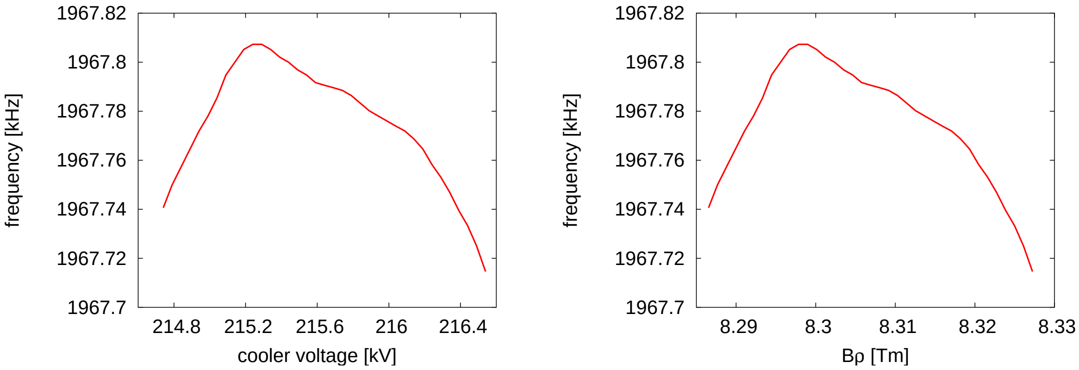

Figure 3.2: The measured isochronicity curve, cooler voltage vs. frequency (left panel) and Bρ vs. frequency (right panel) representations for the setting of ^{135}Sn as a reference fragment. The primary ^{238}U^{90+} was injected into ESR and cooled with the various cooling energy.

there is a direct relation between the cooler voltage and Bρ, as the former determines the energy and consequently also the Bρ of ions. The isochronicity curve is therefore identical in both representations. The figure with a Bρ vs. frequency shows also the ESR acceptance.

The curve is not isochronous for ^{238}U^{90+}, that was used for measurement and would look the same for every ion with the same mass-to-charge ratio, but it holds for ^{135}Sn, that is more obvious after transformation.

3.1.3 Transformation of the Isochronicity Curve

To measure an isochronicity curve we use a beam of one ion species only. This is more difficult and complex with a secondary beam, so the isochronicity curve is measured usually with a primary beam. In general it is different from the isochronicity curve of a desired nuclide, as the nuclides differ in their mass-to-charge ratios.

To transform an isochronicity curve to the nuclide of an interest, the frequency can be calculated from

$$f_{tran} = f_{meas} \frac{\sqrt{\left(\frac{(m/q)_{exp}}{B\rho}\right)^2 + \frac{1}{c^2}}}{\sqrt{\left(\frac{(m/q)_{tran}}{B\rho}\right)^2 + \frac{1}{c^2}}} \tag{3.19}$$

using Eq. 2.3 and 2.4, as it was explained and discussed in Sec. 2.1.1. The curve was measured for the mass-to-charge ratio $(m/q)_{exp}$ and is transformed for the mass-to-charge ratio $(m/q)_{tran}$. An example of an isochronicity curve transformed from the measured isochronicity curved shown in Fig. 3.2 for $m/q = 2.69$ using Eq. 3.19 is shown in Fig. 3.3. It is shown as a function of the magnetic rigidity and circumference. The latter can be used as a check of the isochronicity curve measurement, as the ESR circumference is known.

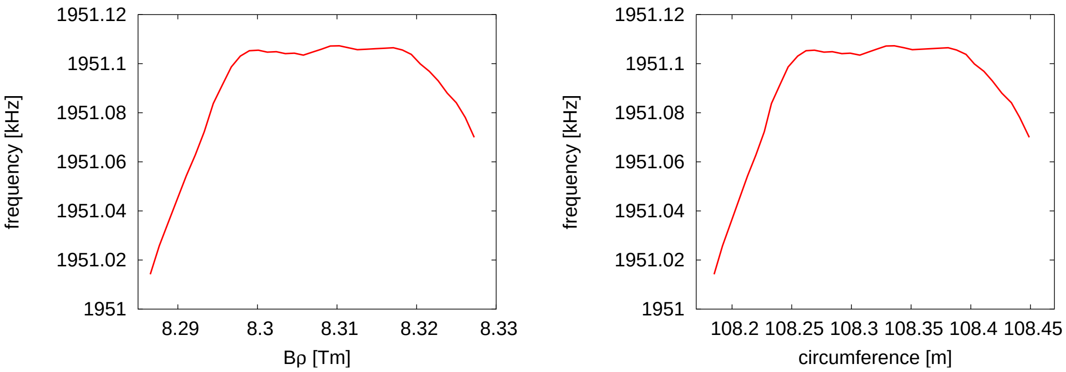

Figure 3.3: The transformed isochronicity curve in Bρ vs. frequency (left) and circumference vs. frequency (right) representations for $m/q = 2.69$. The curve was transformed from the measured curve from Fig. 3.2. The curve is isochronous for the magnetic rigidity between 8.3 and 8.318 Tm, where scrapers were installed to get rid of non-isochronous parts.

The measured isochronicity curve fulfills the requirement for the magnetic rigidity between 8.300 and 8.318 Tm, i.e. the frequency is constant and $f/\Delta f$ amounts to about 10^6. To have the isochronous behavior of particles with $m/q = 2.69$, the scrapers inside the ESR were used, see Tab. 3.1.

This means that ions with a mass-to-charge ratio of 2.69 will revolve with a frequency of about 1951.1 kHz independent from the velocity. It means the revolution frequency is not effected by the inevitable energy losses in the detector foil.

3.2 Energy Loss and Charge Exchange in the ESR

An ion of any species can be injected into the ESR with a magnetic rigidity distribution, which can vary for different ions. The injection acceptance of the ESR in the isochronous mode was discussed already in Sec. 2.2 and has the width of about 0.2%.

An ion is circulating in the ring until is lost. There are two main processes that cause particle losses during an isochronous mass measurement: a charge exchange and energy losses.

In the first process an ion can catch or lose an electron (if it is not bare) in the detector foil. This changes its charge and consequently also its Bρ. The change is typically so high, that it falls out of the ESR acceptance and the particle is lost.

On the other hand, energy losses appear in the every turn, when a particle is passing the detector foil, so it causes a very slow decrease of Bρ. If the lower limit of the Bρ acceptance is reached the particle hits a part of the device and also gets lost.

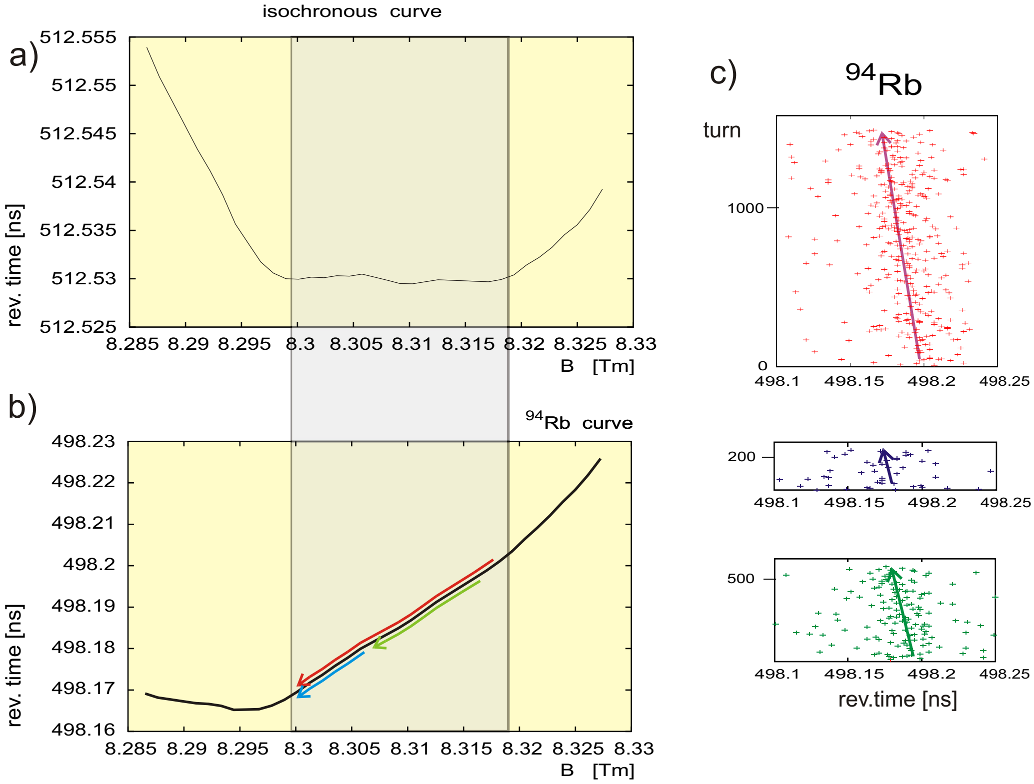

Figure 3.4: Revolution times for a ^{94}Rb ion stored in the ESR. **a)** The isochronicity curve from Fig. 3.3. **b)** The isochronicity curve is transformed for ^{94}Rb^{37+}. Due to the detector foil the ion losses energy and the revolution frequency is changed. The characteristics of revolution time of the three ^{94}Rb ions after multiply passing of the detector foil are shown in the part **c)**. The red one enters the ESR with a Bρ, that is close to the upper limit of the Bρ acceptance and survives approximately 1450 turns, after energy losses in the foil it reaches the lower Bρ limit. At this place it is outside the ESR acceptance, as well as the blue particle. The ^{94}Rb indicated in green color is lost probably due to a charge exchange. The characteristics of the ions on the isochronicity curve are also indicated in the part b).

Some typical examples observed in the experiment are shown in Fig. 3.4. In the upper left part the isochronicity curve from Fig. 3.3 is shown in the magnetic rigidity vs. revolution time representation. The grey area indicates the isochronous part of the curve. This part is confined by scrapers. In the left lower part the isochronicity curve is transformed for ^{94}Rb^{37+}. Here, the curve is not isochronous and its revolution time allows us to determine the position on the isochronicity curve and therefore Bρ. Three examples of ^{94}Rb ions were chosen to be compared, their revolution time behaviors after multiply passing the detector foil are shown in the right part of the figure.

The red one entered the ESR with a Bρ, that is close to the upper limit and survives approximately 1450 turns, when after energy losses in the foil it reaches the lower Bρ limit. After this the ion is lost out of the ESR acceptance. We can check, whether the energy loss would correspond to the calculated value. The ^{94}Rb^{37+} with the magnetic rigidity of 8.319 Tm has the energy of 421.78 MeV/u. The energy loss in the foil 20 μg/cm^2 C on both sides covered with 10 μg/cm^2 CsI calculated by the ATIMA [SG98] is 1.41×10^{-3} MeV/u. After 1450 turns the ions has the energy of 419.74 MeV/u, which corresponds to the magnetic rigidity of 8.295 Tm. According to the calculation the change in the magnetic rigidity is 0.024 Tm, according to the observation it is 0.019 Tm. The position of the scrapers with respect to the optical axis is only known approximately, also the width of the foil, so we can consider the results to be in the agreement.

The same situation as in the previous case happens for the blue particle, but it had its initial energy lower and started in the vicinity of the lower Bρ limit, which was reached after less than 300 turns.

The green particle had its initial Bρ close to the Bρ of the red one, but is lost already after about 600 revolutions, probably due to a charge exchange.

The measurements have shown, that an ion can survive only a maximum number of turns in the ESR, after which the energy loss corresponds to the width of the ring acceptance. In Fig. 3.5 it is illustrated, that a maximum number of turns depends on the proton number.

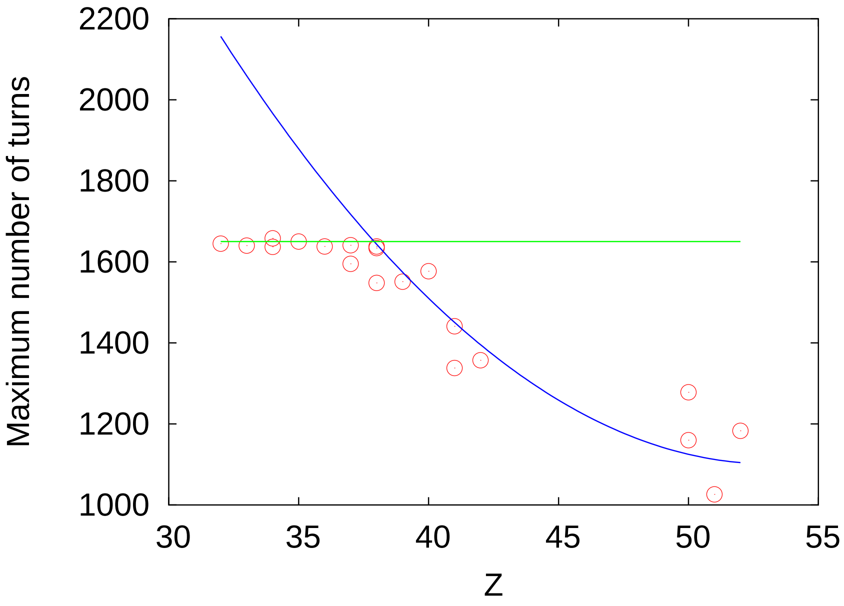

Figure 3.5: The maximum number of turns achieved for one species depending on the proton number. The blue line represent a time limit of the data acquisition system, when the scope stops the signals processing. The green line is drawn to guide an eye. It shows how many turns are needed for an ion to lose an energy to go through full ring acceptance. This is the number of turns after which the energy loss corresponds to the change of the magnetic rigidity that is equal to the acceptance of the ring. On average an ion revolved 260 turns in the ring.

Ions in the element range of $31 < Z < 53$ were investigated to know the highest number of turns for one species. The observed maximum drops with increasing the proton number, as seen in the figure. The reason for this dependence is that the energy loss of an ion increases quadratically with an increasing proton number [Bet30].

Now we can well describe particle losses in the ESR. Some examples are shown in Fig. 3.6. The particle losses due to the ring acceptance are shown with a green color, values are taken from Fig. 3.6 under the assumption that the Bρ distribution is uniform. The process does not depend on the number of particles.

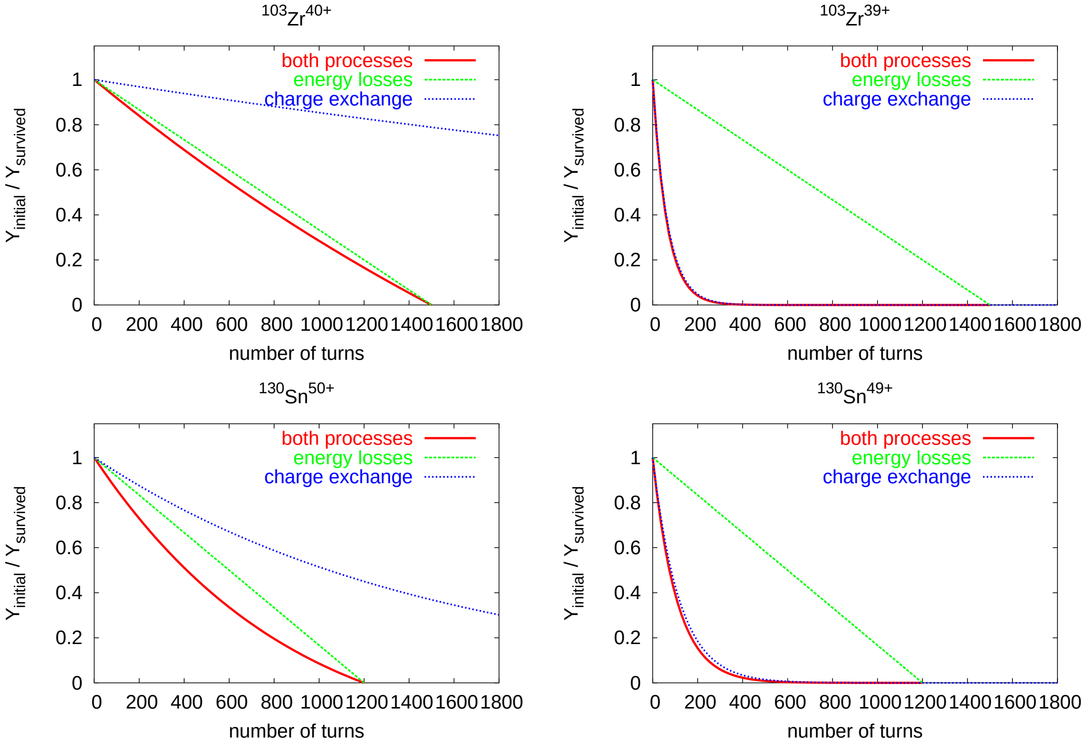

Figure 3.6: Particle abundances Y of species in ESR reduced by the energy losses and the charge exchange. ^{103}Zr and ^{130}Sn in the bare and H-like states are presented. In the case of H-like ions the charge exchange is dominating. The situation is contrary for bare ions, where energy losses in the detector foil cause most of particle losses. This trend is less pronounced for ions with higher proton number. The charge exchange was calculated using the GLOBAL program [SSM$^+$98] for energies corresponding to the magnetic rigidity Bρ=8.31Tm. The probability of charge exchange in the 20μg/cm carbon foil coated on both sides with 10μg/cm CsI for ^{103}Zr^{40+} is 1.58×10^{-4}, for ^{103}Zr^{39+} 1.52×10^{-2}, ^{130}Sn^{50+} 6.65×10^{-4} and for ^{130}Sn^{49+} it is 8.44×10^{-3}. The particle losses due to energy loss were taken from the considerations described in the Figs. 3.4 and 3.5.

The charge exchange is a random process and it depends on a number of particles. Therefore it has an exponential dependence as shown in the figure. The charge exchange probabilities were calculated using the GLOBAL program [SSM+98]. The probability of charge exchange in the 20μg/cm carbon foil coated on both sides with 10μg/cm CsI for $^{103}\mathrm{Zr}^{40+}$ is 1.58×10^{-4}, for $^{103}\mathrm{Zr}^{39+}$ 1.52×10^{-2}, $^{130}\mathrm{Sn}^{50+}$ 6.65×10^{-4} and for $^{130}\mathrm{Sn}^{49+}$ it is 8.44×10^{-3}.

Indeed both processes occur in parallel. In the case of H-like ions the charge exchange is dominating. The situation is contrary for bare ions, where the energy loss in the detector foil causes most of the particle losses. This trend is less pronounced for ions with larger proton number.

3.3 The Data Acquisition System

The data acquisition (see Fig. 3.7) for the isochronous mass spectroscopy is a challenging task. The time resolution of the detector should not be reduced by the timing properties of the following electronics. Furthermore it should be possible to observe ions over many revolutions in the ESR. The intrinsic time accuracy of the detector is about 50 ps and one revolution in the ESR has a duration of about 500 ns.

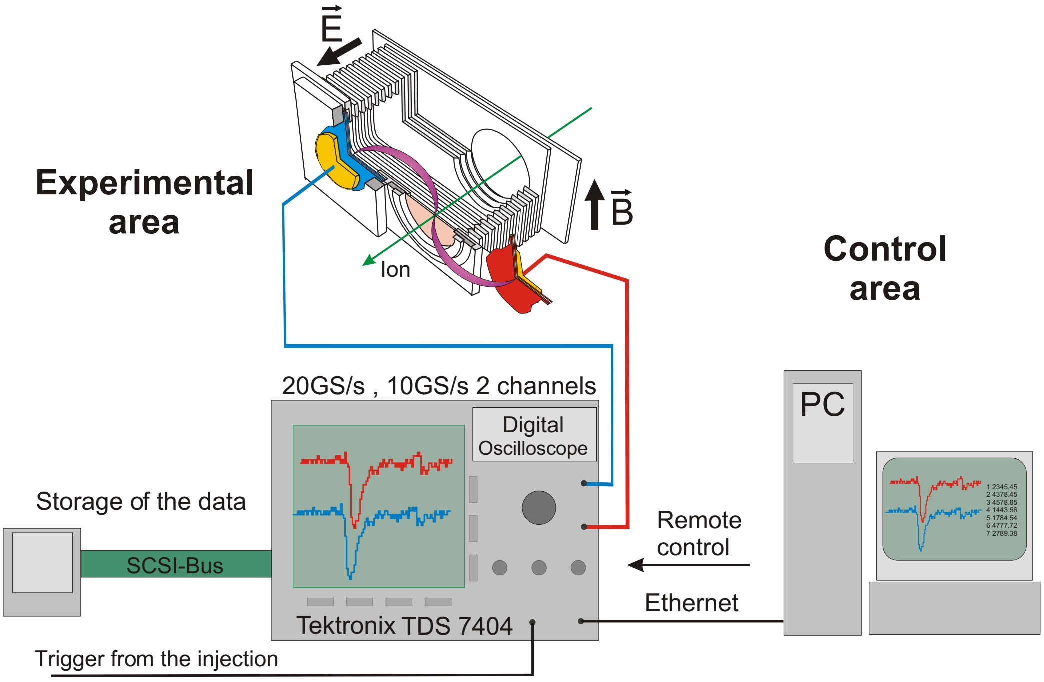

Figure 3.7: Systematic scheme of the data acquisition. Signals are produced in the microchannel plates and transfered to the scope, where they are digitized. The scope starts to load the signals after the trigger form the injection. The scope is controlled from the computer placed in the control area.

The detection of signals should be without a significant dead-time. The total duration of a signal is about 3 ns, so the next stored ion can be recorded after time for signal processing in the electronic modules.

Commercial time measurement systems have difficulties to fulfill all the conditions. Either they are very accurate but have long dead-time or short acquisition times or the system cannot carry out long term measurements with suitable accuracy.

In the preceding experiments [HSA+01, SGH+00, GAB+01, Sta02] a LeCroy LC584AM oscilloscope was used to sample and store signals from the detector for off-line analyses. The measurement time was up to 200μs and the sampling rate 4GS/s. The sampled data were read out from the scope to the computer via the GBIB interface, which limited the transfer rate to about 1 MB/s.

In the experiment presented in this work a Tektronix TS7404 scope was tested. It has an analog bandwidth of 4GHz and a sampling rate of 10GS/s for two channels. The large sampling memory of the oscilloscope allows measurement times of 1.6 ms on two channels or 3.2 ms with one channel. The new device has a built-in PC which makes it possible to write the recorded data directly to hard-disk. This decreases the time needed for storage considerably. During the experiment both oscilloscopes were used and the new Tektronix device was proven to be well suited for the task.

To preserve the signal quality (leading edge rise time $\approx$400ps) the oscilloscopes were placed directly in the ESR close to the detector, and they were remotely controlled from the main control room via Ethernet.

3.4 Injection into the Central Orbit of the ESR

In the experiment with the uranium primary beam the injection close to the central orbit was used [Bel04].

The beam injected into the ESR has to be transferred into the storage ring orbit using a septum magnet and a kicker magnet.

The kicker magnet is situated off the central orbit and therefore the injected beam has to circulate on the outer orbit. This is suitable for most of the experiments in the ESR, but not for the isochronous ion-optical mode. This mode is very sensitive to the setting of the magnetic fields. Therefore it would be of advantage if the ions are circulating close to the central orbit, where the quality of magnetic field is best.

For that reason the beam was not injected to the outer orbit, but close to the central orbit. A local orbit bump allowed a particle to pass through the kicker, that performed an angle correction. After this correction, the particle circulated on a central orbit. The beam envelope in the horizontal plane of the ESR is shown in Fig. 3.8. The local orbit bump was placed between path lengths of 70 m and 80 m.

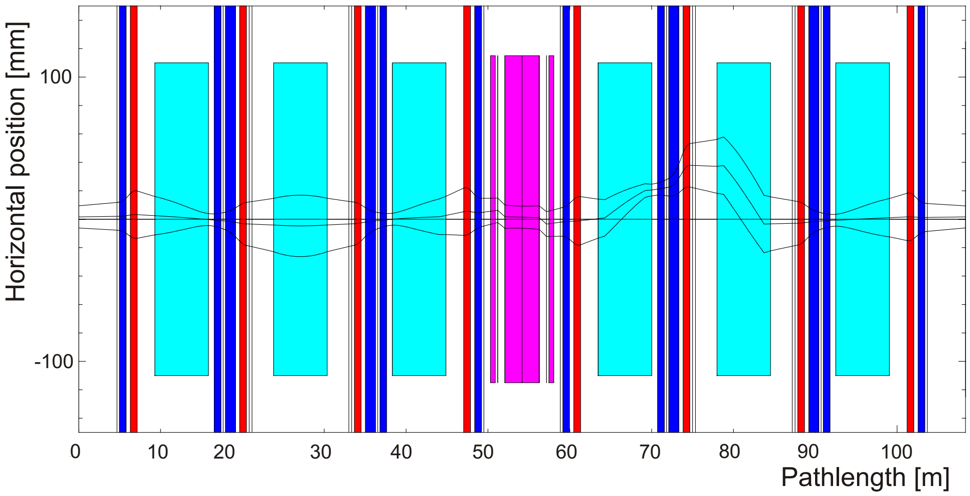

Figure 3.8: Size of the beam envelope in the horizontal plain of the ESR according to the MIRKO calculation. The local orbit bump allows a particle to pass through the kicker, which is placed between path lengths of 70 m and 80 m.

3.5 Experiment with the ^{70}Zn Fragments

The primary beam ^{70}Zn with an energy of 456.4 A·MeV and an intensity of 1×10^9 particles/spill produced projectile fragments in a 4g/cm^2 beryllium target, no degrader was used. The Bρ settings of 7.53 Tm for a cocktail beam centered for ^{57}Ti^{22+} was applied to the FRS-ESR facility.

3.6 Experiment with the ^{238}U Fission Fragments

Also no degrader was used in the experiment with ^{238}U fission fragments.

To cover a large area of isotopes from fission, several Bρ settings were applied. The list of the settings is given in Tab. 3.1.

reference fragment	^{130}Sn	^{133}Sn	^{135}Sn
primary beam energy	381MeV/u	415 MeV/u	410 MeV/u
Bρ after the target	7.5321Tm	8.209 Tm	8.332 Tm

Table 3.1: The overview of the settings applied in the experiment to cover all neutron-rich fission fragments. In all settings the 1 g/cm^2 Be target was used. In the setting with ^{135}Sn as a reference fragment, the scrapers were in the following positions: E01DS_HA = -65mm, E01DS_HI = 8mm, E02DS_HA = -65mm, E02DS_HI = 32mm.

In the ^{135}Sn setting the ESR scrapers E01DS and E02DS were used to eliminate an isochronous part of a isochronicity curve, as is explained in Sec. 3.1.

3.7 Phase-space of the fission fragments after the In-Flight Separation at FRS

Uranium fission fragments produced and separated at the FRS were for the first time injected into the ESR. The energy of a fission fragment is defined by fission kinematics, i.e. the recoil energy and the angle between fragment and primary beam. If they are parallel the energy reaches a maximum, if they are antiparallel it has a minimum. In these two cases the final direction of the fragment is identical with the primary beam direction. The direction of the recoil products is spatially isotropic. This peculiarity of the fission kinematics is used in order to separate efficiently the most neutron-rich isotopes produced by the fission process and to suppress undesired isotopes intensively produced by the projectile fragmentation. The kinetic energy as a function of the horizontal angle for ^{135}Sn fragments produced by fragmentation and fission of 415 MeV/u ^{238}U projectile is calculated at the entrance of the FRS [IGM+97] , see Fig. 3.9. The difference between most forward and backward emitted fragments is more than 100 MeV/u. Optimizing the FRS optics for the fragments emitted in the forward directions we can suppress the transmission of the projectile fragments. The window in Fig. 3.9 shows the part of the phase-space selected by the FRS, which allows to transmit only fission fragments.

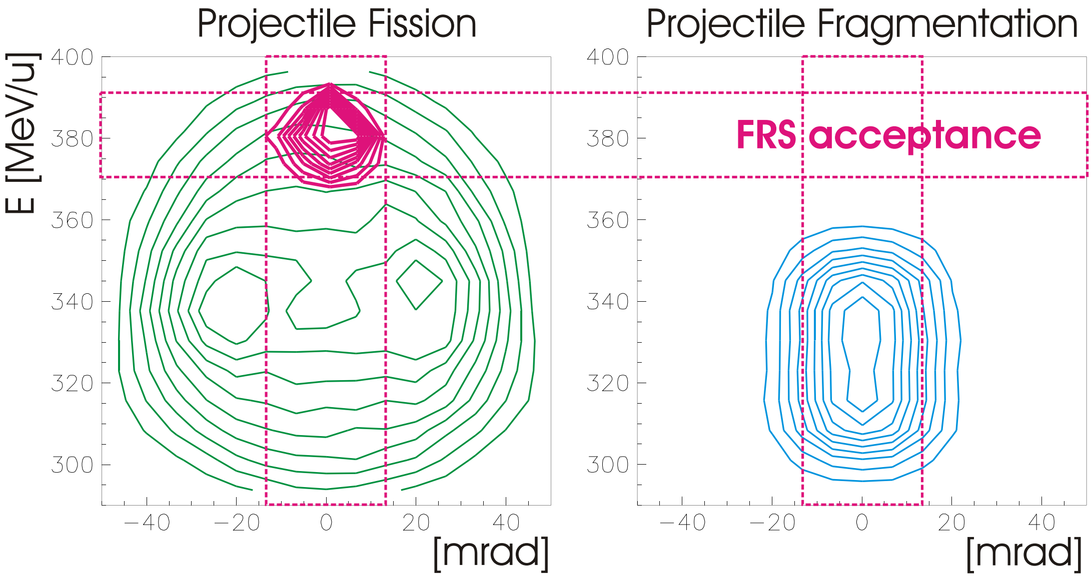

Figure 3.9: The kinetic energy of ^{135}Sn fission and projectile fragments of 415 MeV/u ^{238}U as a function of the horizontal angle when leaving the beryllium production target at the entrance of the FRS as a result of the MOCADI calculation [IGM+97]. The red window shows the part of the phase-space restricted by FRS, which allows fission fragments only to be transmitted.

Only a narrow magnetic rigidity window is separated by the FRS and also the

ESR injection. Magnetic rigidity distributions of several species before an injection into the ESR calculated by the MOCADI [IGM+97] are shown in Fig. 3.10.

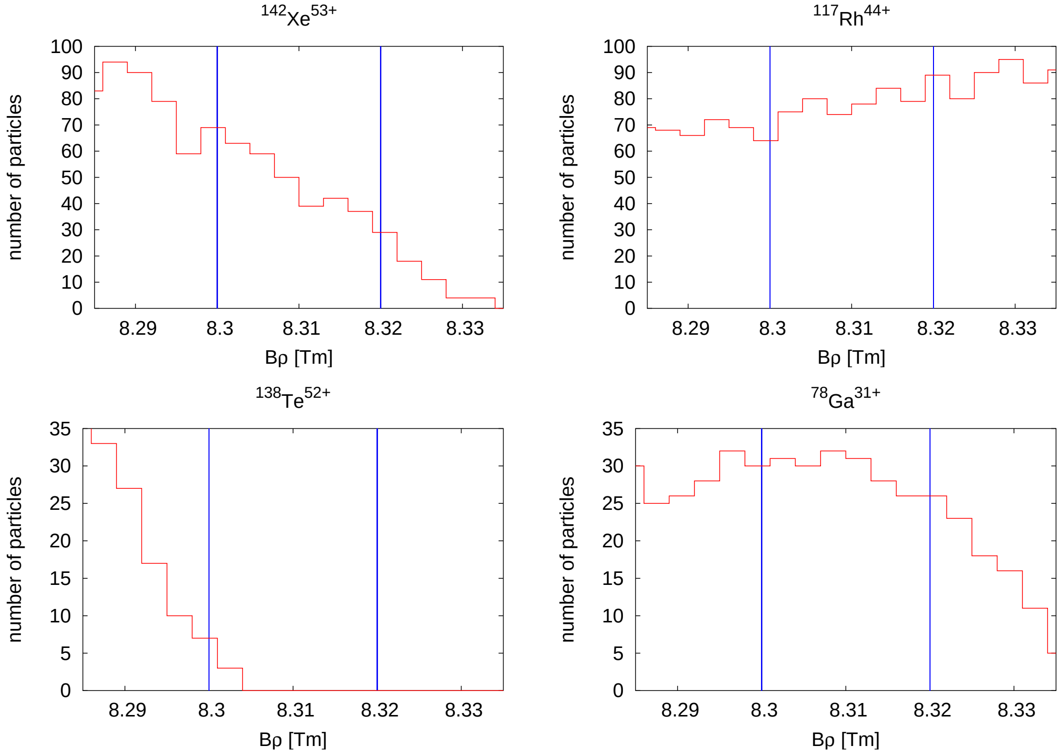

Figure 3.10: Calculated magnetic rigidity distribution of several isotopes before the injection into the ESR [IGM+97] for the mean Bρ setting of ^{135}Sn as a reference fragment. An injection acceptance window into ESR marked by blue lines separates different parts of the magnetic rigidity distributions for various ions.

It is demonstrated, that the magnetic rigidity distribution differs for the different species. It means, that for some ions lower or higher magnetic rigidity can be more probable to be stored in the ESR. This has an effect on the mean magnetic rigidity, that can differ for various species and can lead to a mean revolution time shift, as will be discussed later.

Chapter 4

Data Analysis

During the experiment we have acquired several terabytes of data. This amount of data reflects the comprehensive work of this PhD thesis.

4.1 Signal Processing

The data are received by the scope and digitized. In the case of the LeCroy scope a sampling frequency of 4 G samples/s and recording time of 200μs were used and with the Tektronix scope the sampling frequency was increased to 10 G samples/s and the recording time to 1ms.

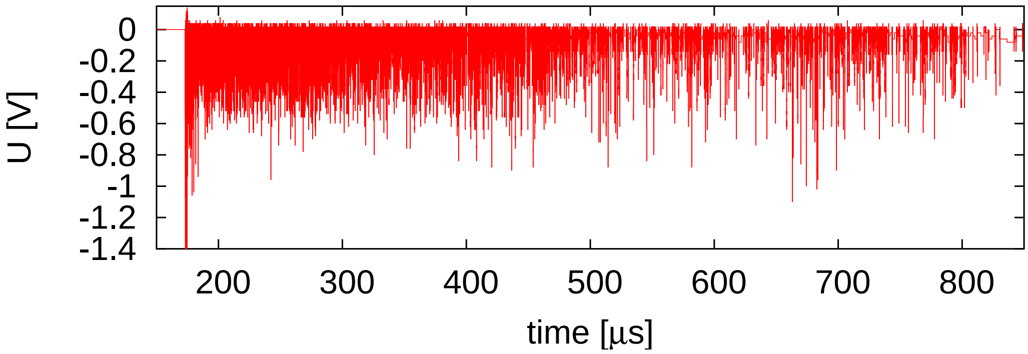

Figure 4.1: Signals from the detector after one injection into the ESR. One revolution in the ESR has a duration of about 500 ns. Therefore 800 μs correspond to about 1600 revolutions.

Signals from the detector after one injection into the ESR are shown in Fig. 4.1, One revolution in the ESR has a duration of about 500 ns, 800 μs therefore correspond approximately to 1600 revolutions in the ring.

Typical digitized signals from the detector are shown in Fig. 4.2.

4.1.1 Time Determination by Constant Fraction Triggering

Precision time measurements require a very accurate determination of the timing from the signal. The uncertainty of the time determination is limited by fluctuations, which are caused by two principle effects: walk and jitter [Leo87].

Timing fluctuations can be caused by noise and statistical fluctuations in the detector signal. This effect is usually referred to as time jitter.

Variations in the amplitude and/or the rise time of the incoming signals can be a source of inaccuracies called "walk effect". This occurs if for example a threshold is used as a trigger for timing.

In our case the charge collected on the anode of micro-channel plates varies drastically, as the time between signals is much smaller than the recovery time of a single channel in the detector, so both the amplitude and the rise time change from signal to signal, see Fig. 4.2.

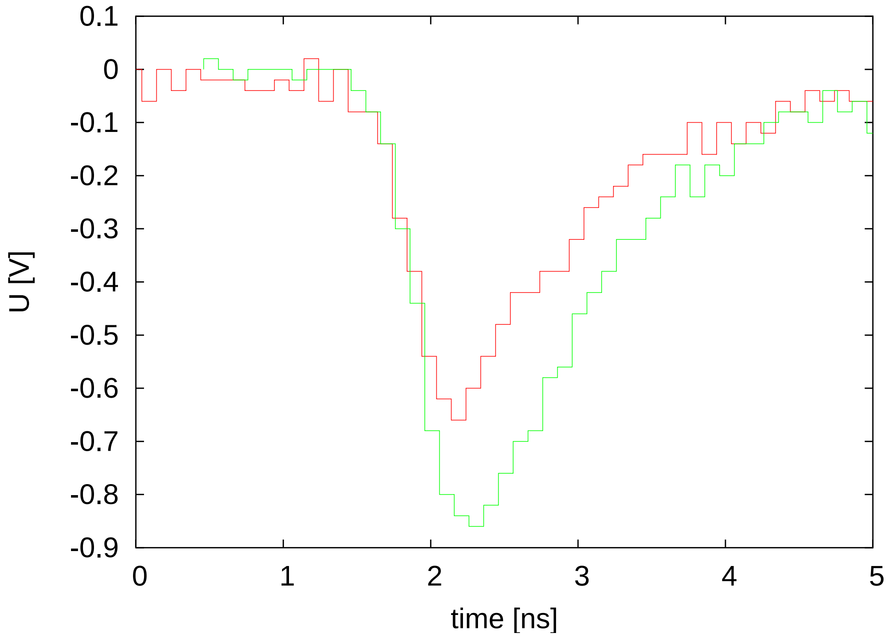

Figure 4.2: Comparison of two signals from one particle with a different time of the first edge and a different amplitude. The green signal needs longer time to reach its maximum than the red one. The effect, called walk, can be minimized by the constant fraction triggering technique.

To minimize walk, various different triggering or time-pickoff methods have been developed [Leo87]. Probably the most efficient and versatile method is the constant fraction triggering technique. The principle of the method is shown in Fig. 4.3.

First the baseline has to be determined. Amplitudes of all signals are histogrammed to get the noise distribution. This is expected to have a Gaussian

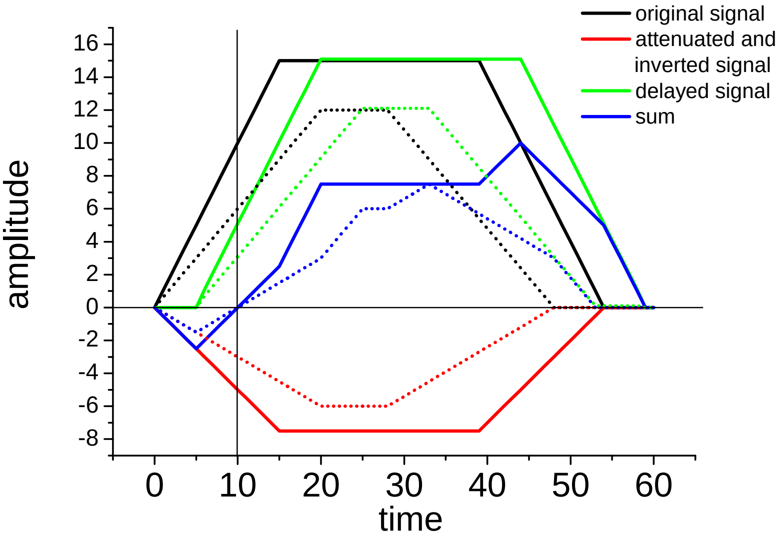

Figure 4.3: Comparison of the Constant Fraction Triggering for two signals (solid and dashed line) with the different amplitude and the different time of the rising edge. Timing is defined by a zero-crossing at the same time for the both signals and is equal for both signals independently from the amplitude and the time of the rising edge.

shape around the baseline. The baseline is the center of the Gaussian and is subtracted from the signals.

To receive a time stamp, first the signal (the black one in Fig. 4.3) is delayed (green signal) and in parallel attenuated and inverted (red signal). These two signals are summed (blue signal) and the zero crossing determines the time stamp. One can see that both signals (solid and dashed line) have the same zero-crossing, although they have different amplitudes and a rise times.

Since the digitized signal consists of discrete points rather than continuous data, a special treatment for the constant fraction algorithm is used. The zero crossing is determined from the two amplitudes neighboring the zero crossing - so the first amplitude, U_a, is supposed to be higher than the baseline and the second amplitude, U_b, lower. The time stamp is then determined from the equation

$$T = t_a - \frac{U_a(t_a - t_b)}{U_a - U_b}, \tag{4.1}$$

where U_a and U_b are the amplitudes of the summed signals and t_a and t_b are the corresponding times.

The uncertainty of the signal voltages are assumed to be equal to the standard deviation $\sigma(U_0)$ of the distribution obtained for the baseline determination. The uncertainty of the summed signal is then the superposition of a voltage of the original signal and the signal attenuated by fraction factor f

$$\Delta U = \sigma(U_0)\sqrt{1+f^2}. \tag{4.2}$$

We assume the time values to be free of any uncertainty. The uncertainty of the timing is then

$$\Delta T = \sqrt{\left(\frac{\partial T}{\partial U_a}\right)^2 \Delta U_a^2 + \left(\frac{\partial T}{\partial U_b}\right)^2 \Delta U_b^2} \tag{4.3}$$

and where if Eq. 4.1 is applied we get

$$\Delta T = \sqrt{\frac{(t_b-t_a)^2}{(U_b-U_a)^4}U_b^2\Delta U_a^2 + \frac{(t_b-t_a)^2}{(U_b-U_a)^4}U_a^2\Delta U_b^2}. \tag{4.4}$$

If we assume $\Delta U_a = \Delta U_b = \Delta U$ from Eq. 4.2

$$\Delta T = \sqrt{(U_a^2+U_b^2)(1+f^2)}\,\frac{t_b-t_a}{(U_b-U_a)^2}\,\sigma(U_0). \tag{4.5}$$

An error distribution with the delay parameter 400 ps and the fraction parameter 0.5 for experimental data is shown in Fig. 4.4. The mean error of the timing is 40 ps, the the root-mean-square is 52 ps.

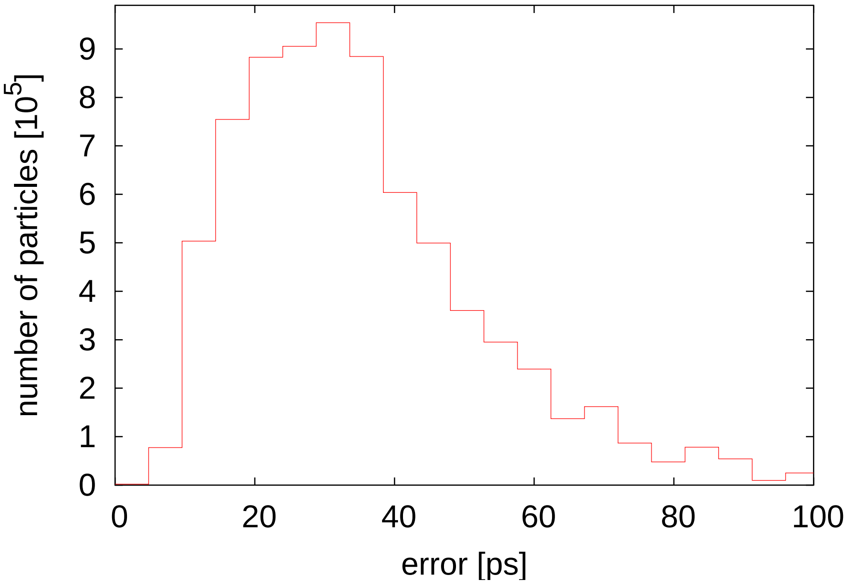

Figure 4.4: Distribution of the error from time determination from the signal using the constant fraction algorithm. The mean error of the timing is 40 ps, the the root-mean-square is 52 ps.

4.1.2 Parameters for the Constant Fraction Method

The constant fraction algorithm depends on two parameters, the fraction factor and the delay. Fig. 4.5 illustrates the effect of various delays.

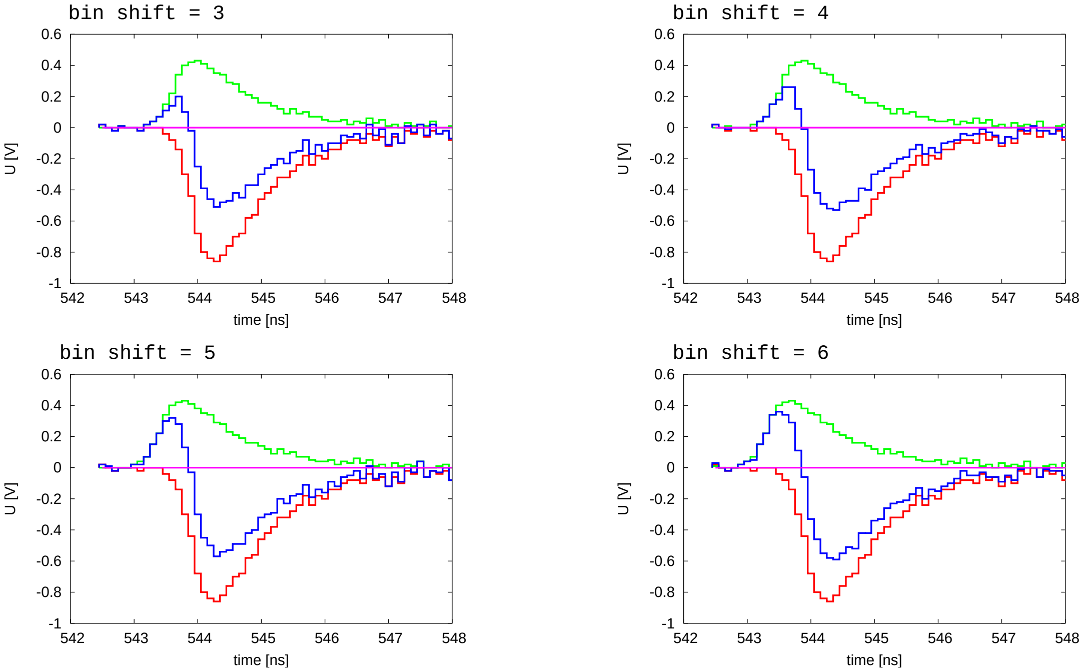

Figure 4.5: Comparison of a different delay in the constant fraction method, the delayed signal of the original size is red, the attenuated signal is green and their sum is blue.

Optimal choice of the parameters is essential for a good timing algorithm. To be independent from the time of the leading slope the zero-crossing has to be determined from the leading slope itself even for the shortest signals. Next we will show this on a simplified linear leading slope, where the signal a_{orig} is changing with time t

$$< 0, \tau_r > \qquad a_{orig} = \frac{A}{\tau_r}\, t, \tag{4.6}$$

where A is the amplitude and τ_r is the rise time. Then the attenuated signal with the fraction parameter f is

$$a_{atten} = -\frac{fA}{\tau_r}\, t, \tag{4.7}$$

the delayed signal with the delay time τ_d

$$a_{del} = \frac{A}{\tau_r}\,(t + \tau_d) \tag{4.8}$$

and the sum crosses the zero

$$0 = a_{atten} + a_{del} = \frac{A}{\tau_r}\,[t(1-f) + \tau_d], \tag{4.9}$$

when

$$t = \frac{\tau_d}{1-f} \tag{4.10}$$

If we want to use the leading slope only, then

$$t < \tau_r \tag{4.11}$$

which requires

$$\tau_d < (1-f)\,\tau_r. \tag{4.12}$$

If this is fulfilled, the walk effect should be eliminated.

A typical signal from the TOF detector digitized by the Tektronix scope has 800–900 ps leading slope corresponding to 8–9 bins. This limits the parameter choice.

As mentioned before, there is also a jitter effect, which causes timing fluctuations. To minimize the jitter, it is essential to choose parameters that place the zero crossing in the second half of the leading edge, so that the attenuated signal at the zero crossing is clearly above the noise. Examples of advantageous and disadvantageous choices of parameters are shown in Fig 4.6.

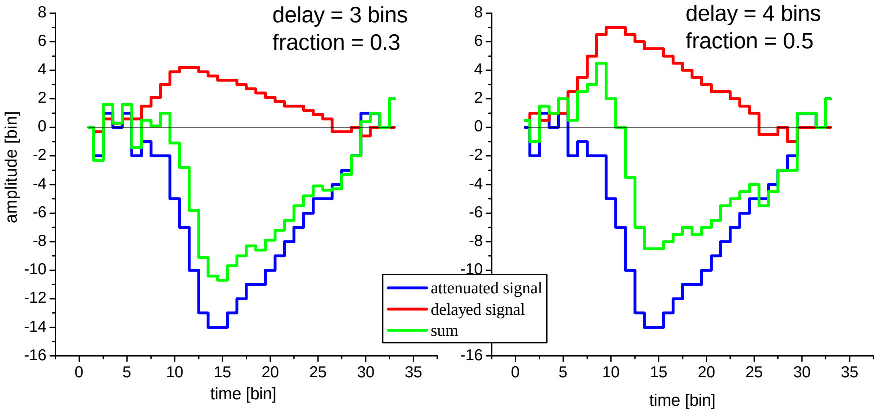

Figure 4.6: Advantageous (right) and disadvantageous (left) choice of parameters. In the left figure the jitter effect make the time determination ambiguous. The problem is solved by the advantageous choice of parameters, as is shown in the right figure.

The precision of the timing method can be determined by the measurement of fluctuations in the time difference between two coincident signals. As we have two independent signals from both sides of the detector we can use it to determine optimal parameters and get also the intrinsic resolution without any influence of non-isochronous conditions. The time determination for experimental data was performed with several sets of parameters. Stamps from both sides of the detector corresponding to the same signal were compared. A constant shift would be expected due to different cable lengths, but the width of the distribution of this shift determines the intrinsic resolution. The results are shown in Fig. 4.7.

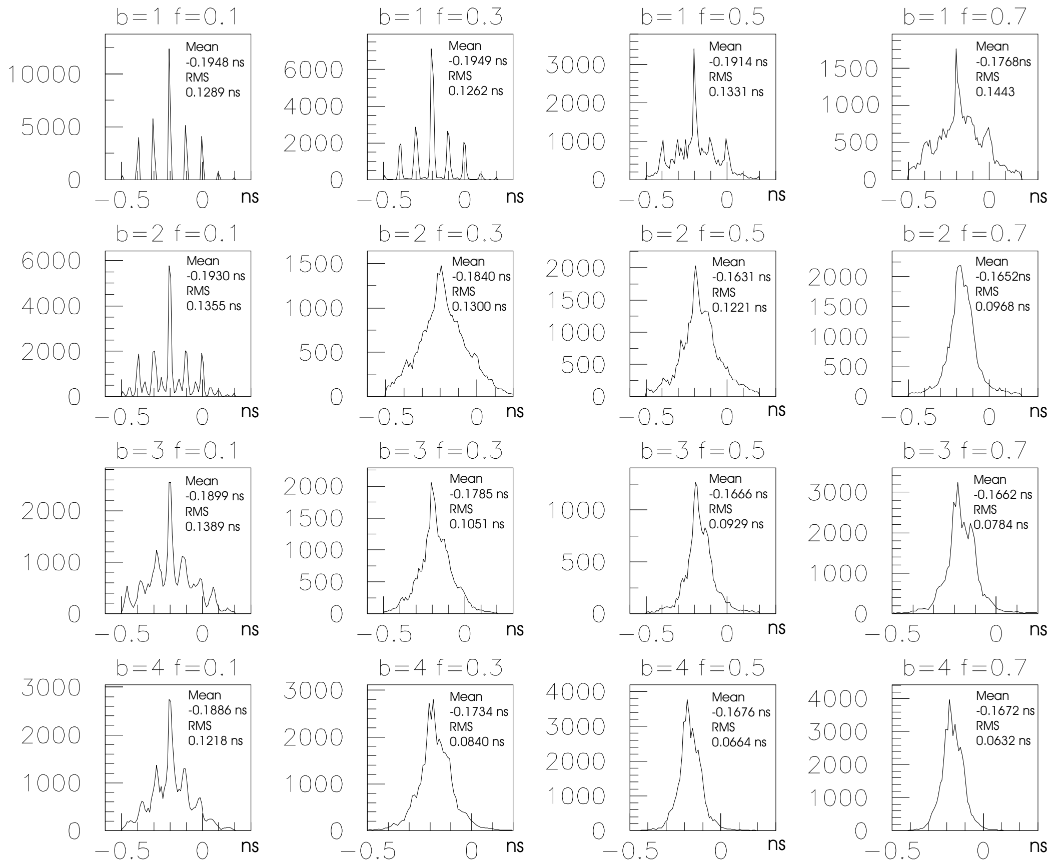

Figure 4.7: Distributions of the time difference between the stamps from both sides of the detector corresponding to same the signal. The width of the distribution of this shift determines the uncertainty of the time determination. The parameter b is the delay in bins, 1bin= 100 ps. The parameter f is the fraction. The set of parameters b=4, f=0.5 was chosen to be used in the analysis.

As we can see, the best results are for the sets of parameters b=4, f=0.5 and b=4, f=0.7. The latter choice does not fulfill the condition described in Eq.4.12, which allows to overcome the walk effect. For the same reason cases with b≥5 were not analyzed.

The distribution width of the chosen parameter set b=4, f=0.5 is σ_{RMS} =66 ps. It is a difference of two signals, so the uncertainty $\sigma(t_{dif})$ is

$$\sigma(t_{dif}) = \sqrt{\sigma(t)^2 + \sigma(t)^2} = \sqrt{2}\,\sigma(t), \tag{4.13}$$

where $\sigma(t)$ is the uncertainty of one signal and amounts to 47 ps. This is in good agreement with the mean value of the uncertainties mentioned before on the page 44.

4.2 Time-of-Flight Determination

In general there are several ions in the ring simultaneously. Therefore the spectra consist of the signals corresponding to various particles as it is shown in Fig. 4.8.

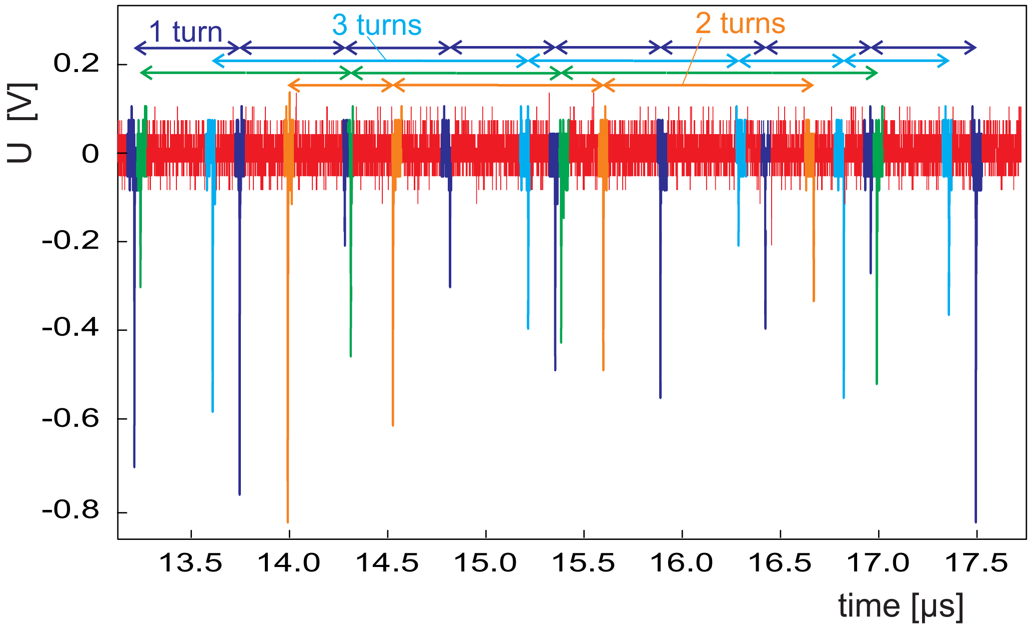

Figure 4.8: A demonstration of signals in a spectrum corresponding to various ions. The signals are identified by a tracing algorithm [Hau99, Sta02].

To determine the revolution times of the ions, an identification of the signals has to be done. An algorithm for tracing a particle in the spectra was developed by [Hau99].

It starts from a very last signal in a spectrum and searches for a corresponding one from preceding signals. The fact, that the revolution time is expected to be in a range of 400–600 ns is decisive. If a suitable signal is found, the revolution time is fixed. Then the remaining spectrum is scanned with the expected trace of the fixed revolution time. If no more signals are found, the fixed revolution time was not correct and another potential signal is used to fix a new revolution time. But if there were more signals found to fulfill the trace, it means they belong to a first identified particle and the procedure is repeated till all particles are traced.

In general the time-of-flight is determined as a difference between two signals at the beginning and at the end of the measuring time. However there are many revolutions in the storage ring with less than 50% detection efficiency. This means one signal would be a stop signal for one time measurement and a start signal for another one. Sometimes the time difference between two signals of one ion corresponds to one revolution, but usually several turns.

As it was already described in Sec. 3.2, a particle that is not perfectly isochronous changes its revolution time after energy losses in the detector foil. A relation between energy losses and revolution time changes is expressed by the isochronicity curve. As described in Sec. 3.1.3, the isochronicity curve depends strongly on a mass-to-charge ratio of the ion. Energy losses rise with the square of the ion proton number. So that if two ions enter the ESR with the same Bρ and mass-to-charge ratio, they are supposed to have the same revolution time. But if they differ in their proton number, they will differ also in their revolution time after several turns due to different energy losses. The mentioned problems are summarized in following:

1. The dependence of the revolution time changes with proton number.
2. The number of turns between two neighboring signals corresponding to one ion varies.
3. If we determined the revolution times of a single particle from two neighboring signal, they would be not statistically independent.

These circumstances require a special approach to overcome all the difficulties. A solution we used is to investigate a time dependence on a number of turns, see Fig. 4.9. The slope at a first particle occurrence is taken as a revolution time value determined for a single particle. This solves all introduced complications. The revolution time at a first ion occurrence is independent from its proton number, as it has no energy losses in the detector foil yet. The variation of number of turns and the statistical independence are constrained by the fitting through all points with 3^{rd} order polynomial function, see Fig. 4.10 and 4.11. Although we get rid of all information about single signals, we gain in getting a revolution time value with an uncertainty much lower than any signal time error and we will work with self-independent data.

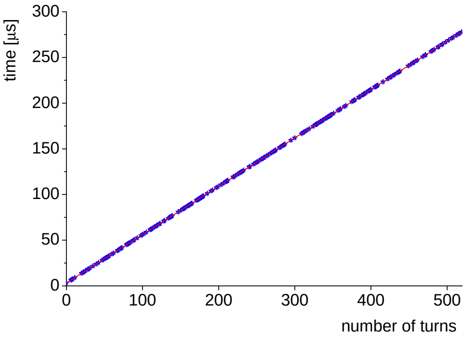

Figure 4.9: Time dependence of the turn number for a single particle. It is very close to a linear function.

In case of perfect isochronicity a relation between time and the number of turns would be a linear function. In reality the dependence differs slightly from linearity, see Fig. 4.10. The non-linearities are described by the isochronicity curve, which means that it is not possible to describe it with an analytical function. The nonlinearities can be solved with a higher order polynomial function.

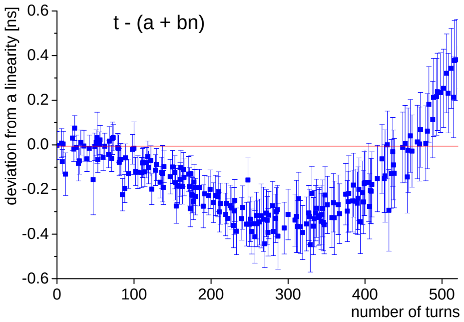

Figure 4.10: Deviation from a linearity for the time dependence of the turn number for a single particle.

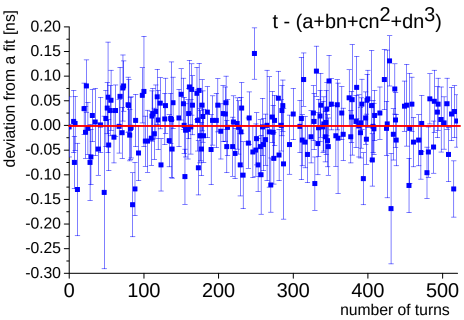

Figure 4.11: Residuum plot of the 3^{rd} order polynomial fit applied on a time dependence of the turn number.

The fitting procedure is based on the finding a minimum chi-square χ^2 for every parameter c_i [Kun99]

$$\chi^2 = \sum_{i=1}^{n} \frac{(t_i - t(x_i))^2}{\Delta t_i^2} = \min, \tag{4.14}$$

where the time $t(x)$ is described by the k-order polynomial function of revolution number x

$$t(x) = c_0 + c_1 x + c_2 x^2 + \cdots + c_k x^k, \tag{4.15}$$

where c_i are the parameters to be found,

$$\mathcal{C} = \begin{pmatrix} c_0 \\ c_1 \\ \dots \\ c_k \end{pmatrix}. \tag{4.16}$$

The measured times t_i and corresponding turn numbers x_i construct matrices $\mathcal{T}$ and $\mathcal{X}$ with n rows,

$$\mathcal{T} = \begin{pmatrix} t_1 \\ t_2 \\ \dots \\ t_n \end{pmatrix}, \quad \mathcal{X} = \begin{pmatrix} 1 & x_1 & \cdots & x_1^k \\ 1 & x_2 & \cdots & x_2^k \\ \vdots & \vdots & \ddots & \vdots \\ 1 & x_n & \cdots & x_n^k \end{pmatrix} \tag{4.17}$$

and the time uncertainties Δt_i the weighting matrix $\mathcal{P}$

$$\mathcal{P} = \begin{pmatrix} \frac{1}{(\Delta t_1)^2} & 0 & \cdots & 0 \\ 0 & \frac{1}{(\Delta t_2)^2} & \cdots & 0 \\ \vdots & \vdots & \ddots & \vdots \\ 0 & 0 & \cdots & \frac{1}{(\Delta t_n)^2} \end{pmatrix}. \tag{4.18}$$

The fitting parameters c_i with the uncertainties Δc_i are then calculated from the equations

$$\mathcal{C} = \left(\mathcal{X}^T \mathcal{P} \mathcal{X}\right)^{-1} \mathcal{X}^T \mathcal{P} \mathcal{T} \tag{4.19}$$

and

$$\Delta c_i = \sqrt{\left\{\left(\mathcal{X}^T \mathcal{P} \mathcal{X}\right)^{-1}\right\}_{ii}}. \tag{4.20}$$

The algorithm is programmed for various polynomial order k and various number of points n.

The revolution time used in the further analyses is then the slope of the fitted function at the first particle occurrence x_0

$$\tau = c_1 + 2c_2 x_0 + \cdots + k c_k x_0^{k-1} \tag{4.21}$$

with an average error

$$\sigma_{av}(\tau) = \sqrt{\sum_{i,j=1}^{k,k} ij \left\{\left(\mathcal{X}^T \mathcal{P} \mathcal{X}\right)^{-1}\right\}_{ij} x_0^{i-1} x_0^{j-1}} \tag{4.22}$$

and a scattering error

$$\sigma_{scat}(\tau) = \sigma_{av} \sqrt{\chi^2/(n-k-1)}. \tag{4.23}$$

The larger of both errors is used.

Polynomial functions with various orders were investigated to find an optimal function. The dependence of the time on the revolution number is fitted. The chi-square χ^2 of a fit is compared with the chi-square $\chi^2_{0.05}$, corresponding to a 95% level of confidence [PTVF92]. The ratio of fits that fulfill this condition is shown in Tab. 4.1. We have decided to use the 3-order polynomial fit, which describes most of the dependences, as shown in Fig. 4.11. Higher polynomial orders mean only a small increase of the fits fulfilling the 95% level of confidence condition. Only these, that fulfill this condition are then used in the later analyses.

polynomial order	$\chi^2 < \chi^2_{0.05}$
1^{st}	60.2%
2^{nd}	88.8%
3^{rd}	91.5%
4^{th}	93.4%
5^{th}	93.7%

Table 4.1: Ratio of the fits fulfilling the 95% level of confidence condition.

4.3 Identification

Once the particle is found and its revolution time is determined, it has to be identified to make a calibration and to determine mass values. As is described in Sec. 3.1, all nuclei of the same species and the same charge state are supposed to have same revolution time (in a case of a perfect isochronicity and a measurement uncertainties). If a particle's mass-to-charge ratio is unique[1], the revolution time of the particle identifies it unambiguously. If we histogram the revolution time spectrum of all measured nuclei, they create peaks consisting of particles of one species. The spectrum containing 70000 particles from the setting with Bρ=8.332Tm in the experiment with the uranium primary beam is shown in Fig. 4.12.

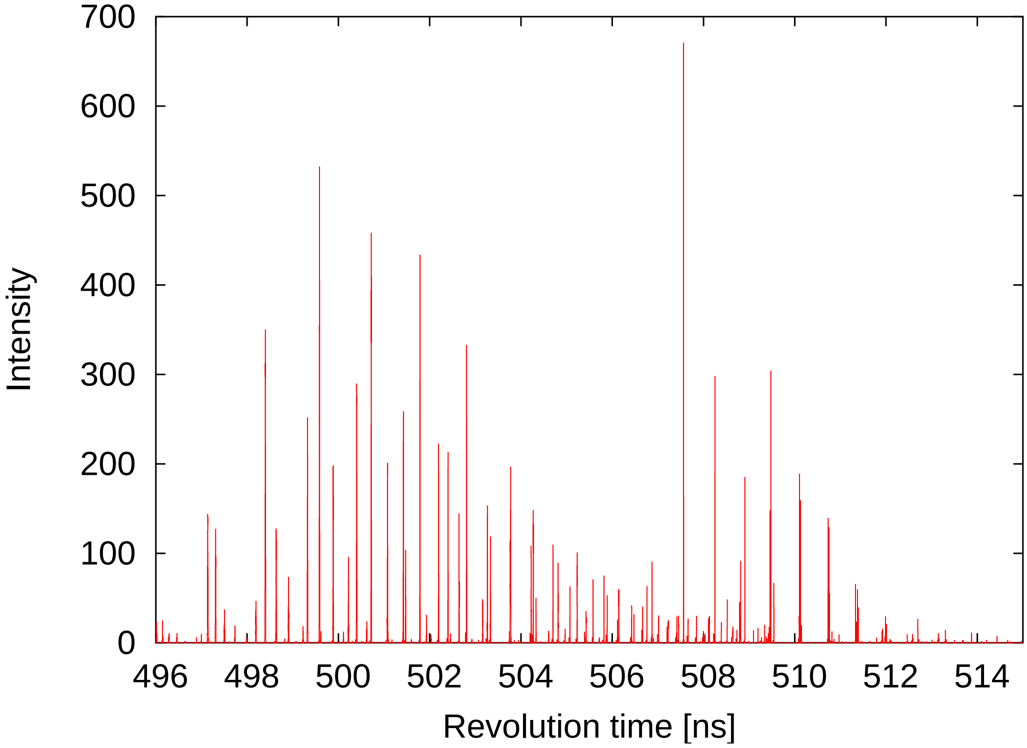

Figure 4.12: Spectrum produced from the histogram with revolution times in the experiment with the uranium primary beam. It contains 70000 particles from the setting with Bρ=8.332Tm.

In reality the isochronicity and the revolution time are not perfect and the revolution time varies around a central ideal revolution time value. The identification of the peaks is not a simple task; thus it requires a complex approach. The parameters of the storage ring are not known so exactly to be able to determine a

---

[1] Mass values are taken from [ABW03], where measured values for known masses and expected values unknown masses are collected.

revolution time vs. mass-to-charge relation on a very fine scale that corresponds to distances between the required peaks. A composition of the peaks produces an unique pattern, that should be a simple transformation of the pattern of corresponding mass-to-charge values. A fist task is to make the patterns to match to each other. The TOFSIM simulation, see Sec. 2.1.1, is a convenient tool for this purpose. It can simulate a spectrum pattern, that is supposed to me identical to the measured one, see Fig. 4.13, where comparison of a simulated and a measured spectra of the ^{135}Sn setting is shown. In the simulated spectrum we know an identity of every peak and therefore we can determine an identity of peaks in a measured spectrum by comparison. Every peak then requires a special investigations to verify its identity. Two different ions can have mass-to-charge ratios so similar, that the peaks cannot be resolved. Some nuclides can have an isomer, which has a mass usually only some hundred keV larger than the ground state ion. If the half-life of the isomer is long enough to be measured, the final peak is a mixture of both states particles and the mean value is shifted. Unfortunately it is impossible to predict an isomeric ratio and calculate the peak shift compared to the ground state, if an isomeric energy is not high enough to resolve the peaks. In these cases the particles are not identified, a peak is used in further analyses only if the identification is unambiguous. The mass measurement is a high preci-

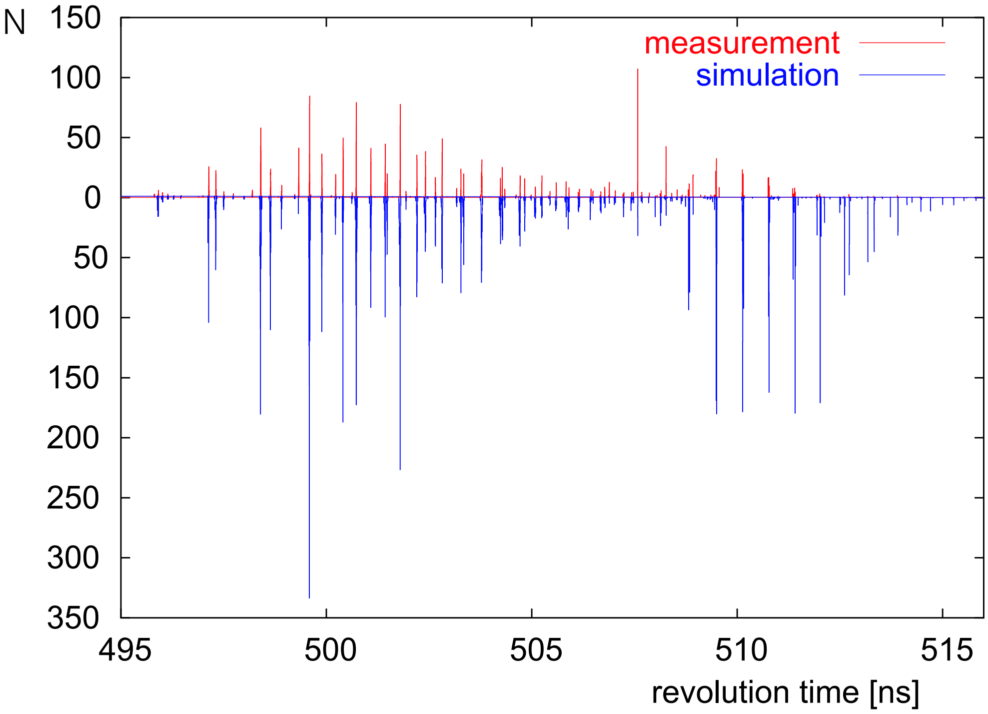

Figure 4.13: Comparison of a simulated and a measured spectrum from the setting of ^{135}Sn as a reference fragment. The simulation simplifies the identification of the ions.

sion experiment and a position of the peak has to be determined very precisely, so that no uncertainty in the identification may occur also for the ion lying on an edge of the peak. An example is shown in the Fig. 4.14, where the uncertainties in the identification of single ions can lead to mean value determination error up to several hundred keV.

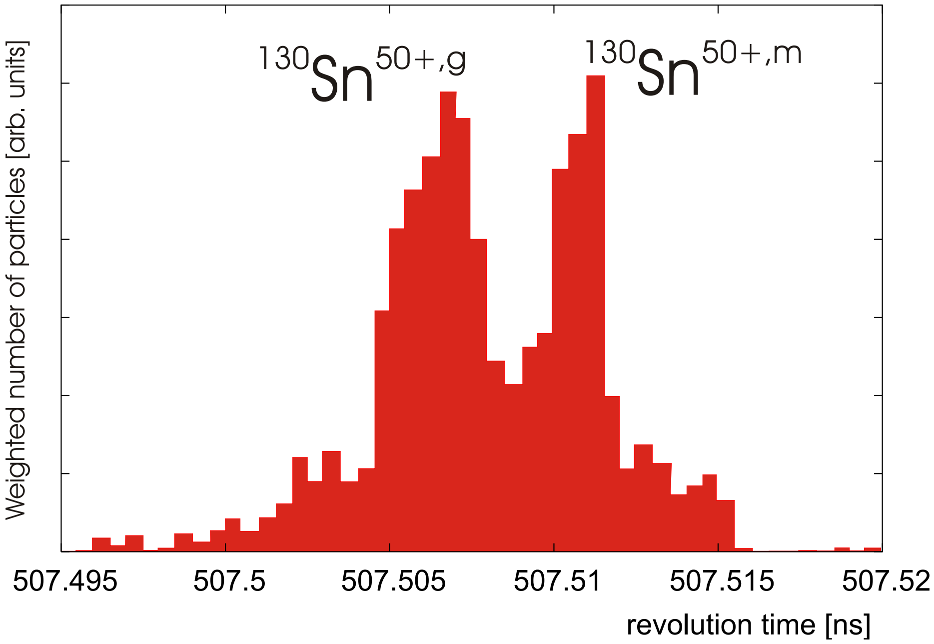

Figure 4.14: Example of peaks resolved in the measured revolution time spectrum. One peak corresponds to the ground state of the ^{130}Sn, the second one is the isomer of ^{130}Sn with the excitation energy of 1.946 MeV.

The weighted mean revolution time $\bar{t}$ is calculated using the equation

$$\bar{t} = \frac{\sum\limits_i \frac{t_i}{\sigma_i^2}}{\sum\limits_i \frac{1}{\sigma_i^2}}, \tag{4.24}$$

with an average error

$$\bar{\sigma}_{av} = \sqrt{\frac{1}{\sum\limits_i \frac{1}{\sigma_i^2}}} \tag{4.25}$$

and a scattered error

$$\bar{\sigma}_{scat} = \sqrt{\frac{\sum\limits_i \frac{1}{\sigma_i^2}(\bar{t} - t_i)^2}{(n-1)\sum\limits_i \frac{1}{\sigma_i^2}}}. \tag{4.26}$$

The larger of the average error and the scattered error is taken as the error of the mean value.

4.4 Area of Isochronicity in the ^{238}U Experiment

Ions of one species have the same revolution time only if isochronicity is fulfilled. If it is not fulfilled, the peak in the revolution time spectrum is wide and the mean value is determined with a larger uncertainty. The isochronicity can be expressed by an isochronicity curve, see Sec. 3.1.2. The isochronicity curve depends on the storage ring setting and the mass-to-charge ratio of the ion, see its transformation for a certain mass-to-charge ratio in Sec. 3.1.3. The isochronicity curve transformed for various mass-to-charge ratios is shown in Fig. 4.15. All the curves are describing the ESR setting with Bρ=7.332Tm, but for different species. It is obvious, that the isochronicity is best for m/q=2.69 and is get-

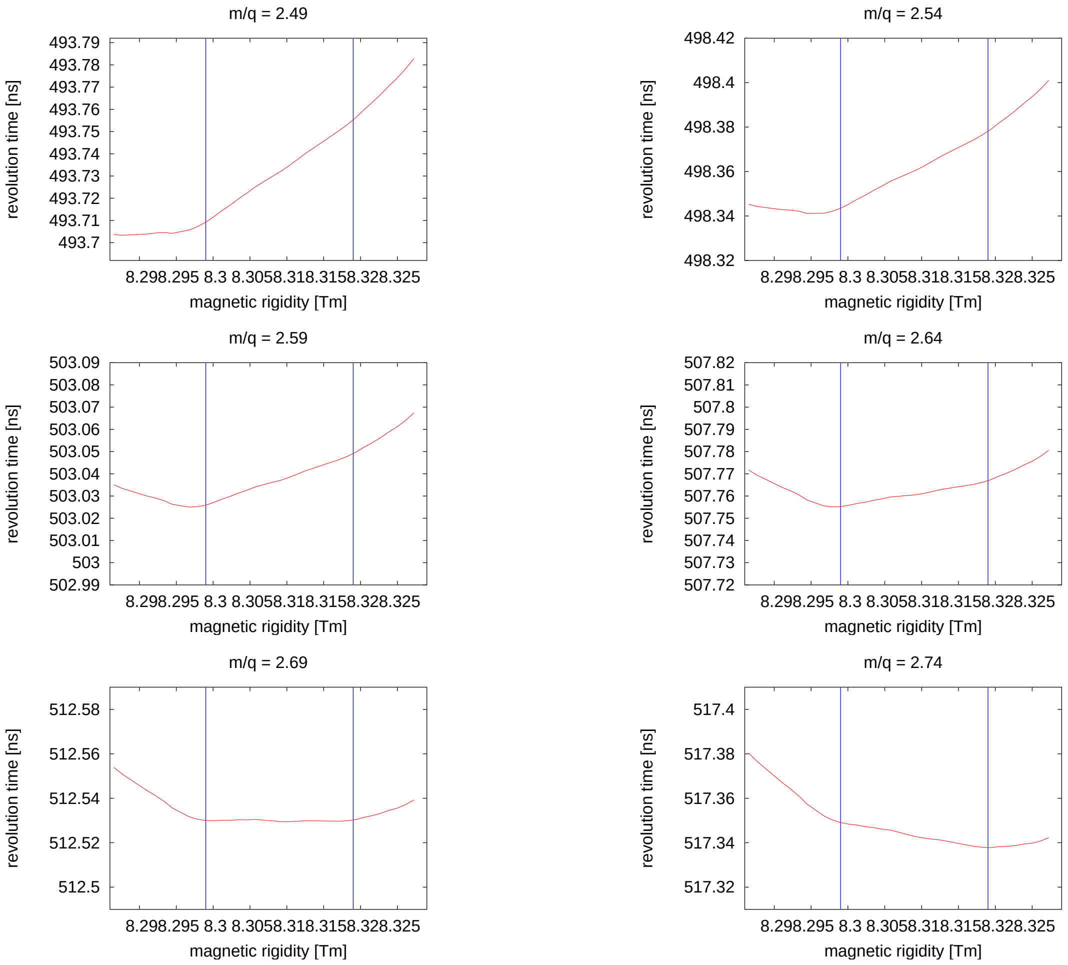

Figure 4.15: Transformations of the isochronicity curve for various mass-to-charge ratios. All the curves are describing the same ESR setting with Bρ=7.332Tm. Blue lines show the magnetic rigidity restriction by scrapers. Isochronicity is different for various species. The best isochronicity is in the area of m/q=2.69.

ting worse further from this mass-to-charge value. This is confirmed by analyses of widths of revolution time peaks, see Fig. 4.16. The standard deviation σ of the revolution time distribution is calculated for single peaks to determine their widths. A trend supporting the isochronicity behavior in the Fig. 4.15 is apparent. The best resolution is reached for $m/q \approx 2.68$, where the standard deviation reaches 0.5 ps. For $\tau \approx 500$ ns it means a maximum time resolution

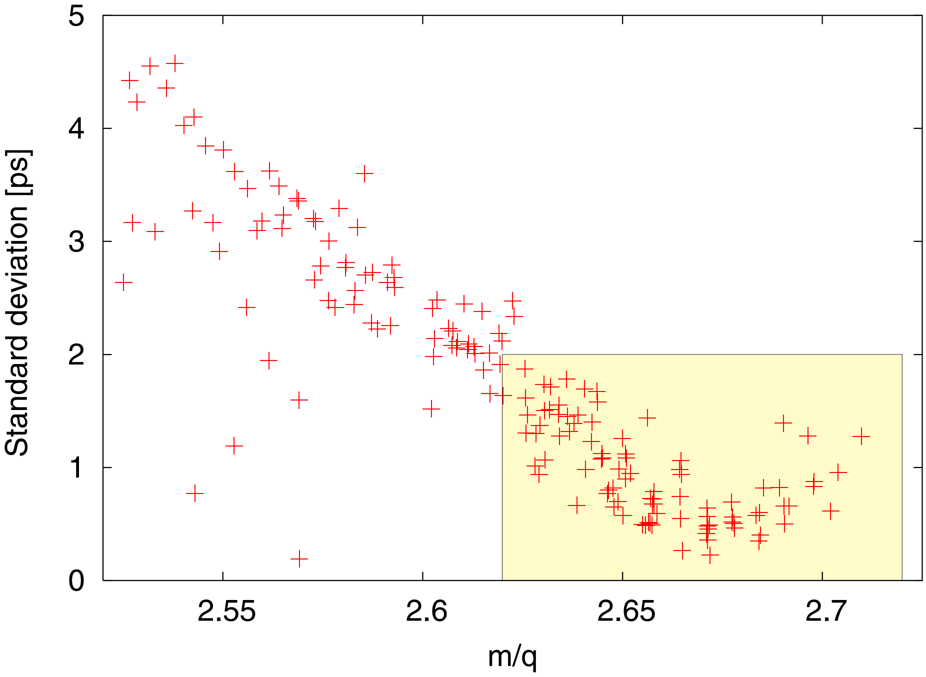

Figure 4.16: Standard deviation σ of revolution time distributions of single peaks for various mass-to-charge ratios in the ESR setting with Bρ=7.332Tm. Only the marked area between m/q=2.62–2.72, where $\sigma < 2$ ps, is analyzed.

$$\frac{\tau}{2\sigma(\tau)} \approx 5 \times 10^5 \qquad \text{resp.} \qquad \frac{\tau}{\mathrm{FWHM}(\tau)} \approx 4 \times 10^5 \tag{4.27}$$

and a maximum mass resolution

$$\frac{m/q}{2\sigma(m/q)} \approx 2.5 \times 10^5 \qquad \text{resp.} \qquad \frac{m/q}{\mathrm{FWHM}(m/q)} \approx 2 \times 10^5. \tag{4.28}$$

The mass resolution can be determined from Eq. 3.17 modified for the isochronicity case,

$$\frac{d\tau}{\tau} = -\alpha_p \frac{d\left(\frac{m}{q}\right)}{\frac{m}{q}}, \tag{4.29}$$

where the momentum compaction value in our measurements is $\alpha_p \approx 0.5$. This can also be shown easily from the spectrum and its identifications.

As it was mentioned above, the statistical uncertainty grows with peak width. So we have decided to limit our analyses to some level of isochronicity. A moderate requirement would be to have a statistical uncertainty of 100 keV for a peak with 50 particles corresponding to the statistical error of the mean revolution time determination to be $\Delta\tau \approx$ of 0.25ps for a charge $Q = 40$. This can be obtained from a standard deviation $\sigma(\tau)$

$$\Delta\tau = \frac{\sigma(\tau)}{\sqrt{n}}, \tag{4.30}$$

where n is a number of particles. For $n = 50$ we end up at the standard deviation limitation $\sigma_{limit}(\tau) \approx 2$ ps.

The non-isochronicity increases the statistical error, yet it causes a systematic error as well. Such a systematic error arises from nonuniform Bρ distribution at the injection into the ESR, see Sec. 3.7. It can cause a shift of the mean revolution time compared to the center of revolution times possible for one species, which is supposed to be equal to the mean revolution time in a case of a uniform Bρ distribution, up to 10% of a standard deviation σ. The revolution time standard deviation limit of 2ps is marked in Figs. 4.16–4.18. Only an area that falls within

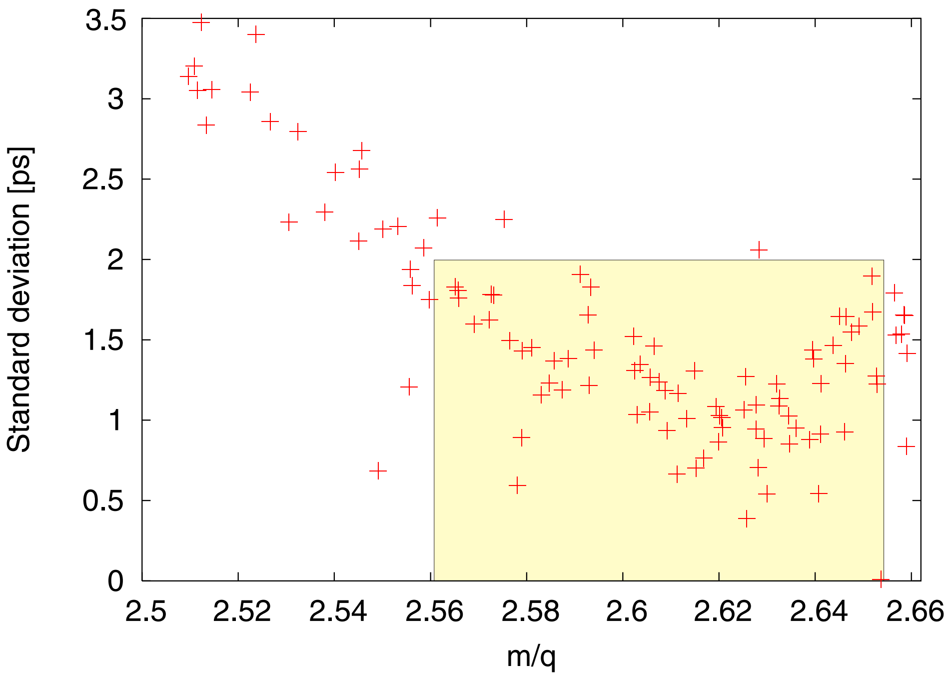

Figure 4.17: Standard deviation σ of revolution time distributions of single peaks for various mass-to-charge ratios in the ESR setting with Bρ=8.209Tm. Only a marked area between 2.56–2.65, where $\sigma < 2$ ps, is analyzed.

this limit is used for analyses. The best isochronicity is reached for $m/q \approx 2.68$ in the ESR setting with Bρ=7.332Tm. In this setting we have enclose the working space to $2.62 < m/q < 2.72$, see Fig. 4.16. A worse isochronicity was reached in the ESR setting with Bρ=8.209Tm, but still good enough to fulfill our conditions. We have limited the area to be analyzed to $2.56 < m/q < 2.65$. As it was mentioned above, the isochronicity is getting worse with getting further from the central mass-to-charge ratio, for which isochronicity is the best. In general the area fulfilling our conditions is

$$\frac{\Delta(m/q)}{m/q} \approx 3 - 4\,\%. \tag{4.31}$$

This value has to be taken into an account in future experiment preparations.

The situation is different for the measurement in the storage ring setting with Bρ=7.5321Tm, see Fig. 4.18. The isochronicity achieved was too poor to get relevant data from the spectra. As the statistics was easy to reach, the situation could be improved by scrapers, which can narrow down the Bρ acceptance and consequently also the revolution time peaks.

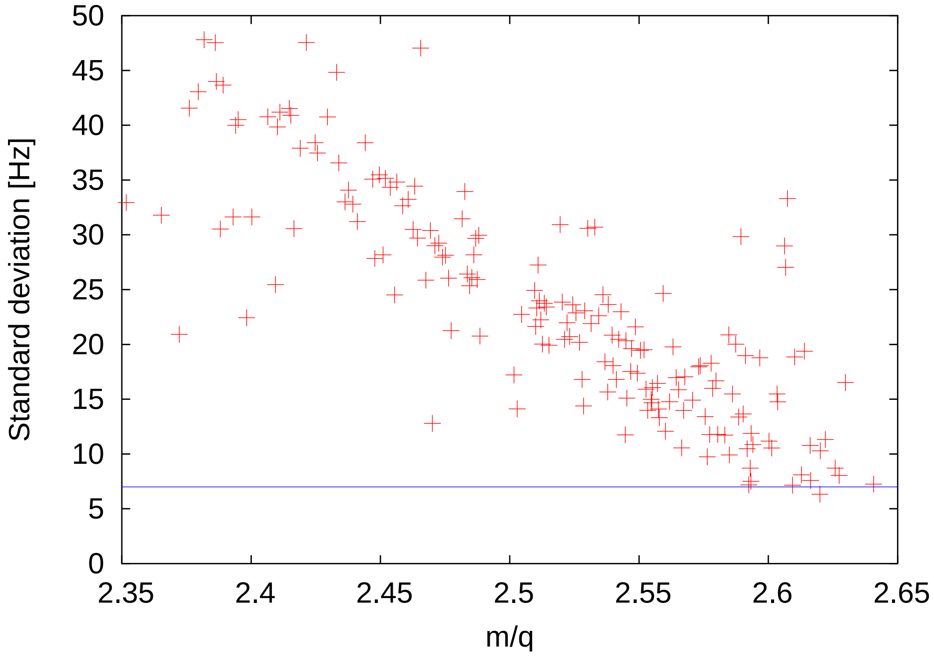

Figure 4.18: Standard deviation σ of revolution time distributions of single peaks for various mass-to-charge ratios in the ESR setting with Bρ = 7.5321Tm. An isochronicity limit 2 ps was not reached.

4.5 Area of Isochronicity in the ^{70}Zn Experiment

As it was mentioned above, the isochronicity is achieved if the last term in Eq. 3.17 is eliminated by fulfilling the condition $\gamma_t = \gamma$. The transition point is a function of the magnetic rigidity $B\rho$ and all ions of one species revolve isochronously if this condition is fulfilled for all magnetic rigidities inside the ring acceptance. An installation of the isochronicity in the storage ring requires a fine tuning of the magnetic optics. In the setting where isochronicity was optimized for $^{57}\mathrm{Ti}^{22+}$ we have obtained the behavior of γ_t for various magnetic rigidities that is shown in Fig. 4.19. The curve is compared with the γ value of $^{57}\mathrm{Ti}^{22+}$ for a corresponding magnetic rigidity. The agreement, which is a requirement for the isochronicity, is achieved in the range of the magnetic rigidity between 7.511 Tm and 7.532 Tm. As a limit we have defined the disagreement of 2% so that

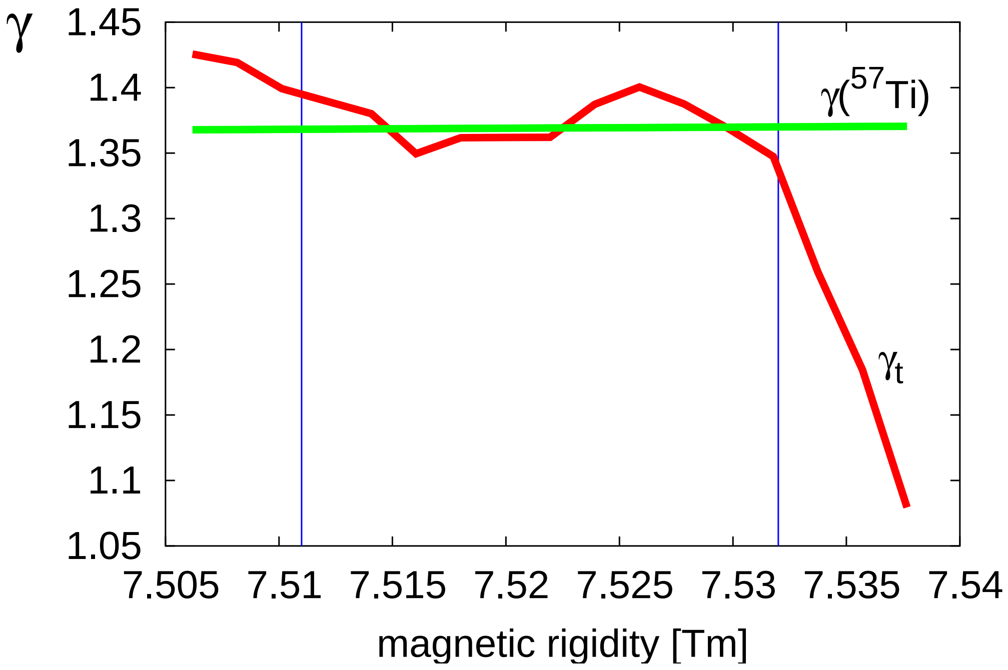

Figure 4.19: Dependence of the transition point γ_t for magnetic rigidities within the storage ring acceptance. It is compared with the Lorentz factor γ. The storage ring acceptance was limited by the scrapers, which are indicated by vertical lines.

$$\frac{|\gamma - \gamma_t|}{\gamma} < 0.02. \tag{4.32}$$

To get rid of the non-isochronous part of the curve we applied scrapers inside the storage ring that limited the magnetic rigidity acceptance as it is shown in Fig. 4.19 by vertical lines. It is confirmed by the curve transformed into the revolution time as a function of the magnetic rigidity for various mass-to-charge ratios (see Fig. 4.20). The transformation for the mass-to-charge ratio of 2.59 is the one corresponding to $^{57}\mathrm{Ti}^{22+}$. We can see that the scrapers enable magnetic rigidities only in the area of isochronicity. The revolution time is varying only about 0.1 ns between vertical lines symbolizing the scrapers position. The isochronicity was achieved for the mass-to-charge ratio of 2.59, which is in agreement with our expectations. It is evident from the figure, that the further a mass-to-charge of a species is from m/q=2.59, the less the isochronicity is fulfilled.

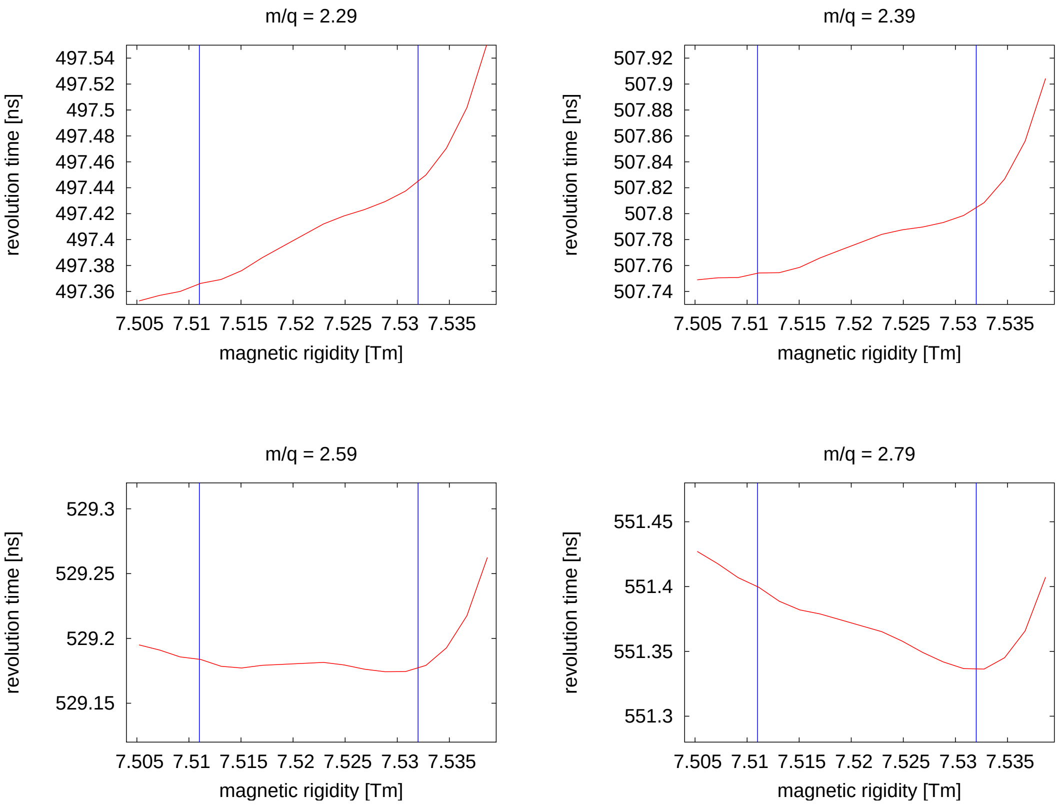

Figure 4.20: Transformations of the isochronicity curve for various mass-to-charge ratios. All the curves describe the storage ring setting of $^{57}\mathrm{Ti}^{22+}$ as a reference fragment. Isochronicity is different for various species. The isochronicity was achieved in the area of m/q=2.59 corresponding to $^{57}\mathrm{Ti}^{22+}$, that is in agreement with our expectations.

Standard deviations σ of the revolution times for various mass-to-charge ratios are shown in Fig. 4.21. As we expected, the widths of the peaks are the smallest

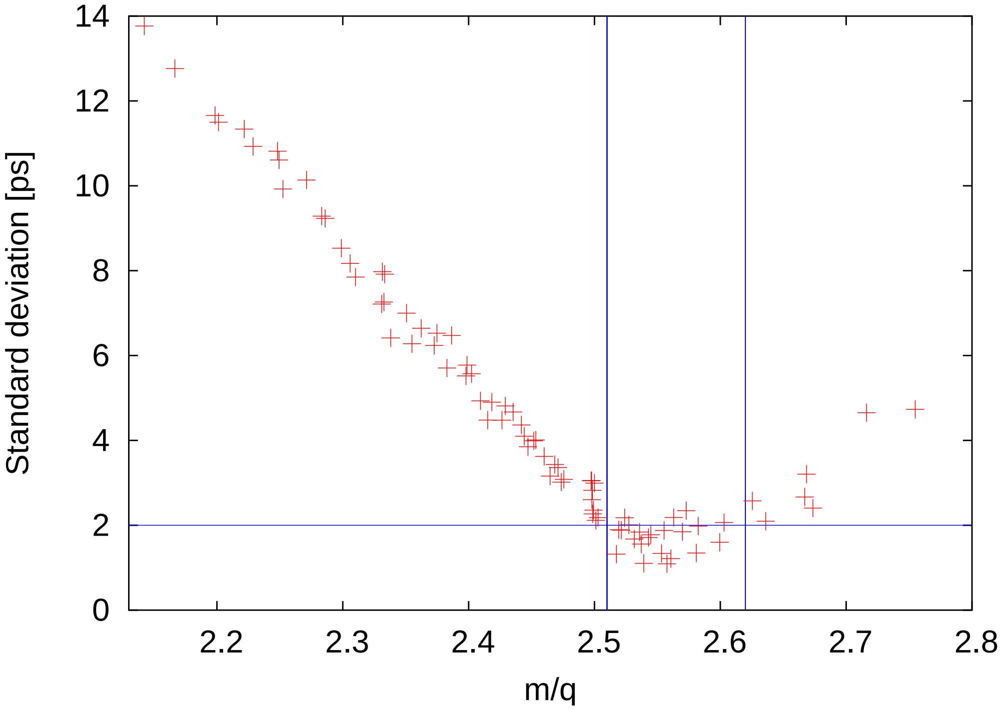

Figure 4.21: Standard deviations of revolution times for various mass-to-charge ratios. The horizontal lines marks the isochronicity level $\sigma < 2\ ps$. The vertical lines specify the area, where the isochronicity condition was fulfilled. Only these part was used in analysis.

in the area, where isochronicity is fulfilled. The isochronicity is a necessary condition of our method, hence we have limited our analyses only to the region, where $\sigma < 2\ ps$.

4.6 Contributions of Different Uncertainties to the Revolution Time Determination

The total standard deviations of the revolution time distribution are investigated to compare it with the contribution from the analyses uncertainties. The value is always determined for all M particles of one species with corresponding number of signals $N_j + 1$ for the particle j. The revolution time is determined from the times t of the consecutive signals and corresponding number of revolution n

$$\tau_i = \frac{t_i - t_{i-1}}{n_i - n_{i-1}}. \tag{4.33}$$

Therefore the number of the determined revolution times is one less than is the number of the signals. The mean revolution time $\bar{\tau}$ for one species is calculated from the following equation

$$\bar{\tau} = \frac{\sum_{j=1}^{M} \sum_{i=1}^{N_j} \frac{t_{ji} - t_{j(i-1)}}{n_{ji} - n_{j(i-1)}}}{\sum_{j=1}^{M} N_j}. \tag{4.34}$$

The standard deviation σ_τ of the same species is determined as

$$\sigma_\tau = \sqrt{\frac{\sum_{j=1}^{M} \sum_{i=1}^{N_j} \left((t_{ji} - t_{j(i-1)}) - (n_{ji} - n_{j(i-1)}) \times \bar{\tau} \right)^2}{\left(\sum_{j=1}^{M} N_j \right) - 1}}. \tag{4.35}$$

In Fig. 4.22 the distributions for non-isochronous $^{91}\mathrm{Kr}^{36+}$ and for isochronous $^{139}\mathrm{Te}^{52+}$ are shown.

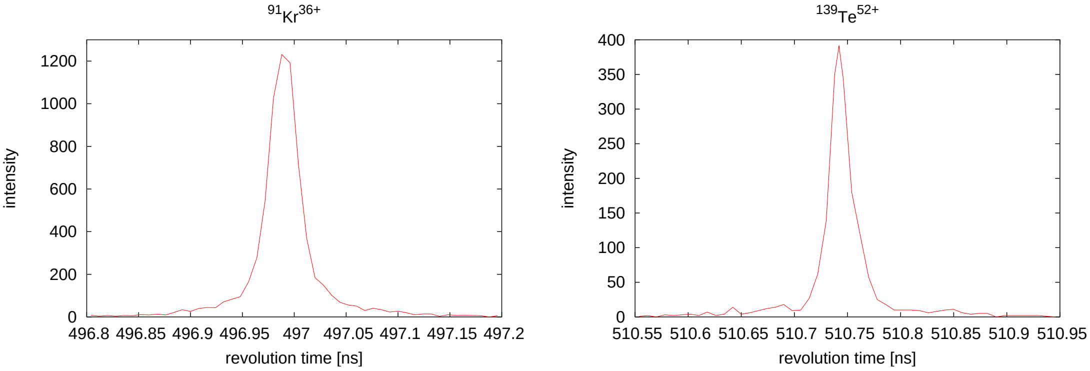

Figure 4.22: Distribution of the revolution time values determined from the consecutive signals. The standard deviation for non-isochronous $^{91}\mathrm{Kr}^{36+}$ with m/q = 2.525 is 123 ps, for isochronous $^{139}\mathrm{Te}^{52+}$ with m/q = 2.671 it is 85 ps.

The standard deviations σ for various species as a function of mass-to-charge ratio is shown in Fig. 4.23. In the figure total widths of the revolution time distribution are shown. The analyses contribution of 66ps is subtracted from these values to show the influence of other factors, mainly the non-isochronicity. It is evident that only in the area of the isochronicity (see also Sec. 4.4) the contribution coming from the analysis is higher than the one coming from the non-isochronicity.

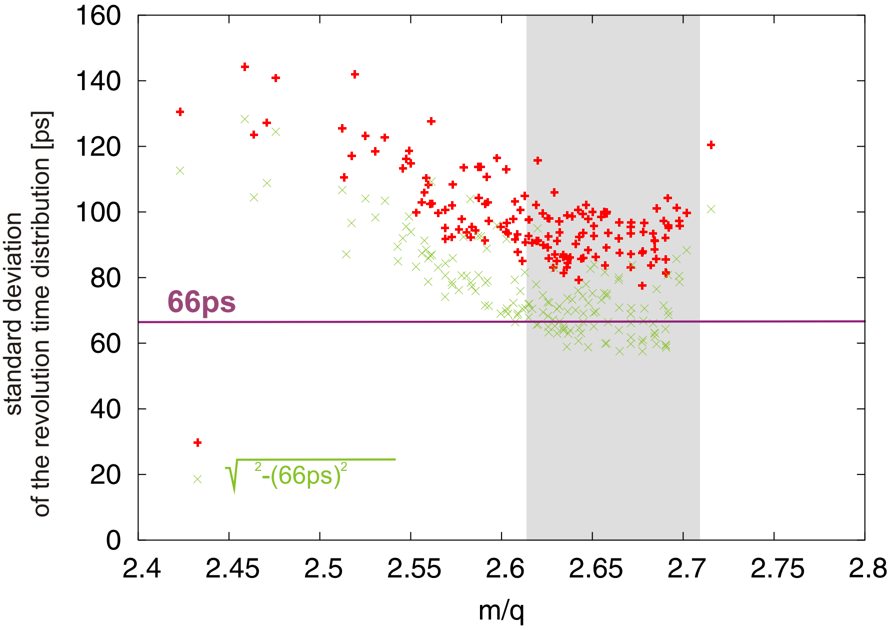

Figure 4.23: The total width of revolution time distribution for single species (red points) consists of the analyses contribution (magenta line) and non-isochronicity contribution (green points). The contribution from analyses has a statistical origin and therefore can be reduce with a higher statistics. This is not case for the non-isochronicity contribution that has an origin in systematics. The grey area was used in analysis.

The total distribution width of the revolution time for ^{91}Kr^{36+} is 123 ps, It consists of the intrinsic uncertainty of the start and stop signal $66\text{ps} = \sqrt{2 \times 47\text{ps}}$ and the non-isochronicity contribution of 105ps.

In the case of ^{139}Te^{52+} the total distribution width of the revolution time is 85 ps. The intrinsic uncertainty of 66ps is higher than the non-isochronicity contribution of 55ps. The revolution time distribution width of 85 ps corresponds to mass distribution width of 47 MeV. On the level of signal processing we are therefore not able to resolve the changes within several tens of MeV, for example in the isomeric decay. If the half-life of the isomer is in the range between $1\mu s$ and $1ms$, it could decay during revolving in the storage ring and we would not be able to resolve it. In such a case an improvement of the time determination would be required. This can be achieved by further development of the micro-channel plates detector and electronics.

The distribution width coming from analyses has a statistical origin and therefore its contribution to the final uncertainty can be reduced with a higher statistics, as is shown in Sec. 4.2. This is not case for the distribution width coming from the non-isochronicity that has an origin in systematics, see Sec. 4.4. In the area of isochronicity we have obtained the resolution of 1 ps, which allows us to resolve isomers of 500 keV. The resolved isomer of 1.95 MeV is shown in Fig. 4.14.

4.7 Mass Determination

After determination of the frequency for every peak in the isochronous part of the spectra and their identification mass-to-charge values can be assigned. Obviously a mass value of the nuclide is known only with some uncertainty or is completely unknown. Our task is to determine these mass values, which were unknown before. To do this we have to find out a relation between measured frequency and the corresponding mass-to-charge ratio. The spectrum consists of the peaks of isotopes with unknown masses as well as the isotopes with well known masses, which are used as reference values, see Figs. 4.24–4.25.

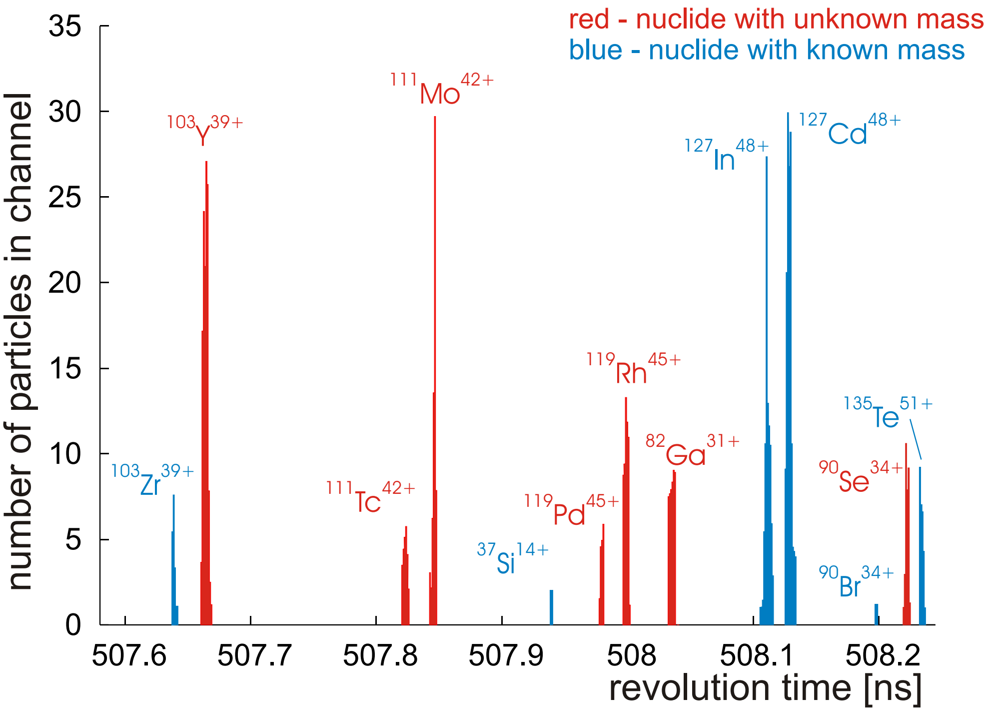

Figure 4.24: Part of the spectrum from the uranium experiment with Bρ=8.332Tm shown in Fig. 4.12. The spectrum consists of the peaks of isotopes with unknown masses as well as the isotopes with well known masses, which can be used as reference values.

Since we do not know the real behavior of such a relation from physical conditions of measurements we have to fit the chosen reference mass values by various curves. It should be emphasized here that the task is to get the simplest function with a number of parameters much lower than a number of nuclides with known masses which we would like to use as reference values.

For a relatively small part of a curve it is natural to use a polynomial function

$$\frac{m}{q}(f) = a_0 + a_1 f + a_2 f^2 + \cdots + a_k f^k. \tag{4.36}$$

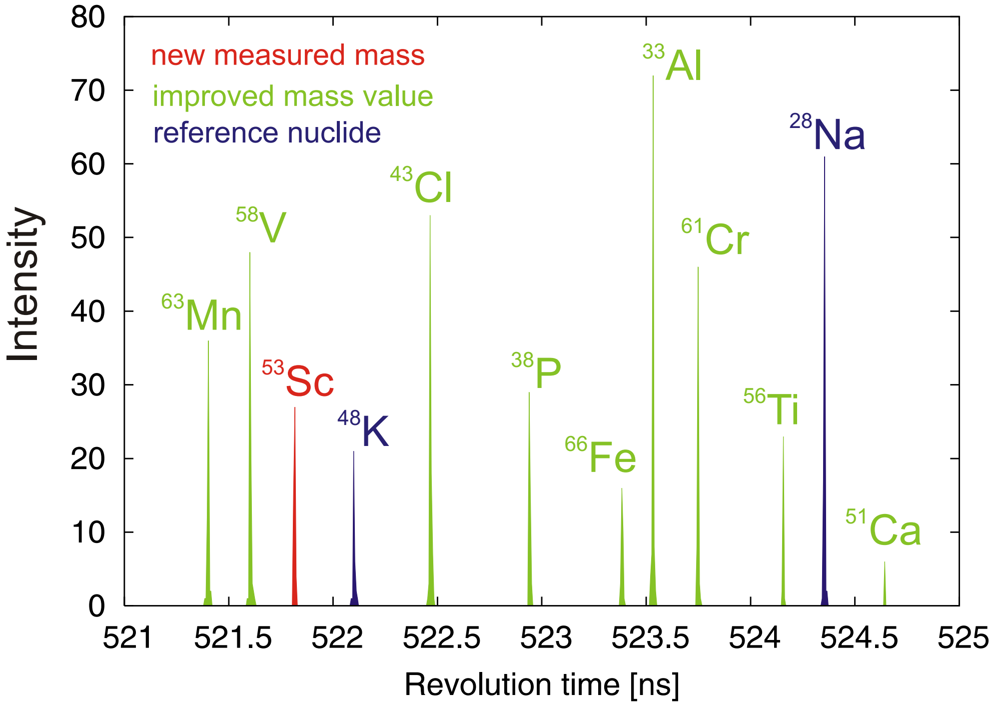

Figure 4.25: Part of the spectrum from the ^{70}Zn experiment. The spectrum consists of the peaks of isotopes with unknown masses, the isotopes with masses known with large uncertainties, for which we have improved the precision and the isotopes with well known masses, which can be used as reference values.

From general considerations we could not expect the curve to be linear. However fit functions consisting polynomials with a higher order could be tested. Here we can restrict ourself to the condition that the last order in the fitting function should have the corresponding coefficient higher than is its error. If the coefficient has after a fitting the error higher than its value we can cancel the corresponding order and a function with the order one degree lower.

After investigations with various orders of the polynomial function we have observed 3^{rd} order polynomial function to be optimal. This finding was also supported by the fact that normalized chi-square

$$\chi^2_{norm} = \frac{\chi^2}{n-p} \tag{4.37}$$

reaches its minimum for 4 parameters, where n is the number of reference masses and p is a number of parameters.

The fitting procedure is done using the same algorithm as is explained in Eq. 4.14–4.23 extended with a variable error Δf. Minimization is therefore based on an extended χ^2

$$\chi^2 = \sum_{i=1}^{n} \frac{\left[\left(\frac{m}{q}\right)_i - \sum_{k=0}^{p-1} a_k f_i^k\right]^2}{\left(\Delta\frac{m}{q}\right)_i^2 + \left[\Delta f \times \sum_{k=0}^{p-1} k a_k f_i^{k-1}\right]^2} = \text{min.} \tag{4.38}$$

where the final uncertainty of one point is a superposition of the uncertainty of the mass-to-charge ratio and the frequency uncertainty. The frequency uncertainty is transformed to the mass-to-charge representation by multiplying with a first derivative

$$\left(\Delta\frac{m}{q}\right)_{f_i} = \frac{d\frac{m}{q}(f)}{df}\Delta f_i = \sum_{k=0}^{p-1} k a_k f_i^{k-1} \times \Delta f_i. \tag{4.39}$$

As this problem has no analytical solution, the so-called confluence analysis is used. It is based on an analytical solution without the variable error Δf, using the matrix method,

$$\mathcal{A} = \left(\mathcal{F}^M \mathcal{P} \mathcal{F}\right)^{-1} \mathcal{F}^T \mathcal{P} \mathcal{M} \tag{4.40}$$

where the matrices are defined as

$$\mathcal{A} = \begin{pmatrix} a_0 \\ a_1 \\ \cdots \\ a_{p-1} \end{pmatrix}, \quad \mathcal{M} = \begin{pmatrix} (m/q)_1 \\ (m/q)_2 \\ \cdots \\ (m/q)_n \end{pmatrix}, \quad \mathcal{F} = \begin{pmatrix} 1 & f_1 & \cdots & f_1^{p-1} \\ 1 & f_2 & \cdots & f_2^{p-1} \\ \vdots & \vdots & \ddots & \vdots \\ 1 & f_n & \cdots & f_n^{p-1} \end{pmatrix} \tag{4.41}$$

and the weighting matrix $\mathcal{P}$ combines the m/q uncertainties $(\Delta m/q)_i$

$$\mathcal{P} = \begin{pmatrix} \frac{1}{\left(\Delta\frac{m}{q}\right)_1^2} & 0 & \cdots & 0 \\ 0 & \frac{1}{\left(\Delta\frac{m}{q}\right)_2^2} & \cdots & 0 \\ \vdots & \vdots & \ddots & \vdots \\ 0 & 0 & \cdots & \frac{1}{\left(\Delta\frac{m}{q}\right)_n^2} \end{pmatrix}. \tag{4.42}$$

Parameters a_i found in this first step are used to fix $\left(\Delta\frac{m}{q}\right)_{f_i}$ from Eq. 4.39 and the procedure is repeated with minimizing

$$\chi^2 = \sum_{i=1}^{n} \frac{\left[\left(\frac{m}{q}\right)_i - \sum_{k=0}^{p-1} a_k f_i^k\right]^2}{\left(\Delta\frac{m}{q}\right)_i^2 + \left(\Delta\frac{m}{q}\right)_{f_i}^2} = \text{min.} \tag{4.43}$$

which is realized by replacing $(\Delta\frac{m}{q})_i^2$ with $(\Delta\frac{m}{q})_i^2+(\Delta\frac{m}{q})_{f_i}^2$ in the weighting matrix $\mathcal{P}$

$$\mathcal{P} = \begin{pmatrix} \frac{1}{(\Delta\frac{m}{q})_1^2+(\Delta\frac{m}{q})_{f_1}^2} & 0 & \cdots & 0 \\ 0 & \frac{1}{(\Delta\frac{m}{q})_2^2+(\Delta\frac{m}{q})_{f_2}^2} & \cdots & 0 \\ \vdots & \vdots & \ddots & \vdots \\ 0 & 0 & \cdots & \frac{1}{(\Delta\frac{m}{q})_n^2+(\Delta\frac{m}{q})_{fn}^2} \end{pmatrix}. \tag{4.44}$$

The iterations are repeated until the parameters a_i converge to the resultant values, i.e. until the parameters do not change in a single iteration.

After the calibration function has been obtained, we can determine the unknown mass-to-charge values from their frequencies using Eq. 4.36. An average error of the fitted value is calculated using

$$\sigma_{fit_{av}}(m/q) = \sqrt{\sum_{k,l=0}^{n,n} \left\{(\mathcal{F}^T\mathcal{P}\mathcal{F})^{-1}\right\}_{kl} f^k f^l} \tag{4.45}$$

and a scattering error

$$\sigma_{fit_{scat}}(m/q) = \sqrt{\chi^2/(n-p)}\ \ \sigma_{fit_{av}}, \tag{4.46}$$

where the larger error is used as a fitting error σ_{fit}. This is the error from the fitting only and the error of the frequency itself is not included. Its contribution to the final error is

$$\sigma_{freq}(m/q) = \sum_{k=0}^{p-1} k a_k f^{k-1} \times \Delta f. \tag{4.47}$$

The full statistical error is therefore a quadratic sum of σ_{fit} and σ_{freq}

$$\sigma_{stat}\left(\frac{m}{q}\right) = \sqrt{\left[\sigma_{fit}\left(\frac{m}{q}\right)\right]^2 + \left[\sigma_{freq}\left(\frac{m}{q}\right)\right]^2}. \tag{4.48}$$

The systematic error σ_{syst} is calculated from comparison with all table values $\left(\frac{m}{q}\right)_i^{table}$ and their uncertainties $\sigma_{table}\left(\frac{m}{q}\right)_i$, that were already known [ABW03], so that

$$\chi^2 = \sum_{i=1}^{n} \frac{\left[\left(\frac{m}{q}\right)_i^{exp} - \left(\frac{m}{q}\right)_i^{table}\right]^2}{\left[\sigma_{stat}\left(\frac{m}{q}\right)_i\right]^2 + \left[\sigma_{table}\left(\frac{m}{q}\right)_i\right]^2 + \sigma_{syst}^2} = 1 \tag{4.49}$$

and the final error of one mass-to-charge value is

$$\sigma\left(\frac{m}{q}\right) = \sqrt{\left[\sigma_{stat}\left(\frac{m}{q}\right)\right]^2 + \sigma_{syst}^2}. \tag{4.50}$$

The mass value m is then determined by multiplication with the charge q.

There are several nuclides that appeared more than one time in our results. They could be in both settings or in two different charge states. In this case a weighted average is calculated

$$\bar{m} = \frac{\sum \frac{m_i}{\sigma_i^2}}{\sum \frac{1}{\sigma_i^2}} . \tag{4.51}$$

The corresponding average uncertainty is then

$$\sigma(m)_{av} = \sqrt{\frac{1}{\sum \frac{1}{\sigma_i^2}}} \tag{4.52}$$

and the scattering uncertainty

$$\sigma(m)_{scat} = \sqrt{\frac{\sum \frac{1}{\sigma_i^2}(m_i - \bar{m})^2}{(n-1)\sum \frac{1}{\sigma_i^2}}}. \tag{4.53}$$

The higher value is then taken as the final error, in most cases it is the average error $\sigma(m)_{av}$.

As it will be shown later in results, the typical relative uncertainty achieved is 2×10^{-6}.

Chapter 5

Results

The results from the experiments and the analysis are presented in this chapter.

5.1 Results from the ^{70}Zn Experiment

For the calibration of the mass spectra the reference masses which are listed in Table 5.1 were used. Table 5.2 shows the results of our mass determination of Zn-fragmentation products. Our data for mass excess ME(IMS) are presented in the 4^{th} column, whereas the data of AME-2003 [ABW03], collecting all previous measurements, are given in the 5^{th} column. The comparison is presented in the 6^{th} column. The nuclides listed in this table fulfilled the isochronicity condition. Among them we have identified $^{13}B(T_{1/2} = 17ms)$, the nuclide with the shortest half-life observed in the storage ring.

element	A	mass excess [keV]
Be	10	12606.7(0.4)
B	13	16562.2(1.1)
C	15	9873.1(0.8)
N	18	13114(19)
O	20	3797.5(1.1)
O	21	8063(12)
Ne	26	430(27)
Na	28	−989(13)
Mg	31	−3217(12)
K	48	−32124(24)

Table 5.1: List of the nuclides, which were used as the reference masses. Mass values are from [ABW03].

In general the appropriate choice of reference masses is a challenging task. However in the Zn-fragmentation we observed nuclides, which are close to the β-

Elem.	A	$\mathrm{ME}_{\mathrm{IMS}}$ [keV]	$\mathrm{ME}_{\mathrm{AME}}$ [keV]	$\mathrm{ME}_{\mathrm{IMS}}$ $-\mathrm{ME}_{\mathrm{AME}}$ [keV]
F	23	3310(40)	3330(80)	−20(90)
Al	33	−8500(60)	−8530(70)	30(90)
Al	34	−2980(90)	−2930(110)	−50(140)
Si	36	−12460(70)	−12480(120)	20(140)
P	38	−14640(70)	−14760(100)	120(120)
P	39	−12670(130)	−12870(100)	200(170)
S	41	−19090(70)	−19020(120)	−70(140)
Cl	43	−24130(80)	−24170(160)	40(180)
Cl	44	−20600(150)	−20230(110)	−370(190)
Ar	46	−29820(100)	−29720(40)	−100(100)
K	49	−29790(210)	−30320(70)	530(220)
Ca	51	−36560(170)	−35860(90)	−700(190)
Sc	53	−38840(110)	−37620$^{\#}$(300$^{\#}$)	−1222(320)
Sc	54	−34520(210)*	−34220(370)	−300(430)
Ti	56	−39420(120)	−38940(200)	−480(230)
Ti	57	−34560(380)	−33540(460)	−1020(600)
V	58	−40360(100)	−40210(250)	−150(270)
V	59	−37890(120)	−37070(310)	−820(330)
V	60	−33430(200)*	−32580(470)	−850(510)
Cr	61	−42550(110)	−42180(250)	−370(270)
Cr	62	−41010(110)	−40410(340)	−600(360)
Cr	63	−36160(430)	−35530$^{\#}$(300$^{\#}$)	−630(520)
Mn	63	−47040(100)	−46350(260)	−690(280)
Mn	64	−43110(120)*	−42620(270)	−490(300)
Fe	66	−50240(140)	−49570(300)	−670(330)
Fe	67	−46240(410)*	−45690(420)	−550(590)

Table 5.2: Mass excess values $\mathrm{ME}_{\mathrm{IMS}}$ determined in the Zn-fragmentation experiment compared with the values from AME-2003 [ABW03]. The masses labeled with $^{\#}$ are predicted values from extrapolations. For the nuclides labeled with * their isomeric states were taken into account.

stability line and thus whose masses have been very precisely measured in binary reactions with a high level of confidence and thus serve for calibration. Some of the masses of nuclides used as references (^{26}Ne, ^{28}Na, ^{31}Mg) have been measured directly (see AME-2003 [ABW03]).

A favorable circumstance in the region under investigation is also the absence of long-lived isomeric states for most of the nuclides. Even if they exist their half-lives are too short to be observed in IMS spectra (^{54m}Sc with $T_{1/2}=7\mu$s) or their energy levels are too low to change the result within the error bars given in Table 5.2. For all nuclides with isomeric states (labeled with *) in Table 5.2, however, we subtracted half the isomeric level energy from the experimentally determined mass value to obtain the ground state energy, as it is recommended in AME-2003.

5.2 Results from the ^{238}U Experiment

Nuclide	mass excess [keV]	uncertainty [keV]	ref.
^{95}Rb	-65854	21	[ACERC+86, ABW03]
^{97}Rb	-58360	30	[ACERC+86, ABW03]
^{95}Sr	-75117	7	[RHAB+02, ABW03]
^{103}Zr	-67870	50	[Ä03]
^{129}Sn^{g,m}†	-80576	45	[Sik03, ABW03]
^{132}Sn	-76554	14	[Sik03, ABW03]
^{142}Cs	-70515	11	[AAB+99, ABW03]
^{143}Cs	-67671	24	[ACERC+86, ABW03]
^{145}Cs	-60057	11	[Web04, ABW03]
^{146}Cs	-55620	70	[ACERC+86, ABW03]
^{143}Ba	-73936	13	[AAB+99, ABW03]

Table 5.3: Nuclides used as the reference masses.

The nuclides with well-known masses used as reference values are listed in Tab. 5.3. Although there are more nuclides with known masses obtained in the spectra, we have chosen those, which have been measured directly, i.e., to avoid to use mass values, which have been determined via Q_β-measurements. In general, it is very difficult to obtain masses by measurement of the Q_β value. Q_β values of exotic nuclides are very often higher than 5 MeV, where there are no reference Q_β-values known for the detector calibration and the response function is complicated. Furthermore the Q_β-value determination depends on the known β-decay

---

[†] A mean value taken from ground state -80594 (29) keV and isomer with an excitation energy 35.2(0.3) keV [ABBW97] as -80576 (45) as the isomeric ratio is unknown.

scheme, especially if the number of β-branches is not high. If there are many β-branches, then the averaging procedure smoothes the final value. On the other hand, it is very difficult to analyze many components. In the construction of the Fermi-Curie graph the procedure of choosing the energy interval for obtaining the end-point is usually ambiguous. The measurement can be also complicated by γ-rays, especially if they belong to higher intensity β-branches.

The atomic mass compilation by [ABW03] is using interpolations and parameterization of mass formulas to obtain the best mass values. Several incorrect mass values used in the region can therefore lead to large uncertainties.

Deviations of known mass values [ABW03] from values obtained in our measurement are shown in Fig. 5.1. Although there are some nuclides, for which the values do not agree within the given errors, it is within the expectations from statistics.

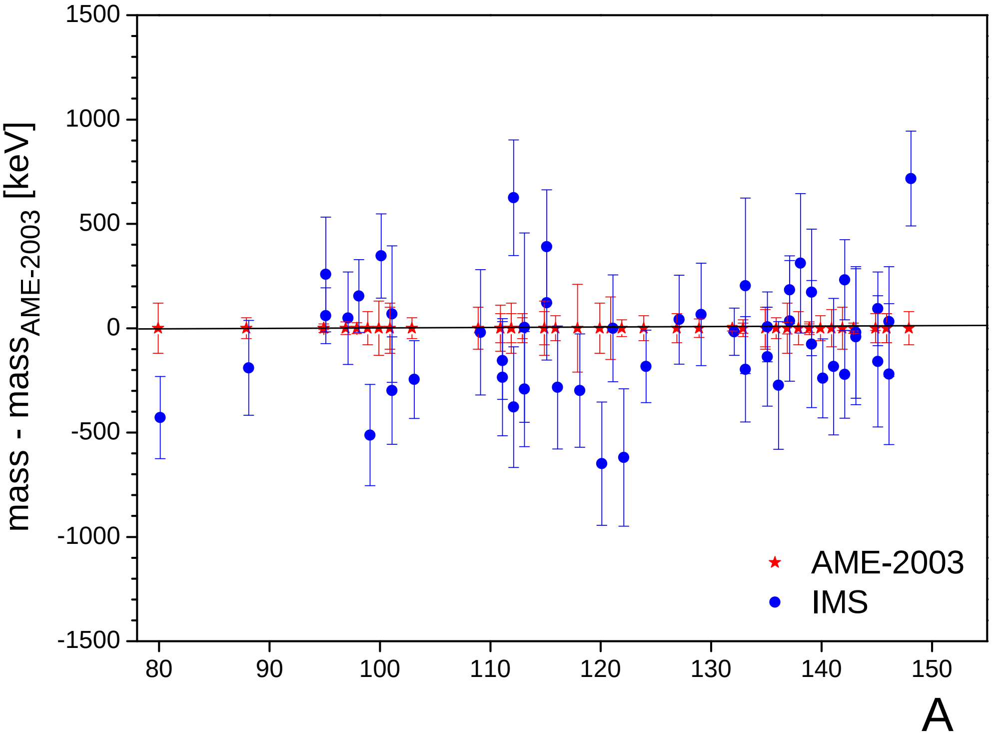

Figure 5.1: Comparison of our mass values obtained in the IMS measurement with the compiled values [ABW03]. Agreement is within the error bars and the statistical law.

The comparisons of our results with the mass values from the extrapolation [ABW03] are shown in Fig. 5.2. The deviations are much larger than it was in the case of previously known masses.

The mass values determined for the first time in this experiment are listed in Tab. 5.4.

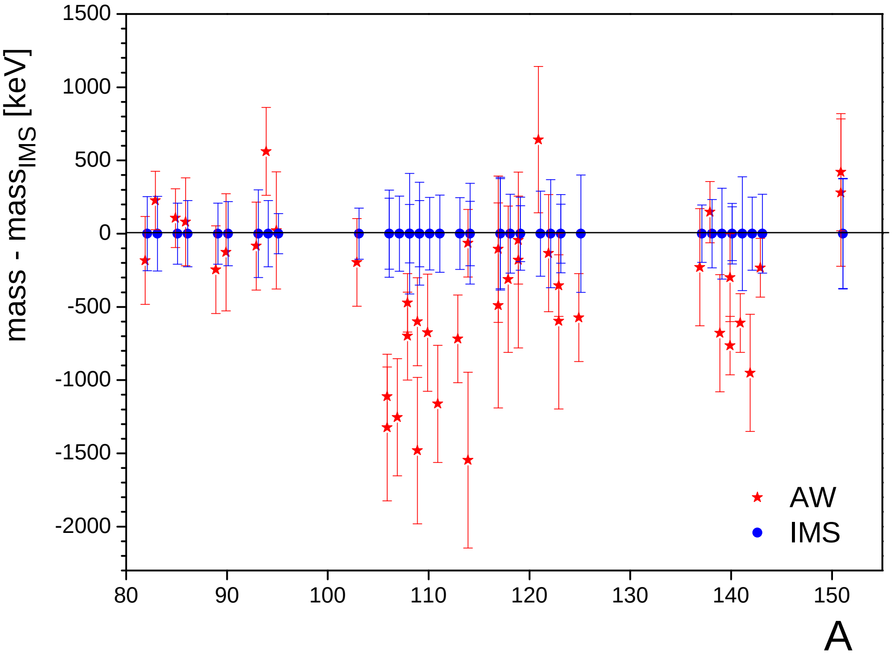

Figure 5.2: Comparison of our new mass values obtained in the IMS measurement with the mass values from extrapolations [ABW03]. The deviations are much larger than it was in the case of previously known masses.

Z	A		mass excess [keV]	error [keV]
31	82	Ga	-52920	250
32	83	Ge	-61130	250
33	85	As	-63430	210
33	86	As	-59230	230
34	89	Se	-58950	210
34	90	Se	-55800	220
35	93	Br	-52970	300
36	94	Kr	-61700	230
36	95	Kr	-56060	140
39	103	Y	-58740	170
40	106	Zr	-58380	300

41	106	Nb	-65990	240
41	107	Nb	-63670	260
41	108	Nb	-60000	410
41	109	Nb	-56620	350
42	108	Mo	-70830	200
42	109	Mo	-66650	230
42	110	Mo	-64780	250
42	111	Mo	-59940	260
43	113	Tc	-63000	250
43	114	Tc	-58180	340
44	114	Ru	-70460	220
44	117	Ru	-59520	390
45	117	Rh	-68840	380
45	118	Rh	-64830	270
45	119	Rh	-63060	250
46	119	Pd	-71580	190
46	121	Pd	-66900	290
46	122	Pd	-64560	370
46	123	Pd	-60010	270
47	123	Ag	-69610	200
47	125	Ag	-64230	400
51	137	Sb	-60030	200
52	138	Te	-66080	230
52	139	Te	-60120	310
52	140	Te	-56660	210
53	140	I	-63510	180
53	141	I	-59910	390
53	142	I	-54770	250
54	143	Xe	-60220	270
57	151	La	-54710	370

Table 5.4:
41 nuclides with experimental mass values, for which the masses have been measured for the first time.

There are new mass values for 41 nuclides with half-lives from 100 ms to 5 s. The lower limit can be even smaller as there are several unknown half-lives of very exotic nuclides.

The area of nuclides of our new masses is shown in the chart of the nuclides, see Fig. 5.3. One can see, that in several regions we are approaching the r-process.

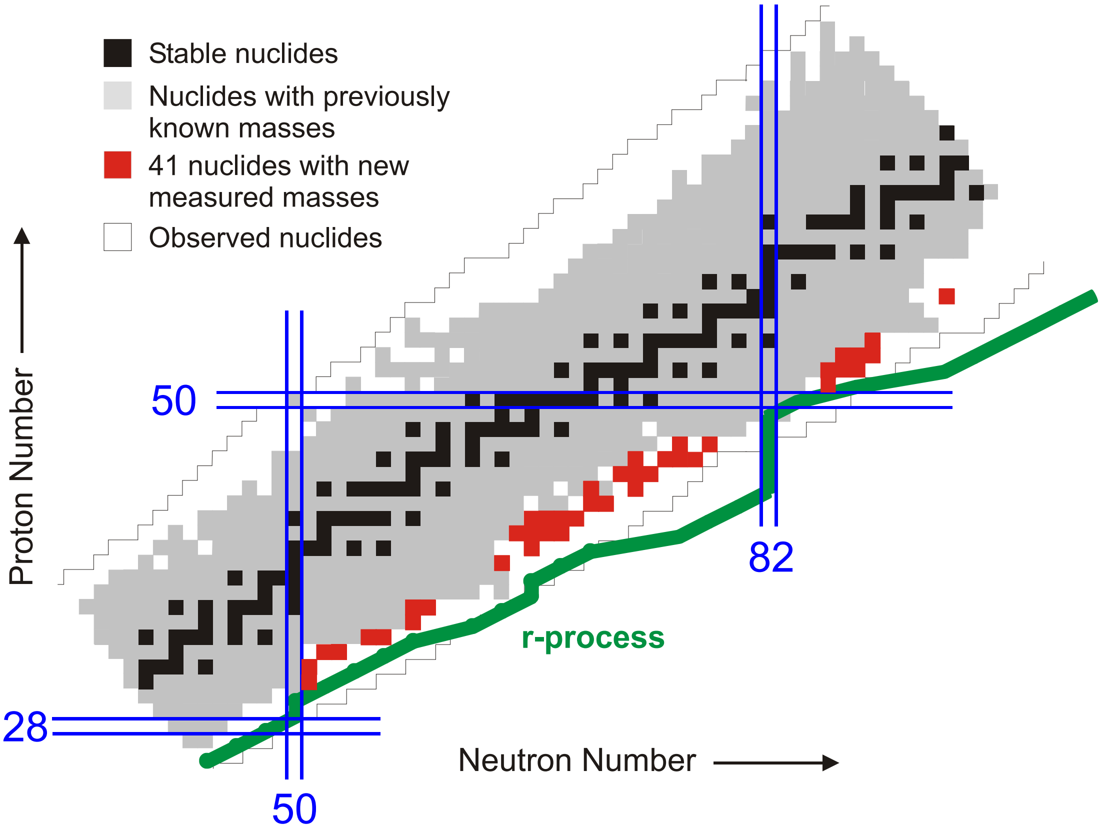

Figure 5.3: Chart of the nuclides representing the knowledge of mass values. Nuclides measured for the first time in this work are indicated by red color. The nuclides are close to the r-process path shown by the green line.

5.3 Comparison with Other Experimental Results

In the experiment of fragmentation of ^{70}Zn we have covered the same isotope region as TOFI measurements at Los Alamos [ZTW+91, SWV+94].

Neutron-rich nuclei were produced via spallation and fission induced by the proton beam. Products were separated by a mass-to-charge filter and transmitted to TOFI. The isochronous spectrometer TOFI is a highly symmetrical system arranged such that the flight time of ions of a particular mass-to-charge ratio is independent of the velocity. In this sense it was an ancestor for our isochronous mass measurements. In the TOFI measurements only an incomplete turn was used, we gain from using a multi-turn device.

A comparison of our mass values with the TOFI results [ZTW+91, SWV+94] is shown in Fig. 5.4. The error bars include both uncertainties from our measurement and from the TOFI measurement, $\sigma = \sqrt{\sigma^2_{\mathrm{TOFI}} + \sigma^2_{\mathrm{IMS}}}$. In general there is good agreement, the deviations are mainly on the order of error bars. The mass values are listed in the Tab. 5.5.

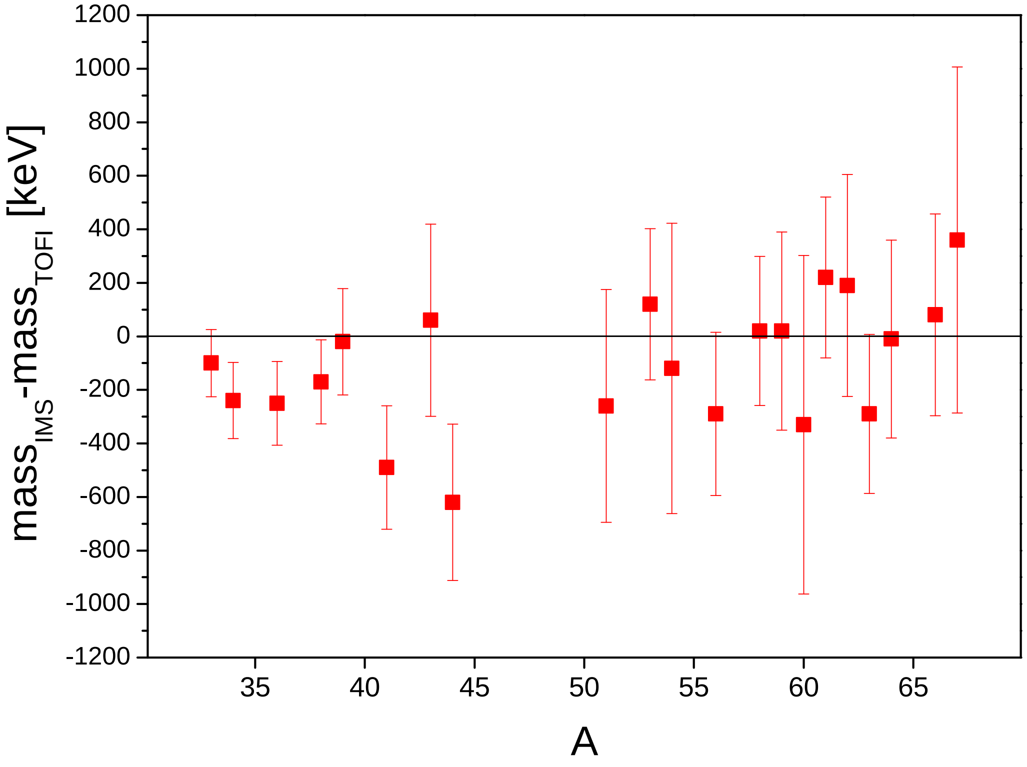

Figure 5.4: Comparison of mass values from this work with the TOFI results [ZTW+91, SWV+94]. The error bars include both uncertainties from our measurement and from the TOFI measurement. The deviations are mainly smaller than error bars.

Elem.	A	ME (IMS) [keV]	ME (TOFI) [keV]
Al	33	-8500(60)	-8400(110) [ZTW+91]
Al	34	-2980(90)	-2740(110) [ZTW+91]
Si	36	-12460(70)	-12210(140) [ZTW+91]
P	38	-14640(70)	-14470(140) [ZTW+91]
P	39	-12670(130)	-12650(150) [ZTW+91]
S	41	-19090(70)	-18600(220) [ZTW+91]
Cl	43	-24130(80)	-24190(350) [ZTW+91]
Cl	44	-20600(150)	-19980(250) [ZTW+91]
Ca	51	-36560(170)	-36300(400) [SWV+94]
Sc	53	-38840(110)	-38960(260) [SWV+94]

Sc	54	-34520(210)	-34400(500) [SWV+94]
Ti	56	-39420(120)	-39130(280) [SWV+94]
V	58	-40360(100)	-40380(260) [SWV+94]
V	59	-37890(120)	-37910(350) [SWV+94]
V	60	-33430(200)	-33100(600) [SWV+94]
Cr	61	-42550(110)	-42770(280) [SWV+94]
Cr	62	-41010(110)	-41200(400) [SWV+94]
Mn	63	-47040(100)	-46750(280) [SWV+94]
Mn	64	-43110(120)	-43100(350) [SWV+94]
Fe	66	-50240(140)	-50320(350) [SWV+94]
Fe	67	-46240(410)	-46600(500) [SWV+94]

Table 5.5: Comparison of mass values from this work with the TOFI results. The deviations are mainly smaller than error bars σ.

5.4 Discussion of the results

Table 5.2 shows that about half of the listed nuclides have experimental values which differ by more than one σ-value from the values in the AME-2003 evaluation. The same inconsistency we observed in our IMS experiments with uranium projectiles [MNB+]. Recent precise measurements by the Penning trap technique ([Ä03] and [Cla03]) also noted such discrepancies of their data with evaluated values in AME-2003 [ABW03]. The most striking deviations of more than 4σ and 6σ have been observed for ^{147}La and ^{158}La, respectively, in [Cla03].

Fig. 5.5 shows the deviation of our experimental mass values from the AME-2003 data for neutron-rich nuclides with deviations larger than 1σ-value. The data for the region of A$= 40 - 70$ have been taken from the present study, however for the region of A$= 80 - 150$ from various mass measurements of fission products — an effective source of neutron-rich nuclei. They are our previous measurements for uranium fission products [MNB+], proton induced fission for Zr-products (A$= 96 - 104$) [Ä03], and Penning trap results of A$= 140 - 150$ [Cla03].

As it can be seen from Fig. 5.5 there are even larger deviations for the extrapolated mass values in AME-2003. Though the error bars are also very large for corresponding differences (very often because of high error bars for extrapolations) the deviation from an experiment for some of the extrapolated values exceeds 2σ.

The large deviation of directly measured mass values in comparison with the evaluated ones, systematically observed for different large regions of the neutron-rich nuclides, has not been observed so far. Indeed, as can be seen from the

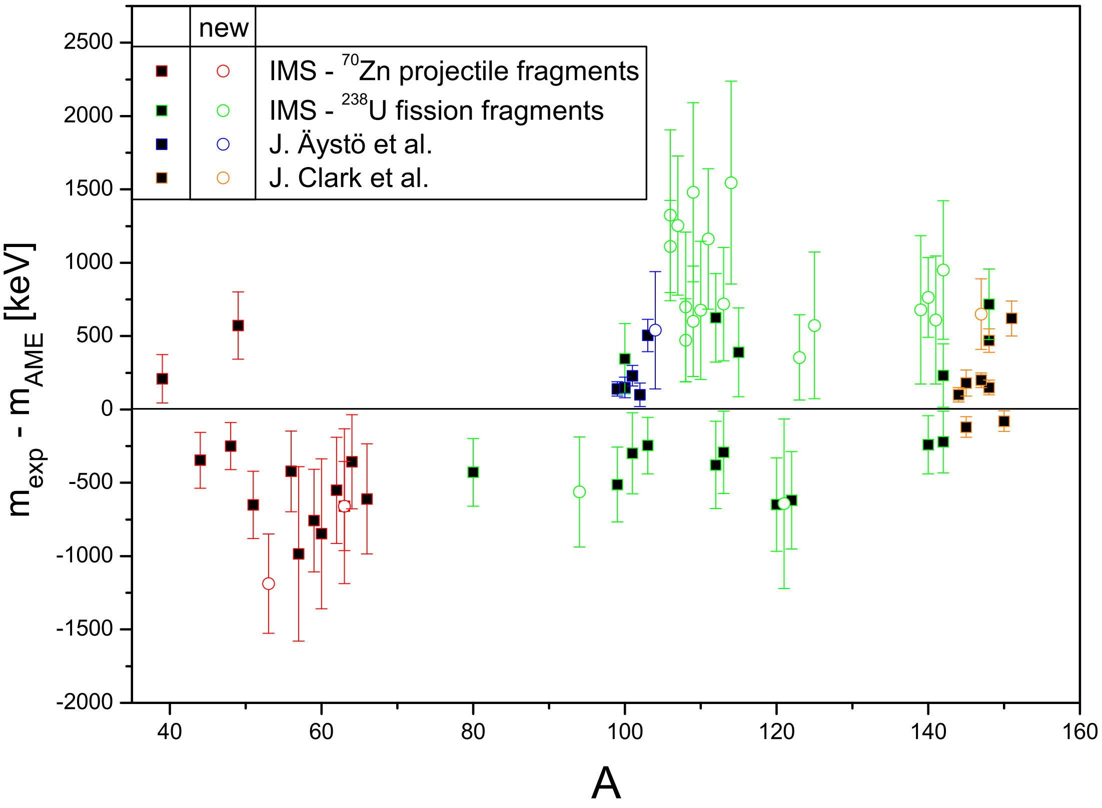

Figure 5.5: Comparison of AME-2003 evaluated data with experimental values measured in this work and recent measurements [Ä03], [MNB+] and [Cla03].

results measured by means of Schottky Mass Spectrometry (SMS) in the neutron-deficient side of the chart of the nuclides only very few mass values out of 450 have deviations up to 300 – 400 keV [Lit03]. Typical deviations from current evaluations [ABBW97] were tens of keV only.

Our relatively large uncertainties are partially due to the difficult conditions for calibration in the neutron-rich region of the chart of nuclides.

Another problem was the discrepancy of measured values with the previous ones. The latter belong mainly to SPEG and TOFI-measurements in the region of light and medium weight nuclides (see Table 5.2) and to the β-decay spectroscopy data for the fission products. The SPEG and TOFI-data are not precise, whereas the β-decay values were claimed to have much better precision for many of determined mass values, by the way, did not checked by other methods. We have already mentioned above that the error bars for masses determined from β-decay spectroscopy could be underestimated because of many reasons, that took place for nuclides investigated in [MNB+]. As a confirmation of this point of view we can refer also to the mentioned data of direct mass measurements announced very recently [Ä03] and [Cla03] , which also show large deviations from β-decay data for some of the nuclides (see Fig. 5.5).

5.5 Comparison with Mass Models

In most theoretical nuclear models, the binding energies of nuclei, and hence their masses are one of the basic properties, since they can be verified experimentally. There are several models available, that can be compared with our results.

5.5.1 Mass Models

Based on the liquid drop the nuclear binding energies and therefore also nuclear masses were for the first time described by von Weizsäcker [vW35]. The model was adjusted by Bethe and Bacher [BB36] into the form

$$M = NM_n + ZM_p - \alpha A + \beta(N-Z)^2/A + \gamma A^{\frac{2}{3}} + \frac{3}{5}(e^2/r_0)Z^2A^{-1/3} \tag{5.1}$$

where A is the atomic weight, N and Z the numbers of neutrons and protons, $r_0A^{\frac{1}{3}}$ the nuclear radius, M_n and M_p the masses of neutron and proton. The parameters were determined empirically. The volume term with the parameter $\alpha = 13.86$ MeV represents the main binding energy. The decrease of the binding energy when the numbers of protons and neutrons become different is described by the term with the parameter $\beta = 19.5$ MeV. A surface effect is reflected in the term with the parameter $\gamma = 13.2$ MeV. The Coulomb repulsion is derived using empirical radii from $r_0 = 1.48 \times 10^{-13}$ cm to be $\frac{3}{5}e^2/r_0 = 0.58$ MeV.

The Bethe-Weizsäcker formula is the basis for macroscopic mass formulas, that are usually improved by applying deformations and oscillations of the nucleus.

The macroscopic approach does not describe shell effects, pairing etc. For this reason microscopic corrections are taken into account. Macroscopic-microscopic mass models can contain an empirical shell part (Tachibana et al. [TUYY88]), the Hugenholtz-Van Hove theorem (Satpathy-Nayak [SN88]) or proposed equation (Masson-Jänecke [MJ88]). The finite range liquid-droplet model (FRLDM) and finite range droplet model (FRDM) include Strutinsky shell corrections, BCS pairing corrections and a Wigner term [MNMS95].

A fully self-consistent approach is applied in pure microscopic mass models. They are based on a solution of the Schrödinger equation (in the non-relativistic case) or the Dirac equation (in the relativistic case) with the interactions between protons and neutrons. However, the computation time time required for such calculations is huge. Therefore, one has to limit these calculations to a smaller nucleon number and, at the same time, exploit these those symmetries of the mean field that can reduce the computation time. A typical and commonly used non-relativistic approach is the Hartree-Fock approximation. The effective interaction is mostly described by the Skyrme force [Sky56], an alternative is the more complicated Gogny force [Gog75]. Recently calculations with different pairing correlation approaches were published. The Bardeen-Cooper-Schriefer method using the Skyrme force MSk7 in the so-called HFBCS model [GTP01] and Bogoliubov method with the Skyrme force BSk2 in HFB model [SGP03] were applied. Relativistic calculations consume even more computation time. Calculations using the Relativistic-Mean-Field (RMF) theory with two body interactions of the Yukawa type appeared recently [LRR99].

There are several approximations much closer to the Hartree-Fock method than droplet-model-based methods. In the Thomas-Fermi method a smooth density function is constructed with various potentials. A Yukawa type interaction is used by Myers-Świątecki [MS96]. The extended Thomas-Fermi method combined with the Strutinsky integral known as ETFSI uses the Skyrme force SkSC18 [PN00]. An effective interaction smooth enough for Hartree-Fock calculations is used by Duflo-Zuker [DZ95].

Another possibility is that the models are completely empirical and employ some general features. The Garvey-Kelson relation [GK66] assumes that the binding energy is a smooth function of A and Z. Using this method new masses obtained by interpolation and extrapolation were calculated by Comay-Kelson-Zidon [CKZ88] and Jänecke-Masson [JM88]. In the Atomic Mass Evaluation AME-2003 [ABW03], the masses of nuclei are obtained by smooth extrapolations of the trends of two-proton and two-neutron separation energies.

A comparison of the model predictions with our data is shown in the Sec. 5.5.2.

5.5.2 Predictive Power of Mass Models

The decisive test of mass models is a comparison with newly measured masses. The predictive power of various models for masses presented for the first time in this work is shown in Tab. 5.6.

The average deviation of the model from experimental data σ_{th} is defined such, that it fulfills the expression

$$\frac{1}{n-1}\sum_{i=1}^{n}\frac{(m_{exp}-m_{th})_i^2}{(\sigma_{exp})_i^2+\sigma_{th}^2}=1. \tag{5.2}$$

The value σ_{th} should be close to the rms-deviation

$$\sigma_{rms}^2=\frac{1}{n}\sum_{i=1}^{n}(m_{exp}-m_{th})_i^2 \tag{5.3}$$

if the experimental errors are less than the theoretical errors [RNG+01]. It is obvious from the values that errors of the theoretical models contribute to the deviations more than the experimental errors. Theoretical predictions for several

Mass formula	$\sigma_{rms}[keV]$	$\sigma_{th}[keV]$
Tachibana et al. [TUYY88]	935	877
Satpathy-Nayak [SN88]	1274	1227
Masson-Jänecke [MJ88]	1002	956
FRLDM [MNMS95]	607	537
FRDM [MNMS95]	667	578
HFB-2 Skyrme force BSk2 [SGP03]	575	491
HFBCS Skyrme force MSk7 [GTP01]	784	714
ETFSI Skyrme force SkSC18 [PN00]	657	578
Myers-Świątecki [MS96]	673	612
Duflo-Zuker (10 par.) [DZ95]	826	765
Duflo-Zuker (28 par.) [DZ95]	683	610
Comay-Kelson-Zidon [CKZ88]	801	733
Jänecke-Masson [JM88]	1186	1133
AME-2003 [ABW03]	651	573

Table 5.6: Predictive power of various mass models. The rms-deviation σ_{rms} of the model from experimental data is obtained from Eq. 5.3, theoretical deviation σ_{th} from Eq. 5.2 Models are in more detail described in Sec. 5.5.1

elements are compared with values achieved in our measurement in Fig. 5.6, where previously known masses are also shown. As it is clear from Tab. 5.6, the best predictions are obtained from the Hartree-Fock-Bogoliubov model [SGP03] and the AME-2003 extrapolations [ABW03], but they also fail for some most exotic nuclides. Unfortunately no RMF calculation for the area presented in this work is available, as this is together with HF one of the most fundamental approaches.

A remarkable result is that the pure microscopic theoretical model [SGP03] is better (σ_{rms} =575 keV) in this new territory than the microscopic-macroscopic FRDM description [MNMS95] (σ_{rms} =667 keV). In the recently measured neutron-deficient new mass surface [Lit03] the FRDM prediction was still a factor of two superior due to the method of parameter adjustment to experimental data. This reflects the advantage of microscopic theories for unknown mass areas far from the valley of beta stability. Much room for improvements is also observed from the comparison with the AME-2003 [ABW03]. The AME-2003 has for our previously measured new neutron-deficient mass surface [Lit03] a σ_{rms} deviation of 148 keV and has now for the 41 new masses in this work 651 keV. For individual nuclides the deviation is even larger, e.g. for ^{109}Nb and ^{114}Tc isotopes the differences from AME-2003 reach 1.5 MeV.

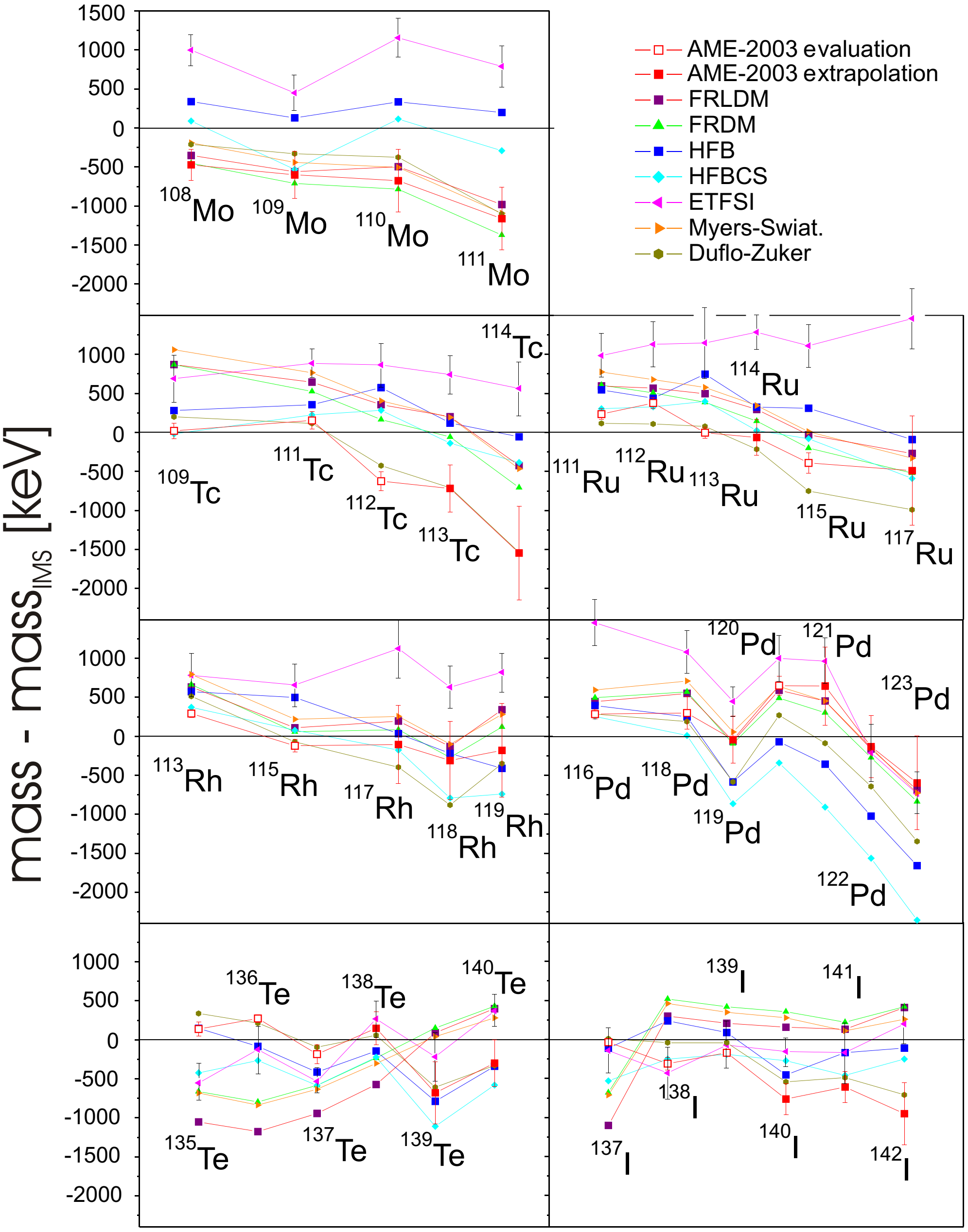

Figure 5.6: Deviations of model predictions (in the case of known AME-2003 mass values they are previously known masses) from masses obtained in our measurement. The comparisons are shown for AME-2003 [ABW03], FRLDM and FRDM [MNMS95], HFB-2 with Skyrme force BSk2 [SGP03], HFBCS with Skyrme force MSk7 [GTP01], ETFSI with Skyrme force SkSC18 [PN00], Myers-Świątecki [MS96] and Duflo-Zuker (28 parameters) [DZ95] tables. The uncertainties of the IMS experimental data are illustrated as error bars of the ETFSI deviations but are valid for all cases.

Chapter 6

Outlook

In future experiments our goals are to increase the resolution and accuracy of the method. A goal will also be to widen the mass-to-charge range for which the isochronicity condition holds. The TOF detector can also be modified from the experience of the present experiments, e.g., to aim for a thinner foil without losing the present efficiency and to avoid the burst of injected ions which will not reach stable orbits.

Furthermore, a future goal is to reach more exotic nuclei towards the neutron dripline, particularly along the predicted r-process path for Z>30. This would require an increase of the primary-beam intensity and a higher efficiency in the ESR acceptance channel.

A huge improvement will be achieved by the new facility FAIR [GSI01, NUS04].

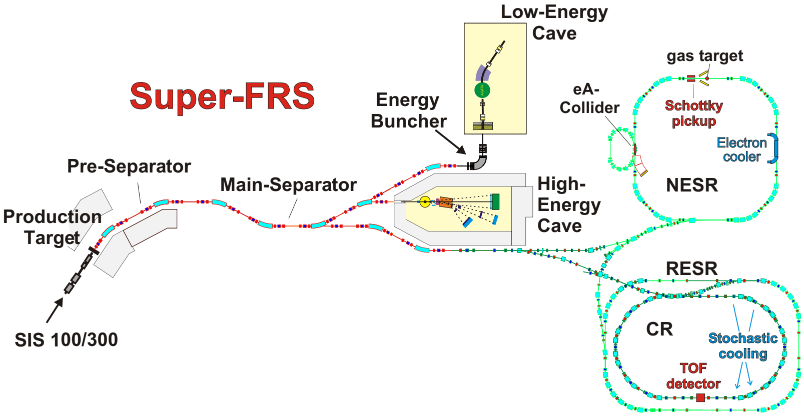

Figure 6.1: Schematic view of the proposed exotic-nuclear-beam facility FAIR. The superconducting two-stage fragment separator (Super-FRS) will provide beams of unstable nuclei for the storage ring system (Collector Ring CR and New Experimental Storage Ring NESR) including an ion-electron collider (e-A), as well as for the high- and low-energy experimental areas. The electron cooler and the Schottky pickup at the NESR and the stochastic cooling and the TOF detector at the CR are shown.

The new synchrotron complex is expected to achieve 1×10^{12} ions/pulse for all heavy ions up to uranium. The new large acceptance fragment separator, the Super-FRS [GWW+03], will provide radioactive beam intensities increased by the factor up to 10 000 compared to the present situation. The Super-FRS will provide beams of exotic nuclei to different experimental ares including the complex of storage rings, see Fig. 6.1.

The Collector Ring (CR) is designed to accept the separated fragment beam from the Super-FRS and to pre-cool with stochastic cooling. The CR in the isochronous mode together with the time-of-flight detector will offer mass measurement of short-lived ions, in a similar way as described in this thesis.

The New Experimental Storage Ring (NESR) is designed to store ions transferred from CR. The electron cooler and several Schottky pickups will be used in the experiments with long-lived nuclei.

The calculated rates for exotic nuclides at the Super-FRS are shown in Fig. 6.2. It is demonstrated that the new facility will be an ideal tool to study the most neutron-rich nuclei, particular along the r-process path for Z>30.

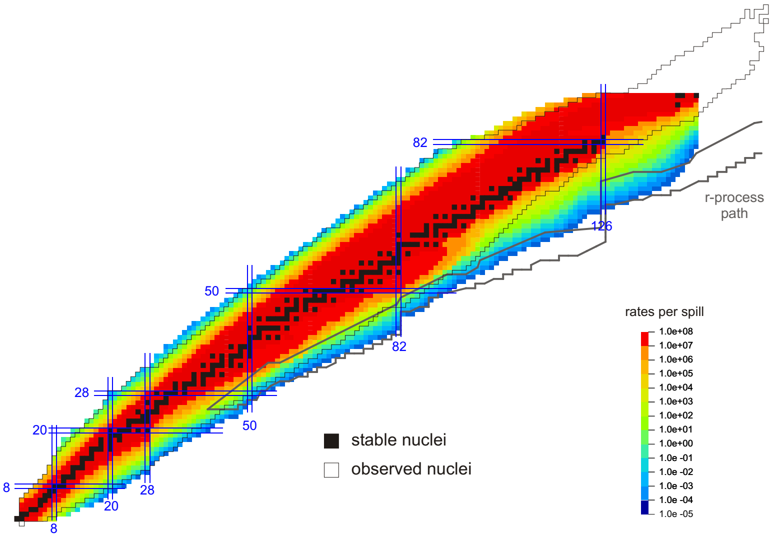

Figure 6.2: Predicted production rates at the Super-FRS facility for primary beam intensities of 10^{12} ions/spill. Stable nuclei (black symbols), closed shells, and the limits of known nuclei are indicated. At the new facility, hitherto unexplored parts of the r-process path will become accessible, in particular around the closed neutron shells.

Appendix A

Description of the TOFSIM Simulation Program

The TOFSIM is a simulation of the mass measurement experiment in the ESR in the isochronous mode. The program has a graphic interface based on the TROLLTECH Qt library [TRO02].

Production of exotic nuclei and their separation in the FRS are calculated by the simulation program MOCADI [IGM+97, SGM+88]. The command '*export*' at the injection into ESR in the MOCADI input file produces an ASCII output, which contains information about separated ions, proton number, charge, mass, vertical and horizontal position and angle, energy and time–of–flight. The ASCII file is used as an input file in the TOFSIM (see Fig. A.1 and A.2).

The program MOCADI is using the same number of ions produced in the target for all simulated nuclides and only the transmission without the cross section is included. Hence the histograms are weighted according to cross–sections, so that the intensities correspond to yields. There are two modes possible to provide the cross section values. For the fragmentation process the EPAX2 formula [SB00] is implemented. For this purpose the production target as well as the beam have to be specified, see Fig. A.2. This is the default mode and can be explicitly declared in the input file by the '*fragmentation*' command inserted in the separated line before all fragmentation particles. Analogously the fission mode is switched by the '*fission*' command. The EPAX formula cannot be used for the fission, so the cross–section values for all particles after the command are read from the specified file. The file has the following format:

`Z(int) A(int) q(int)` σ`(float)[`μb`]`

The default value for the non–listed isotopes is zero or can be specified in the first file line with $Z = 0$, $A = 0$ and $q = 0$ values,

`0 0 0 1.000 ,`

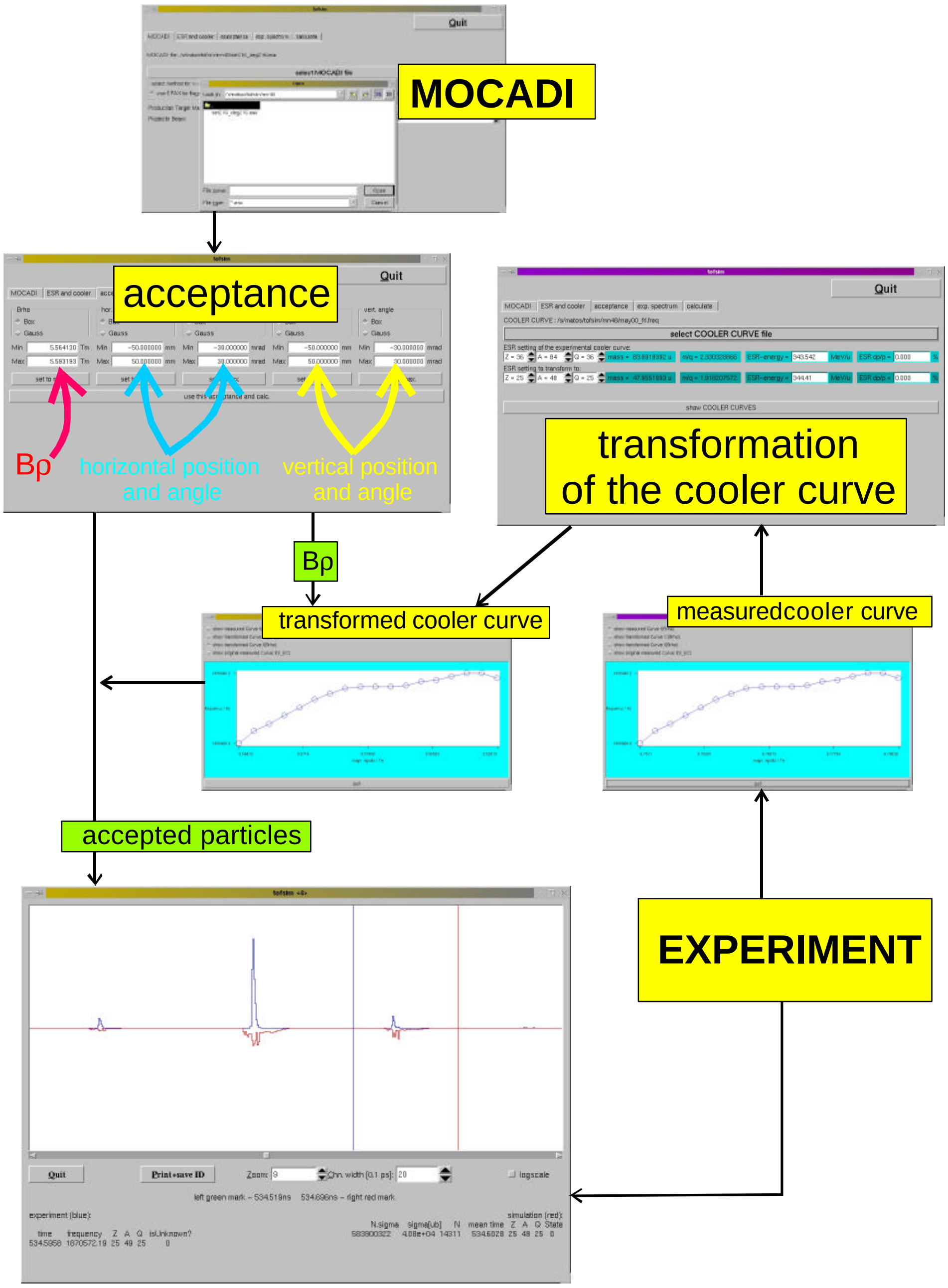

```
Quit        Print+save ID        Zoom: 9    Chn. width [0.1 ps]: 20        logscale
                 left green mark – 534.519ns    534.696ns – right red mark
experiment (blue):                                                           simulation (red):
                                                   N.sigma   sigma[ub]    N    mean time  Z  A  Q  State
  time      frequency   Z  A  Q  isUnknown?       583900322   4.08e+04  14311   534.6028  25 48 25  0
534.5958  1870572.19  25 48 25      0
```

Figure A.1: Systematic scheme of the TOFSIM simulation. Results from the MOCADI simulation are used as an input. After acceptance parameters are applied the revolution times are calculated using an isochronicity curve. Their spectrum can be compared with results from a measurement.

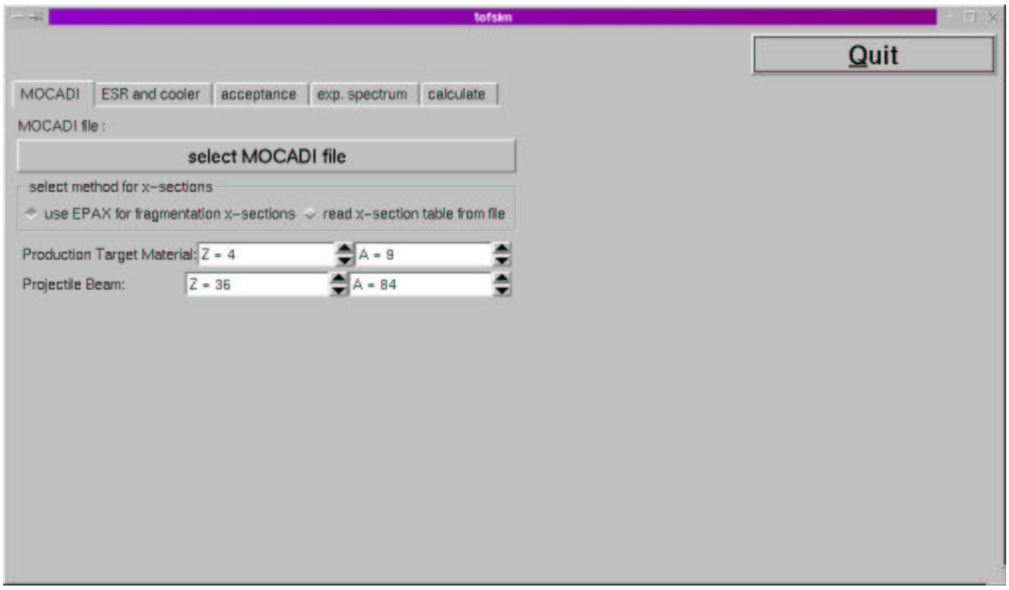

MOCADI file :

select method for x-sections

◆ use EPAX for fragmentation x-sections ◇ read x-section table from file

Production Target Material: Z = 4 A = 9

Projectile Beam: Z = 36 A = 84

Figure A.2: The window of the TOFSIM simulation, in which the input file calculated by the MOCADI, parameters for the calculation of the fragmentation cross–section and fission cross–section file are specified.

where the default value is $1.0\mu b$ in this case.

In the experiment the revolution time of every particle is measured. The revolution time of every ion from the MOCADI output file can be determined using its energy according to the isochronicity curve and its transformation, for details see Sec. 3.1.3, 3.1.2 and 2.1.1. A file with a measured isochronicity curve and parameters for its transformation have to be set, see Fig. A.3. The choice of the correct central rigidity is essential for the successful simulation.

Simulated particles are selected by the injection acceptance. It can be adjusted for the magnetic rigidity, vertical and horizontal position and angle. Gaussian and constant distributions are available for the acceptance, see Fig. A.4. Parameters are known from the MOCADI simulation. The Gaussian distribution function is using the Monte Carlo method.

Using the procedures mentioned above, a simulated spectrum can be calculated, see Fig. A.5. Only the simulated spectrum is shown. The spectrum can be compared with an experimental spectrum from the file in the '*.3particles*' format. If the corresponding identification file is available, it can be read. The window with both spectra is opened by pressing the '*plot spectra*' button (see Fig.A.5). The opened window consists of two parts, the one with the graphs and the one with the buttons and information about the spectra (see Fig.A.6). The graph is divided into lower (red) simulated spectra and upper (blue) experimental spectra. The figure can be zoomed by the `Zoom` button. The `log` button switches between the linear and logarithmic scale of the y axes. The channel width can be adjusted.

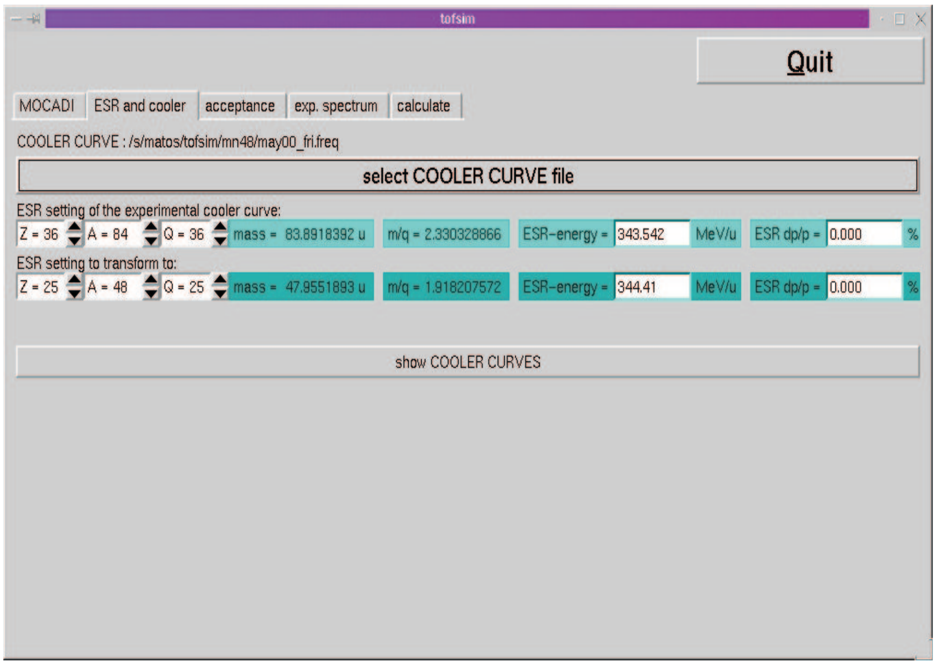

COOLER CURVE : /s/matos/tofsim/mn48/may00_fri.freq

ESR setting of the experimental cooler curve:
Z = 36 A = 84 Q = 36 mass = 83.8918392 u m/q = 2.330328866 ESR−energy = 343.542 MeV/u ESR dp/p = 0.000 %

ESR setting to transform to:
Z = 25 A = 48 Q = 25 mass = 47.9551893 u m/q = 1.918207572 ESR−energy = 344.41 MeV/u ESR dp/p = 0.000 %

Figure A.3: The window of the TOFSIM simulation, in which the isochronicity curve file and parameters for its transformation are specified.

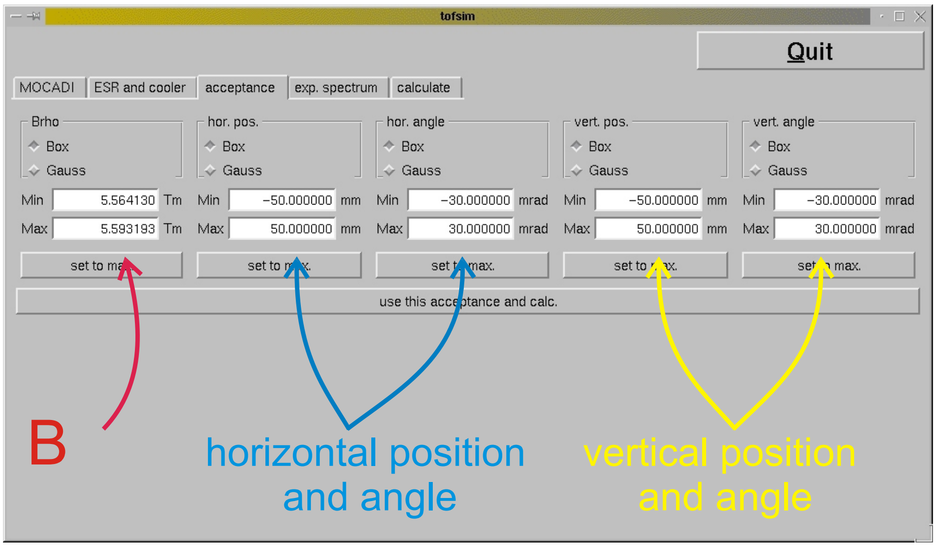

	Brho	hor. pos.	hor. angle	vert. pos.	vert. angle
	◇ Box ◇ Gauss	◇ Box ◇ Gauss	◇ Box ◇ Gauss	◇ Box ◇ Gauss	◇ Box ◇ Gauss
Min	5.564130 Tm	−50.000000 mm	−30.000000 mrad	−50.000000 mm	−30.000000 mrad
Max	5.593193 Tm	50.000000 mm	30.000000 mrad	50.000000 mm	30.000000 mrad

Figure A.4: The window of the TOFSIM simulation for the selection of the acceptance. It can be adjusted for the magnetic rigidity, vertical and horizontal position and angle. Gaussian and constant distributions are available.

When the window is opened, the data with the accepted particles are saved into the file '*simulatedSpectrum.3particles*'. It is in the same format like the analyzed files from the experiment, so it can be used for the further analyses. The number of the particles in the MOCADI file is proportional to the transmission

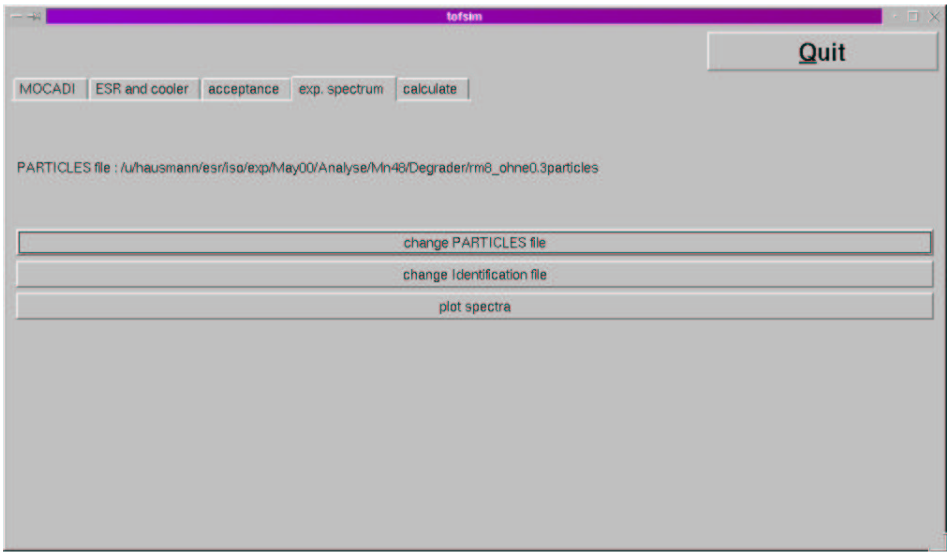

```
PARTICLES file : /u/hausmann/esr/iso/exp/May00/Analyse/Mn48/Degrader/rm8_ohne0.3particles
```

Figure A.5: The window of the TOFSIM simulation for the selection of the file with experimental data and the identification file. The graph is opened with '*plot spectra*' button

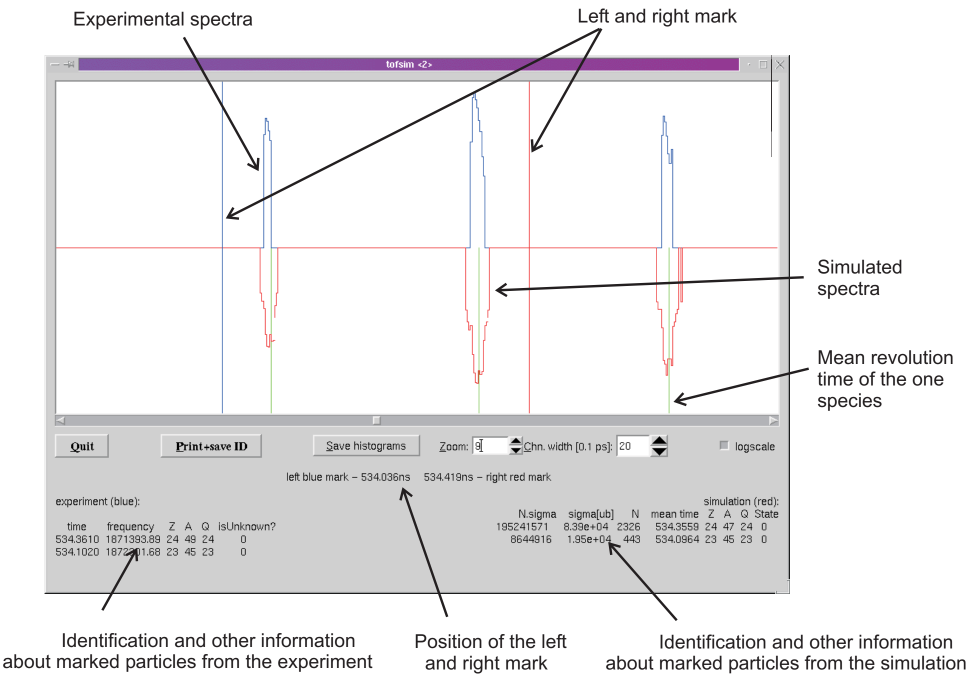

```
left blue mark – 534.036ns    534.419ns – right red mark

experiment (blue):                                                simulation (red):
                                                 N.sigma   sigma[ub]   N   mean time  Z  A  Q State
  time     frequency   Z  A  Q  isUnknown?      195241571  8.39e+04  2326  534.3559 24 47 24  0
534.3610 1871393.89 24 49 24       0              8644916  1.95e+04   443  534.0964 23 45 23  0
534.1020 1872201.68 23 45 23       0
```

Figure A.6: The window of the TOFSIM simulation with the the final graph. The graph is divided into lower (red) simulated spectra and upper (blue) experimental spectra.

through the FRS, it has to be weighted according to the cross-section. This is solved by the selection of the species with lower cross-sections. The particle is included into the file with the probability proportional to the ratio of its cross section and the highest cross section in the data.

The '*Save histogram*' button saves the histogram showed in the current window. It means that the current scale, zoom and channel width are used. The file is in the following format:

$\mathtt{x}\ \mathtt{y}_{measurement,scaled}\ \mathtt{y}_{simulation,scaled}\ \mathtt{y}_{simulation}$

The first column x contains the revolution time in *ns*. Histogram contents are in the y columns. Scaled values are numbers adjusted to draw the graphs in the window, so also the logarithmic scale is applied if switched. The last column contains the row simulated values.

The button '*Print+save ID*' makes the identification file, based on the simulated data. The mean revolution frequency of one species is used. These values can be also drawn in the graph with green lines.

To select on area of interest one can mark the region using the left and right mouse button. The position of the both marks is written in the mid of the lower part. The left side shows information about the experimental data between the marks, the identification file is used. The same information about the simulated data are in the right side.

Bibliography

[Ä03] J. Äystö. Private communication, 2003. 71, 77, 78

[AAB$^+$99] F. Ames, G. Audi, D. Beck, G. Bollen, M. de Saint Simon, R. Jertz, H.-J. Kluge, A. Kohl, M. König, D. Lunney, I. Martel, R. B. Moore, T. Otto, Z. Patyk, H. Raimbault-Hartmann, G. Rouleau, G. Savard, E. Schark, S. Schwarz, L. Schweikhard, H. Stolzenberg, Szerypo J., and the ISOLDE Collaboration. High accuracy mass determination of unstable cesium and barium isotopes. *Nuclear Physics*, A651:3–30, 1999. 71

[ABBW97] G. Audi, O. Bersillon, J. Blachot, and A. H. Wapstra. The NUBASE evaluation of nuclear and decay properties. *Nuclear Physics*, A 624:1, 1997. 71, 78

[ABE$^+$89] N. Angert, W. Bourgeois, H. Emig, B. Franzke, B. Langenbeck, K. D. Leible, H. Schulte, P. Spädtke, and B. H. Wolf. Electron cooling on the ESR at GSI. In S. Tazzari, editor, *Proceedings of the European Particle Accelerator Conference, Rome, 1988*, page 1436, Singapore, 1989. World Scientific. 30

[ABE$^+$90] N. Angert, W. Bourgeois, H. Emig, B. Franzke, B. Langenbeck, K. D. Leible, T. Odenweller, H. Poth, H. Schulte, P. Spädtke, and B. H. Wolf. The 320-keV ESR-electron cooler. In P. Marin and P. Mandrillon, editors, *Proceedings of the 2nd European Particle Accelerator Conference, Nice, 1990*, pages 1374–1376, Gif-sur-Yvette, Cedex, 1990. Edition Frontieres. 13

[ABW03] O Audi, G. Bersillon, J. Blachot, and A. H. Wapstra. The NUBASE evaluation of nuclear and decay properties. *Nuclear Physics*, A729:3–128, 2003. vii, 1, 52, 67, 69, 70, 71, 72, 73, 77, 80, 81, 82

[ACERC$^+$86] G. Audi, A. Coc, M. Epherre-Rey-Campagnolle, G. Le Scornet, C. Thibault, and F. Touchard. Mass–spectrometric measurements of exotic Rb, Cs and Fr isotopes. *Nuclear Physics*, A 449:491, 1986. 71

[Ast33] F. W. Aston. *Mass Spectra and Isotopes.* Edward Arnold, London, 1933. 10

[BAB+03] K. Blaum, G. Audi, D. Beck, G. Bollen, F. Herfurth, A. Kellerbauer, H.-J. Kluge, E. Sauvan, and S. Schwarz. Masses of ^{32}Ar and ^{33}Ar for fundamental tests. *Physical Review Letters*, 91(26):260801, 2003. 12

[BB36] H. A. Bethe and R. F. Bacher. Nuclear physics I. stationary states of nuclei. *Review of Modern Physics*, 8:82–229, 1936. 79

[BBFP85] K. Blasche, D. Böhne, B. Franzke, and H. Prange. The SIS heavy ion synchrotron project. *IEEE Transactions on Nuclear Science*, Ns-32(5):2657, 1985. 9

[BBH+74] J. Borer, P. Bramham, H. G. Hereward, K. Hübner, W. Schnell, and L. Thorndahl. Nondestructive diagnosis of coasting beams with Schottky noise. In *Proc. IXth Conference on High Energy Accelerators, Stanford 1974*, page 53. U. S. Department of Commerce, 1974. 30

[BBH+03] K. Blaum, G. Bollen, F. Herfurth, A. Kellerbauer, H.-J. Kluge, M. Kuckein, S. Heinz, P. Schmidt, , and L. Schweikhard. Recent developments at ISOLTRAP: towards a relative mass accuracy of exotic nuclei below 10^{-8}. *Journal of Physics B*, 36:921–930, 2003. 12

[BCF+00] K. Beckert, F. Caspers, B. Franczak, B. Franzke, R. Menges, F. Nolden, A. Schwinn, and M. Steck. Stochastic cooling at the ESR. *Nuclear Instruments and Methods in Physics Research*, A441:219–222, 2000. 13

[Bel04] P. Beller. Private communication, January 2004. 37

[Bet30] H. Bethe. Theory of the passage of fast corpuscular rays through matter. *Annalen der Physik (Leipzig)*, 5:325–400, 1930. 10, 35

[BGM90] U. Brosa, S. Grossmann, and A Müller. Nuclear scission. *Physics Reports*, 197(4):167–262, 1990. 6

[BH78] J. D. Bowman and R. H. Heffner. A novel zero time detector for heavy ion spectroscopy. *Nuclear Instruments and Methods in Physics Research*, 148:503–509, 1978. 16

[BHR03] M. Bender, P.-H. Heenen, and P.-G. Reinhard. Self-consistent mean-field models for nuclear structure. *Review of Modern Physics*, 75:121, 2003. 2

[BJ93] P. J. Bryant and K. Johnsen. *The principles of circular accelerators and storage rings.* Cambridge University Press, 1993. 27

[BKP+98] A. V. Belozyorov, R. Kalpakchieva, Yu. E. Penionzhkevich, Z. Dlouhý, Š. Piskoř, J. Vincour, H. G. Bohlen, M. von Lucke-Petsch, A. N. Ostrowski, D. V. Alexandrov, E. Yu. Nikolskii, B. G. Novatskii, and D. N. Stepanov. Spectroscopy of ^{13}Be. *Nuclear Physics*, A 636:419–426, 1998. 11

[Bol97] G. Bollen. Modern approaches for direct mass measurements far from stability. *Nuclear Physics*, A 626:297c–305c, 1997. 10

[BVSW98] Y. Bai, D. J. Vieira, H. L. Seifert, and J. M. Wouters. Mass measurement in the fp-shell using the TOFI spectrometer. In B. M. Sherrill, D. J. Morrissey, and C. N. Davids, editors, *Exotic Nuclei and Atomic Masses ENAM98*, volume 455 of *AIP Conference Proceedings*, page 90, 1998. 12

[CKZ88] E. Comay, I. Kelson, and A. Zidon. Mass predictions by modified ensemble averaging. *Atomic Data and Nuclear Data Tables, edited by P. E. Haustein*, 39:235–240, 1988. 80, 81

[Cla03] J. Clark. Precise mass measurements of nuclides approaching the r-process. First Argonne/MSU/JINA/INT RIA Workshop: The r-process: the astrophysical origin of the heavy elements and related Rare Isotope Acclerator Physics, Seattle, USA, January 8-10 2003. 77, 78

[DVE+96] A. Dolinskiy, A. Valkov, H. Eickhoff, B. Franczak, and B. Franzke. Operation of the ESR (GSI, Darmstadt) at the transition energy. In S. Myers, A. Pacheco, R. Pascual, Ch. Petit-Jean-Genaz, and J. Poole, editors, *Proceedings of the 5th European Particle Accelerator Conference (EPAC 96), Sitges, Spain, 10-14 Jun 1996*, pages 596–598, Bristol, 1996. Institute of Physics Publishing. 27, 30

[DZ95] J. Duflo and A. P. Zuker. Microscopic mass formulas. *Physical Review C*, 52:R23–R27, 1995. 80, 81, 82

[EBF+99] T. Enqvist, J. Benlliure, F. Farget, K.-H. Schmidt, P. Armbruster, M. Bernas, L. Tassan-Got, A. Boudard, R. Legrain, C. Volant, C. Böckstiegel, M. de Jong, and J. P. Dufour. Systematic experimental survey on projectile fragmentation and fission induced in collisions of ^{238}U at 1 A GeV with lead. *Nuclear Physics*, A 658(1):47–66, 1999. 5

[FCD+01] T. Fritioff, C. Carlberg, G. Douysset, R. Schuch, and I. Bergström. A new determination of the ^{4}He and ^{3}He masses in a Penning trap. *European Physical Journal*, A 15:141–143, 2001. 12

[FMM+98] B. Fogelberg, K. A. Mezilev, H. Mach, V. I. Isakov, and J. Slivova. Precise atomic mass values near ^{132}Sn: The resolution of a puzzle. *Physical Review Letters*, 82(9):1823–1826, 1998. 11

[Fra87] B. Franzke. The heavy ion storage and cooler ring project ESR at GSI. *Nucl. Instr. Meth.*, B24/25:18, 1987. 13, 30

[GAB+92] H. Geissel, P. Armbruster, K.H. Behr, A. Brünle, K. Burkard, M. Chen, H. Folger, B. Franczak, H. Keller, O. Klepper, E. Pfeng, M. Pfützner, E. Roeckl, K. Rykaczewsky, I. Schall, D. Schardt, C. Scheidenberger, K.-H. Schmidt, A. Schröter, T. Schwab, K. Sümmerer, M. Weber, G. Münzenberg, T. Brohm, H.-G. Clerc, M. Fauerbach, J.-J. Gaimard, A. Grewe, E. Hanelt, B. Knödler, M. Steiner, J. Weckenmann, C. Ziegler, A. Magel, H. Wollnik, J. P. Dufour, Y. Fujita, D. J. Vieira, and B. Sherrill. The GSI projectile fragment separator (FRS): a versatile magnetic system for relativistic heavy ions. *Nuclear Instruments and Methods in Physics Research*, B70:286, 1992. 10, 24

[GAB+01] H. Geissel, F. Attallah, K. Beckert, F. Bosch, M. Falch, B. Franzke, M. Hausmann, Th. Kerscher, O. Klepper, H.-J. Kluge, C. Kozhuharov, Yu. Litvinov, K. E. G. Löbner, G. Münzenberg, N. Nankov, F. Nolden, Yu. Novikov, T. Ohtsubo, Z. Patyk, T. Radon, C. Scheidenberger, J. Stadlmann, M. Steck, K. Sümmerer, H. Weick, and H. Wollnik. Progress in mass measurements of stored exotic nuclei at relativistic energies. *Nuclear Physics*, A 685:115c, 2001. 13, 37

[GBB+92] H. Geissel, K. Beckert, F. Bosch, H. Eickhoff, B. Franczak, B. Franzke, M Jung, O. klepper, R. Moshammer, G. Münzenberg, F. Nickel, F. Nolden, U. Schaaf, C. Scheidenberger, P. Spädtke, M. Steck, K. Sümmerer, and A. Magel. First storage and cooling of secondary heavy-ion beams at relativistic energies. *Physical Review Letters*, 68(23):3412–3415, 1992. 10

[GK66] G. T. Garvey and I. Kelson. New nuclidic mass relationship. *Physical Review Letters*, 16:197, 1966. 80

[GMR95] H. Geissel, G. Münzenberg, and K. Riisager. Secondary exotic nuclear beams. *Annual Review of Nuclear and Particle Science*, 45:163 – 203, 1995. 7, 8, 10

[Gog75] D. Gogny. Simple separable expansions for calculating matrix elements of two–body local interactions with harmonic oscillator functions. *Nuclear Physics*, A 237(3):399–418, 1975. 80

[Gol74] A. S. Goldhaber. Statistical models of fragmentation processes. *Physics Letters*, 53B:306 – 308, 1974. 24

[GS91] J. J. Gaimard and K. H. Schmidt. A reexamination of the abrasion-ablation model for the description of the nuclear fragmentation reaction. *Nuclear Physics*, A531:709, 1991. 6, 26

[GSI01] An international accelerator facility for beams of ions and antiprotons. Conceptual design report, GSI, Darmstadt, November 2001. 83

[GTP01] S. Goriely, F. Tondeur, and J. M. Pearson. A Hartree–Fock nuclear mass table. *Atomic Data and Nuclear Data Tables*, 77(2):311–381, 2001. 80, 81, 82

[GWW+03] H. Geissel, H. Weick, M. Winkler, G. Münzenberg, V. Chichkine, M. Yavor, T. Aumann, K. H. Behr, M. Böhmer, A. Brünle, K. Burkard, J. Benlliure, D. Cortina-Gil, L. Chulkov, A. Dael, J.-E. Ducret, H. Emling, B. Franczak, J. Friese, B. Gastineau, J. Gerl, R. Gernhäuser, M. Hellström, B. Jonson, J. Kojouharova, R. Kulessa, B. Kindler, N. Kurz, B. Lommel, W. Mittig, G. Moritz, C. Mühle, J. A. Nolen, G. Nyman, P. Roussell-Chomaz, C. Scheidenberger, K.-H. Schmidt, G. Schrieder, B. M. Sherrill, H. Simon, K. Sümmerer, N. A. Tahir, V. Vysotsky, H. Wollnik, and A. F. Zeller. The Super–FRS project at GSI. *Nuclear Instruments and Methods in Physics Research B*, 204:71–85, 2003. 84

[HAA+03] F. Herfurth, F. Ames, G. Audi, D. Beck, K. Blaum, G. Bollen, A. Kellerbauer, H.-J. Kluge, M. Kuckein, D. Lunney, R. B. Moore, M. Oinonen, D. Rodríguez, E. Sauvan, C. Scheidenberger, S. Schwarz, G. Sikler, C. Weber, and the ISOLDE Collaboration. Mass measurements and nuclear physics — recent results from ISOLTRAP. *Journal of Physics B*, 36:931–939, 2003. 12

[HAB+00] M. Hausmann, F. Attallah, K. Beckert, F. Bosch, A. Dolinskiy, H. Eickhoff, M. Falch, B. Franczak, B. Franzke, H. Geissel, Th. Kerscher, O. Klepper, H.-J. Kluge, C. Kozhuharov, K. E. G. Löbner, G. Münzenberg, F. Nolden, Yu. Novikov, T. Radon, H. Schatz, C. Scheidenberger, J. Stadlmann, M. Steck, T. Winkler, and H. Wollnik. First isochronous mass spectrometry at the experimental storage ring ESR. *Nuclear Instruments and Methods in Physics Research*, A 446:569–580, 2000. 16, 30

[Hau99] M. Hausmann. *Energieisochrone Massenmessungen am Experimentierspeicherring der GSI*. Ph. D. thesis, University Giessen, June 1999. 27, 30, 48

[HBD$^+$98] M. Hausmann, K. Beckert, A. Dolinskiy, H. Eickhoff, B. Franczak, B. Franzke, H. Geissel, G. Münzenberg, F. Nolden, C. Scheidenberger, M. Steck, Th. Winkler, and H. Wollnik. Operation of the ESR at transition energy. In S. Myers, L. Liljeby, Ch. Petit-Jean-Genaz, J. Poole, and K.-G. Rensfeldt, editors, *Proceedings of the 6th European Particle Accelerator Conference, Stockholm, 1998*, pages 511 – 513. Institute of Physics Publishing, Bristol, 1998. 16, 27

[HBE$^+$98] M. Hausmann, K. Beckert, H. Eickhoff, A. Dolinskiy, B. Franczak, B. Franzke, H. Geissel, G. Münzenberg, F. Nolden, C. Scheidenberger, M. Steck, Th. Winkler, and H. Wollnik. Development and investigation of the isochronous mode of the ESR. In U. Grundinger, editor, *GSI Scientific Report 1997*, GSI-98-1, page 170, D-64291 Darmstadt, 1998. Gesellschaft für Schwerionenforschung mbH. 30

[HHA$^+$00] F.P. Heßberger, S. Hofmann, D. Ackermann, V. Ninov, M. Leino, Š. Šáro, A. Andreyev, A. Lavrentev, A. G. Popeko, and A. V. Yeremin. Decay properties of neutron-deficient nuclei in the region z = 86–92. *European Physical Journal*, A 8:521 – 535, 2000. 11

[HHA$^+$01] F.P. Heßberger, S. Hofmann, D. Ackermann, V. Ninov, M. Leino, G. Münzenberg, Š. Šáro, A. Lavrentev, A. G. Popeko, A. V. Yeremin, and Ch. Stodel. Decay properties of neutron-deficient isotopes ^{256,257}Db, ^{255}Rf, ^{252,253}Lr. *European Physical Journal*, A 12:269 – 277, 2001. 11

[HSA$^+$01] M. Hausmann, J. Stadlmann, F. Attallah, K. Beckert, P. Beller, F. Bosch, Eickhoff. H., M. Falch, B. Franczak, B. Franzke, H. Geissel, Th. Kerscher, O. Klepper, H.-J. Kluge, C. Kozhuharov, Yu. A. Litvinov, K. E. G. Löbner, G. Münzenberg, N. Nankov, F. Nolden, Yu. N. Novikov, T. Ohtsubo, T. Radon, H. Schatz, C. Scheidenberger, M. Steck, Z. Sun, H. Weick, and H. Wollnik. Isochronous mass measurements of hot exotic nuclei. In *Proceedings of the 2nd Euroconference on Atomic Physics at Accelerators APAC2000*, volume 132 of *Hyperfine Interactions*, pages 289–295, 2001. 15, 37

[IGM$^+$97] N. Iwasa, H. Geissel, G. Münzenberg, C. Scheidenberger, Th. Schwab, and H. Wollnik. Mocadi: A universal Monte Carlo code for the transport of heavy ions through matter within ion-optical systems. *Nuclear Instruments and Methods in Physics Research*, B126:284, 1997. 19, 39, 40, 85

[JA02] B. Jurado Apruzzese. *New signatures on dissipation at small deformations from studies of fission induced by peripheral heavy-ion collisions at relativistic energies.* PhD thesis, Universidad de Santiago de Compostela, Facultad de Física, Departamento de Física de Partìculas, Santiago de Compostela, Spain, June 2002. 6

[JM88] J. Jänecke and P. J. Masson. Mass prediction from the Garvey–Kelson mass relations. *Atomic Data and Nuclear Data Tables, edited by P. E. Haustein*, 39:265–271, 1988. 80, 81

[KBB$^+$91] G. Kraft, W. Becher, K. Blasche, D. Böhne, B. Fischer, G. Gademann, H. Geissel, Th. Haberer, J. Klabunde, K. Kraft-Weyrather, G. Langenbeck, G. Münzenberg, S. Ritter, W. Rösch, D. Schardt, H. Stelzer, and Th. Schwab. The heavy ion therapy project at GSI. *Nuclear Tracks and Radiation Measurements*, 19:911, 1991. 9

[KBvO$^+$00] R. Kalpakchieva, H.řG. Bohlen, W. von Oertzen, B. Gebauer, M. von Lucke-Petsch, T.N. Massey, and Th. Wilpert M. Wilpert Th. Ostrowski, A.N. Stolla. Spectroscopy of ^{13}B, ^{14}B, ^{15}B and ^{16}B using multi–nucleon transfer reactions. *European Physical Journal*, A 7:451 – 461, 2000. 11

[KDD$^+$99] E. G. Kessler, Jr., M. S. Dewey, R. D. Deslattes, A. Henins, H. G. Börner, M. Jentschel, C. Doll, and H. Lehmann. The deuteron binding energy and the neutron mass. *Physics Letters*, A 255:221–229, 1999. 11

[KEH$^+$03] V. S. Kolhinen, T. Eronen, J. Hakala, A. Jokinen, S. Kopecký, S. Rinta-Antila, J. Szerypo, and J. Äystö. Penning trap for isobaric mass separation at IGISOL. In *Proceedings of the 14th International Conference on Electromagnetic Isotope Separators and Techniques Related to their Applications*, volume 204 of *Nuclear Instruments and Methods in Physics Research B*, pages 502–506, 2003. 12

[Kel02] A. Kelić. Private communication, July 2002. 26

[Kel03] A. Kelić. Private communication, December 2003. 5

[Kol03] V. S. Kolhinen. *Penning trap for isobaric purification of radioactive ion beams at IGISOL.* Ph. D. Thesis JYFL research report 3/2003, University of Jyväskylä, Finland, 2003. 12

[Kun99] F. Kundracik. *Spracovanie experimentálnych dát (Experimental data analysis).* Faculty of Mathematics and Physics, Comenius University, Bratislava, Slovakia, 1999. 50

[KW03] M. Kraemer and M. Winter. The heavy ion therapy project at gsi webpages. `http://www-aix.gsi.de/~bio/RESEARCH/therapy.html`, 2003. 9

[LAB+03] D. Lunney, G. Audi, C. Bachelet, K. Blaum, G. Bollen, C. Gaulard, S. Henry, F. Herfurth, A. Kellerbauer, A. Lépine-Szily, M. de Saint Simon, H. Simon, C. Thibault, and N. Vieira. High accuracy mass measurement of the very short-lived halo nuclide ^{11}Li. *CERN-INTC-2003-007*, 2003. 12

[LAM+01] A. S. Lalleman, G. Auger, W. Mittig, M. Chabert, M. Chartier, J. Fermé, A. Gillibert, A. Lépine-Szily, M. Lewitowicz, M. H. Moscatello, N. A. Orr, G. Politi, F. Sarazin, H. Savajols, P. Van Isacker, and A. C. C. Villari. Mass measurements of exotic nuclei around N=Z=40 with CSS2. In *Proceedings of the 2nd Euroconference on Atomic Physics at Accelerators APAC2000*, volume 132 of *Hyperfine Interactions*, pages 313–320, 2001. 13

[Leo87] W.R. Leo. *Techniques for Nuclear and Particle Physics Experiments.* Springer Verlag, Berlin Heidelberg, 1987. 42

[LGZ+98] Xiuqin Lu, Jiyu Guo, Kui Zhao, Yehao Cheng, Yong Ma, Zhichang Li, Shuyuan Li, and Ming Ruan. Study of ^{168}Dy mass by heavy ion transfer reactions. *European Physical Journal*, A 2:149 – 151, 1998. 11

[Lit03] Yu. Litvinov. *Basic nuclear properties of neutron-deficient nuclei investigated via high precision mass measurements in the element range of 36 $\leq$ Z $\leq$ 92.* Ph. D. Thesis, Justus Liebig University Giessen, Germany, 2003. viii, 16, 78, 81

[LLSA+02] G. F. Lima, A. Lépine-Szily, G. Audi, W. Mittig, M. Chartier, N. A. Orr, R. Lichtenthaler, J. C. Angelique, J. M. Casandjian, A. Cunsolo, C. Donzaud, A. Foti, A. Gillibert, M. Lewitowicz, S. Lukyanov, M. MacCormick, D. J. Morrissey, A. N. Ostrowski, B. M. Sherrill, C. Stephan, T. Suomijarvi, L. Tassan-Got, D. J. Vieira, A. C. C. Villari, and J. M. Wouters. Direct mass measurements of proton-rich isotopes of Ge, As, Se, and Br. *Physical Review C*, 65:044618, 2002. 12

[LRR99] G. A. Lalazissis, S. Raman, and P. Ring. Ground-state properties of even-even nuclei in the relativistic mean–field theory. *Atomic Data and Nuclear Data Tables*, 71:1–40, 1999. 2, 80

[LZ76] S. Liran and N. Zeldes. Mass predictions: A semiempirical shell-model formula. *Atomic Data and Nuclear Data Tables*, 17:431–441, 1976. 2

[MGV$^+$95] A. Magel, H. Geissel, B. Voss, P. Armbruster, T. Aumann, M. Bernas, B. Blank, T. Brohm, H.-G. Clerc, S. Czajkowsky, H. Folger, A. Grewe, E. Hanelt, A. Heinz, H. Irnich, M. de Jong, A. Junghans, F. Nickel, M. Pfützner, A. Piechaczek, C. Röhl, C. Scheidenberger, K.-H. Schmidt, W. Schwab, S. Steinhäuser, K. Sümmerer, W. Trinder, H. Wollnik, and G. Münzenberg. First spatial isotopic separation of relativistic uranium projectile fragments. *Nuclear Instruments and Methods in Physics Research*, B 94:548, 1995. 10

[MJ88] P. J. Masson and J. Jänecke. Masses from an inhomogeneous partial defference equation with higher–order isospin contributions. *Atomic Data and Nuclear Data Tables, edited by P. E. Haustein*, 39:273–280, 1988. 79, 81

[MJD$^+$01] C. Mazzocchi, Z. Janas, J. Döring, M. Axiotis, L. Batist, R. Borcea, D. Cano-Ott, E. Caurier, G. de Angelis, E. Farnea, A. Faß bender, A. Gadea, H. Grawe, A. Jungclaus, M. Kapica, R. Kirchner, J. Kurcewicz, S.M. Lenzi, T. Martínez, I. Mukha, E. Nácher, D. R. Napoli, E. Roeckl, B. Rubio, R. Schwengner, J. L. Tain, and C. A. Ur. First measurement of g-decay properties of the proton drip-line nucleus ^{60}Ga. *European Physical Journal*, A 12:269 – 277, 2001. 11

[MNB$^+$] M. Matoš, Yu. N. Novikov, K. Beckert, P. Beller, F. Bosch, D. Boutin, T. Faestermann, B. Franczak, B. Franzke, H. Geissel, M. Hausmann, E. Kaza, O. Klepper, H.-J. Kluge, C. Kozhuharov, K.-L. Kratz, Yu. A. Litvinov, L. Maier, G. Münzenberg, F. Nolden, T. Ohtsubo, A. N. Ostrowski, Z. Patyk, B. Pfeiffer, M. Portillo, C. Scheidenberger, J. Stadlmann, M. Steck, D. Vieira, H. Weick, M. Winkler, H. Wollnik, and T. Yamaguchi. Direct mass measurements of short-lived neutron-rich fission fragments at the FRS-ESR facility at GSI. Abstract to the EXON2004-conference, Peterhof, Russia, July, 2004, to be published. 77, 78

[MNMS95] P. Möller, J.R. Nix, W.D. Myers, and W.J. Świątecki. Nuclear ground-state masses and deformations. *Atomic Data and Nuclear Data Tables*, 59:185–381, 1995. vii, 2, 79, 81, 82

[MS96] W. D. Myers and W. J. Świątecki. Nuclear properties according to the Thomas-Fermi model. *Nuclear Physics*, A601:141–167, 1996. 80, 81, 82

[NUS04] NUSTAR. The NUSTAR letters of intent. `http://www.gsi.de/forschung/kp/kp2/nustar.html`, 2004. 83

[Pen01] Yu. E. Penionzhkevich. Mass measurements in nuclear reactions. In *Proceedings of the 2nd Euroconference on Atomic Physics at Accelerators APAC2000*, volume 132 of *Hyperfine Interactions*, pages 263–271, 2001. 11

[PN00] J. M. Pearson and R. C. Nayak. Nuclear–matter symmetry coefficient and nuclear masses. *Nuclear Physics*, A 668:163–171, 2000. 80, 81, 82

[PTVF92] W. H. Press, S. A. Teukolsky, W. T. Vetterling, and B. P. Flannery. *Numerical Recipes in C: the art of scientific computing*. Cambridge University Press, Cambridge, GB, second edition, 1992. 51

[Rad94] T. Radon. *Aufbau und Test eines schnellen Zeitdetektorsystems*. Diploma Thesis, Justus Liebig University Giessen, 1994. 16, 17, 18

[RBF+97] H. Reich, W. Bourgeois, B. Franzke, A. Kritzer, and V. Varentsov. The ESR internal target. *Nuclear Physics*, A626:417c–425c, 1997. 14

[RFK+98] J. Reinhold, J. Friese, H.-J. Körner, R. Schneider, K. Zeitelhack, H. Geissel, A. Magel, G. Münzenberg, and K. Sümmerer. Projectile fragmentation of ^{129}Xe at e_{lab} =790a MeV. *Physical Review C*, 58:247–255, 1998. 5

[RGM+00] T. Radon, H. Geissel, G. Münzenberg, B. Franzke, Th. Kerscher, F. Nolden, Yu. Novikov, Z. Patyk, C. Scheidenberger, F. Attallah, K. Beckert, T. Beha, F. Bosch, H. Eickhoff, Y. Falch, M. Fujita, M. Hausmann, F. Herfurth, H. Irnich, H. C. Jung, O. Klepper, C. Kozhuharov, Yu. A. Litvinov, K. E. G. Löbner, F. Nickel, H. Reich, W. Schwab, B. Schlitt, M. Steck, K. Sümmerer, Th. Winkler, and H. Wollnik. Schottky mass measurement of stored and cooled neutron-deficient projectile fragments in the element range of $57 \leq Z \leq 84$. *Nuclear Physics*, A 677:75–99, 2000. 15, 16

[RHAB+02] H. Raimbault-Hartmann, G. Audi, Beck, G. Bollen, M. de Saint Simon, H.-J. Kluge, M. König, R. B. Moore, S. Schwarz, G. Savard, J. Szerypo, and the ISOLDE Collaboration. High-accuracy mass determination of neutron-rich rubidium and strontium isotopes. *Nuclear Physics*, A 706:3–14, 2002. 71

[RKS+97] T. Radon, Th. Kerscher, B. Schlitt, K. Beckert, T. Beha, F. Bosch, H. Eickhoff, B. Franzke, Y. Fujita, H. Geissel, M. Hausmann, H. Irnich, H. C. Jung, O. Klepper, H.-J. Kluge, C. Kozhuharov, G. Kraus, K. E. G. Löbner, G. Münzenberg, Yu. Novikov, F. Nickel, F. Nolden, Z. Patyk, H. Reich, C. Scheidenberger, W. Schwab, M. Steck, K. Sümmerer, and H. Wollnik. Schottky mass measurement of cooled proton-rich nuclei at the GSI experimental storage ring. *Physical Review Letters*, 78(25):4701 – 4704, 1997. 15

[RNG+01] T. Radon, Yu. N. Novikov, H. Geissel, G. Münzenberg, F. Attallah, K. Beckert, T. Beha, F. Bosch, H. Eickhoff, M. Falch, B. Franzke, Y. Fujita, M. Hausmann, F. Herfurth, H. Irnich, H. C. Jung, Th. Kerscher, O. Klepper, H.-J. Kluge, C. Kozhuharov, Yu. A. Litvinov, K. E. G. Löbner, F. Nickel, F. Nolden, Z. Patyk, H. Reich, C. Scheidenberger, W. Schwab, B. Schlitt, M. Steck, K. Sümmerer, A. H. Wapstra, Th. Winkler, and H. Wollnik. Schottky mass measurements of cooled nuclei and mass landscape of the new area of neutron–deficient sub–uranium nuclides. In U. Grundinger, editor, *GSI Scientific Report 2001*, GSI-01-06, D-64291 Darmstadt, December 2001. Gesellschaft für Schwerionenforschung mbH. 80

[SAA+03] G. Sikler, D. Ackermann, F. Attallah, D. Beck, J. Dilling, S. A. Elisseev, H. Geissel, D. Habs, S. Heinz, F. Herfurth, F. Heßberger, S. Hofmann, H.-J. Kluge, C. Kozhuharov, G. Marx, M. Mukherjee, J. Neumayr, W. R. Plaß, W. Quint, S. Rahaman, D. Rodríguez, C. Scheidenberger, M. Tarisien, P. Thirolf, V. Varentsov, C. Weber, and Z. Zhou. First on-line test of SHIPTRAP. In *Proceedings of the 14th International Conference on Electromagnetic Isotope Separators and Techniques Related to their Applications*, volume 204 of *Nuclear Instruments and Methods in Physics Research B*, pages 482–486, 2003. 12

[SB00] K. Sümmerer and B. Blank. Modified empirical parametrization of fragmentation cross sections. *Physical Review*, C61:034607, 2000. 24, 85

[SBB+00] M. Steck, K. Beckert, F. Bosch, H. Eickhoff, B. Franzke, O. Klepper, R. Moshammer, F. Nolden, H. Reich, B. Schlitt, P. Spadtke, and T. Winkler. Beam accumulation with the SIS electron cooler. *Nuclear Instruments and Methods in Physics Research*, A441:175–182, 2000. 13

[Sch91] U. Schaaf. *Schottky-Diagnose und BTF-Messungen an gekühlten Strahlen im Schwerionen-Speicherring ESR*. Ph. D. Thesis, University Frankfurt, Germany, 1991. 30

[SG98] C. Scheidenberger and H. Geissel. Penetration of relativistic heavy ions through matter. *Nuclear Instruments and Methods in Physics Research*, B 135:25 – 34, 1998. 10, 34

[SGH$^+$00] J. Stadlmann, H. Geissel, M. Hausmann, F. Nolden, T. Radon, H. Schatz, C. Scheidenberger, F. Attallah, K. Beckert, F. Bosch, M. Falch, B. Franczak, B. Franzke, Th. Kerscher, O. Klepper, H.-J. Kluge, C. Kozhuharov, K. E. G. Löbner, G. Münzenberg, Yu. N. Novikov, M. Steck, Z. Sun, K. Sümmerer, H. Weick, and H. Wollnik. First isochronous time-of-flight mass measurements of short-lived projectile fragments in the ESR. In H. O. Meyer and P. Schwandt, editors, *Proceedings of the 4th international Conference on Nuclear Physics at Storage Rings STORI99*, volume 512 of *AIP Conference Proceedings*, page 305, 2000. 37

[SGM$^+$88] Th. Schwab, H. Geissel, G. Münzenberg, K. H. Schmidt, B. Sherrill, and H. Wollnik. In U. Grundinger, editor, *GSI Scientific Report 1987*, GSI-88-1, page 284, D-64291 Darmstadt, 1988. Gesellschaft für Schwerionenforschung mbH. 19, 85

[SGP03] M. Samyn, S. Goriely, and J. M. Pearson. Nuclear mass predictions within the Skyrme HFB theory. *Nuclear Physics*, A 718:653c–655c, 2003. vii, 2, 80, 81, 82

[Sik03] G. Sikler. *Massenspektrometrie kurzlebiger Sr– und Sn– Isotope und Aufbau der SHIPTRAP–Penningfallen*. Ph. D. Thesis, Ruprecht Karl University Heidelberg, 2003. 71

[Sky56] T. H. R. Skyrme. The nuclear spin-orbit coupling. *Philosophical Magazine*, 1:1055–1068, 1956. 80

[SN88] L. Satpathy and R. C. Nayak. Masses of atomic nuclei in the infinite nuclear matter model. *Atomic Data and Nuclear Data Tables, edited by P. E. Haustein*, 39:241–249, 1988. 79, 81

[SSB$^+$00] K.-H. Schmidt, S. Steinhäuser, C. Böckstiegel, A. Grewe, A. Heinz, A. R. Junghans, J. Benlliure, H.-G. Clerc, M. de Jong, J. Müller, M. Pfützner, and B. Voss. Relativistic radioactive beams: A new access to nuclear-fission studies. *Nuclear Physics*, A665:221–267, 2000. 6

[SSM+98] C. Scheidenberger, Th. Stöhlker, W. E. Meyerhof, H. Geissel, P. H. Mokler, and B. Blank. Charges states of relativistic heavy ions in matter. *Nuclear Instruments and Methods in Physics Research*, B 142:441 – 462, 1998. 26, 35, 36

[Sta02] J. Stadlmann. *Erste isochrone Massenmessung kurzlebiger Nuklide am Experimentierspeicherring der GSI.* Ph. D. Thesis, Justus Liebig University Giessen, Germany, 2002. 37, 48

[Ste97] M. Steck. Diagnostic methods to detect the properties of cooled heavy ion beams in storage rings. In F. Bosch and P. Egelhoff, editors, *Proceedings of the 3rd international Conference on Nuclear Physics at Storage Rings STORI96*, volume A626 of *Nuclear Physics*, pages 473c – 483c, 1997. 30

[SWV+94] H.L. Seifert, J.M. Wouters, D.J. Vieira, H. Wollnik, X.G. Zhou, X.L. Tu, Z.Y. Zhou, and G.W. Butler. Mass measurement of neutron-rich isotopes from ^{51}Ca to ^{72}Ni. *ZP*, A349:25, 1994. 75, 76, 77

[TBE+92] J. Trötscher, K. Balog, H. Eickhoff, B. Franczak, B. Franzke, Y. Fujita, H. Geissel, Ch. Klein, J. Knollmann, A. Kraft, K. E. G. Löbner, A. Magel, G. Münzenberg, A. Przewloka, D. Rosenauer, H. Schäfer, M. Sendor, D. J. Vieira, B. Vogel, Th. Winkelmann, and H. Wollnik. Mass measurements of exotic nuclei at the ESR. *Nuclear Instruments and Methods in Physics Research*, B70:455–458, 1992. 16, 17, 18

[THKL99] W. Thalheimer, W. Hartmann, J. Klemm, and B. Lommel. Self-suppoting carbon thinfilms used in the heavy-ion beam. *Crystal Research and Technology*, 34(2):175–179, 1999. 16

[Trö93] J. Trötscher. *Der Experimentierspeicherring der GSI als Flugzeitmassenspektrometer für exotische Nuklide.* Ph. D. Thesis, Justus Liebig University Giessen, 1993. 16, 17, 18

[TRO02] TROLLTECH. Qt library. `http://www.trolltech.com`, 2002. 85

[TUYY88] Takahiro Tachibana, Masahiro Uno, Masami Yamada, and So Yamada. Empirical mass formula with proton–neutron interaction. *Atomic Data and Nuclear Data Tables, edited by P. E. Haustein*, 39:251–258, 1988. 79, 81

[vW35] C. F. von Weizsäcker. Zur theorie der kernmassen. *Zeitschrift für Physik*, 96:431, 1935. 79

[WBB⁺97] H. Wollnik, K. Beckert, T. Beha, F. Bosch, A. Dolinskii, H. Eickhoff, M. Falch, B. Franzke, Y. Fujita, H. Geissel, M. Hausmann, Th. Horvath, H. Irnich, H. C. Jung, Th. Kerscher, O. Klepper, C. Kozhuharov, G. Kraus, K. E. G. Löbner, G. Münzenberg, F. Nickel, F. Nolden, Yu. Novikov, T. Radon, H. Reich, C. Scheidenberger, B. Schlitt, W. Schwab, A. Schwinn, M. Steck, K. Sümmerer, M. Theiss, and Th. Winkler. TOF–mass–measurements of exotic nuclei at the ESR of the GSI. In F. Bosch and P. Egelhoff, editors, *Proceedings of the 3rd international Conference on Nuclear Physics at Storage Rings STORI96*, volume A626 of *Nuclear Physics*, pages 327c – 331c, 1997. 16, 27

[Web04] Ch. Weber. *Konzeption eines kryogenen Penningfallenaufbaus für SHIPTRAP und Massenbestimmungen von Radionukliden um den $Z = 82$ - Schalenabschluss an ISOLTRAP*. Ph. D. Thesis, Ruprecht Karl University, Heidelberg, 2004. 71

[WHB88] H. Wollnik, B. Hartmann, and M. Berz. Principles of GIOS and COSY. In C. Eminihizer, editor, *AIP Conference Proceedings*, volume 177, pages 74–85, 1988. 23

[Wol87] H. Wollnik. Mass separators. *Nuclear Instruments and Methods in Physics Research*, A258:289–296, 1987. 30

[WSB86] H. Wollnik, Th. Schwab, and M. Berz. First ion optical calculations to operate the planned ESR as a time-of-flight mass spectrometer. In U. Grundinger, editor, *GSI Scientific Report 1985*, GSI-86-1, page 372, 6100 Darmstadt, März 1986. Gesellschaft für Schwerionenforschung mbH. 16, 27

[WSC76] B. D. Wilkins, E. P. Steinberg, and R. R. Chasman. Scission-point model of nuclear fission based on deformed-shell effects. *Physical Review*, C 14:1832–1863, 1976. 26

[WWG01] C. Wagemans, J. Wagemans, and G. Goeminne. Determination of atomic masses and nuclear binding energies via neutron induced reactions. In *Proceedings of the 2nd Euroconference on Atomic Physics at Accelerators APAC2000*, volume 132 of *Hyperfine Interactions*, pages 321–327, 2001. 11

[Zer01] T. Zerguerras. *Etude de l'emission proton et de deux protons dans les noyaux légers déficients en neutrons de la région*

A=20. PhD thesis, Universite Pierre et Marie Curie - Paris VI, 2001. `http://tel.ccsd.cnrs.fr/documents/archives0/00/00/26/92/index_fr.html`. 11

[ZTW+91] X. G. Zhou, X. L. Tu, J. M. Wouters, D. J. Vieira, K. E. G. Löbner, H. L. Seifert, Z. Y. Zhou, and G. W. Butler. Direct mass measurements of the neutron-rich isotopes of fluorine through chlorine. *Physics Letters B*, 260(3):285–290, 1991. 75, 76